

University of Alabama in Huntsville

LOUIS

Theses

UAH Electronic Theses and Dissertations

2015

Aerodynamic performance of flexible flapping wings in hover at fruit fly and bumblebee scales

Madhu K. Sridhar

Follow this and additional works at: <https://louis.uah.edu/uah-theses>

Recommended Citation

Sridhar, Madhu K., "Aerodynamic performance of flexible flapping wings in hover at fruit fly and bumblebee scales" (2015). *Theses*. 699.
<https://louis.uah.edu/uah-theses/699>

This Thesis is brought to you for free and open access by the UAH Electronic Theses and Dissertations at LOUIS. It has been accepted for inclusion in Theses by an authorized administrator of LOUIS.

**AERODYNAMIC PERFORMANCE OF
FLEXIBLE FLAPPING WINGS IN HOVER
AT FRUIT FLY AND BUMBLEBEE SCALES**

by

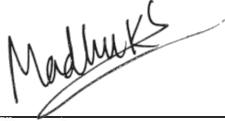
MADHU SRIDHAR

A THESIS

**Submitted in partial fulfillment of the requirements
for the degree of Master of Science in Engineering
in
The Department of Mechanical and Aerospace Engineering
to
The School of Graduate Studies
of
The University of Alabama in Huntsville**

**HUNTSVILLE, ALABAMA
2015**

In presenting this thesis in partial fulfillment of the requirements for a master's degree from The University of Alabama in Huntsville, I agree that the Library of this University shall make it freely available for inspection. I further agree that permission for extensive copying for scholarly purposes may be granted by my advisor or, in his/her absence, by the Chair of the Department or the Dean of the School of Graduate Studies. It is also understood that due recognition shall be given to me and to The University of Alabama in Huntsville in any scholarly use which may be made of any material in this thesis.



Madhu Sridhar

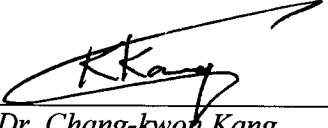
3/9/2015

(Date)

THESIS APPROVAL FORM

Submitted by Madhu Sridhar in partial fulfillment of the requirements for the degree of Master of Science in Engineering in Mechanical Engineering and accepted on behalf of the Faculty of the School of Graduate Studies by the thesis committee.

We, the undersigned members of the Graduate Faculty of The University of Alabama in Huntsville, certify that we have advised and/or supervised the candidate of the work described in this thesis. We further certify that we have reviewed the thesis manuscript and approve it in partial fulfillment of the requirements for the degree of Master of Science in Engineering in Mechanical Engineering.



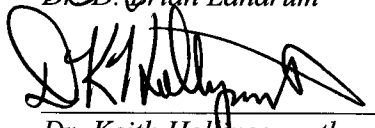
Dr. Chang-kwon Kang 3/20/2015 Committee Chair
(Date)



Dr. Kader Frendi 3/20/15
(Date)



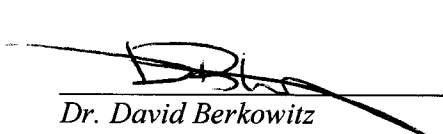
Dr. Brian Landrum 3/20/15
(Date)



Dr. Keith Hollingsworth 3/20/15 Department Chair
(Date)



Dr. Shankar Mahalingam 03/30/15 College Dean
(Date)



Dr. David Berkowitz 4/7/15 Graduate Dean
(Date)

ABSTRACT

School of Graduate Studies
The University of Alabama in Huntsville

Degree Masters of Science College/Dept. Engineering/Mechanical and
in Engineering Aerospace Engineering

Name of Candidate Madhu Sridhar

Title Aerodynamic Performance of Flexible Flapping Wings at Fruit fly and Bumblebee Scales in Hover Flight.

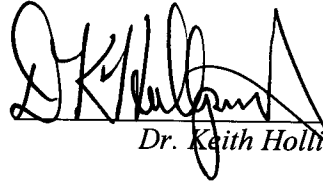
Aeroelastic response at fruit fly and bumblebee scales is explored using a well-validated Navier-Stokes equation solver, fully-coupled with a linear Euler-Bernoulli beam solver. Hover flight is considered with passive pitch at low Reynolds numbers. A systematic study with varying motion amplitudes and wing stiffness showed that the optimal efficiency at both scales was observed at lower reduced frequencies and frequency ratios, whereas lift was the highest at the higher reduced frequency and frequency ratio. The aeroelastic response at bumblebee scale was non-periodic and more unsteady when compared to fruit fly scale, consistent with the higher Reynolds number for the bumblebee. Lift at bumblebee scale was lower. A potential reason is an upward vortex street. Overall, lift at both scales varies with the shape deformation parameter γ . Optimal efficiency motion is closely aligned to experimental observations of fruit flies and bumblebees, suggesting that both insects aim to conserve energy, rather than to generate large forces.

Abstract Approval: Committee Chair



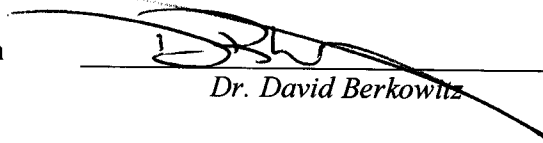
Dr. Chang-kwon Kang

Department Chair



Dr. Keith Hollingsworth

Graduate Dean



Dr. David Berkowitz

TABLE OF CONTENTS

	PAGE
LIST OF FIGURES.....	x
LIST OF TABLES.....	xv
LIST OF SYMBOLS.....	xvi
1 INTRODUCTION	1
1.1 Bio-inspired Micro air vehicles.....	1
1.2 Research objectives.....	5
1.3 Thesis outline	7
1.4 Content disclaimer	8
2 LITERATURE REVIEW	9
2.1 Terminology and dimensionless parameters.....	9
2.1.1 Hovering motion	9
2.1.2 Dimensionless parameters for flexible flapping wing motion	10
2.1.3 Aeroelasticity	10
2.1.4 Scaling and dimensional analysis	11
2.1.5 Reynolds number	12
2.1.6 Reduced frequency.....	12
2.1.7 Strouhal number	13
2.1.8 Frequency ratio	13
2.1.9 Effective stiffness.....	14
2.1.10 Shape deformation parameter	14
2.2 Aerodynamics of insect flight.....	15

2.2.1	Unsteady mechanisms.....	15
2.2.2	Effects of flexibility	20
2.2.3	Experimental observations.....	20
2.3	Kinematics of insect flight.....	22
3	METHODS	26
3.1	Case setup and governing equations.....	26
3.2	Numerical framework and solver functionalities.....	32
3.3	Assumptions.....	34
4	RESULTS	36
4.1	Aeroelastic response at fruit fly scale	37
4.1.1	Aerodynamic performance at fruit fly scale.....	37
4.1.2	Structural response at fruit fly scale.....	39
4.2	Aeroelastic response at bumblebee scale	41
4.2.1	Aerodynamic performance at bumblebee scale	41
4.2.2	Structural response at bumblebee scale	43
4.2.3	Non-periodic aeroelastic response	44
4.2.4	Normalization of lift coefficient	49
5	DISCUSSION.....	51
5.1	Comparison of aeroelastic response at fruit fly, bumblebee and water tunnel scales....	51
5.2	Highest lift motion	56
5.3	Optimal efficiency motion	60
5.4	Scaling of the time averaged lift	64

5.5	Comparison to experimental measurements of fruit flies and bumblebees	66
6	CONCLUSION.....	71
6.1	Summary	71
6.2	Concluding remarks	72
6.3	Implications, consequences and limitations.....	75
6.4	Recommendation for future research.....	76
A.	APPENDIX: TIME AVERAGING AT BUMBLEBEE SCALE	80
B.	APPENDIX: TABLE OF COMPUTATIONAL RESULTS	83
	REFERENCES.....	103

LIST OF FIGURES

Figure	Page
<p>Figure 1-1. State of the art MAV designs (a) Fixed wing design from University of Florida [3]; (b) Nano Hummingbird from AeroVironment [4,6]; (c) Delfly form TU Delft [5,7]; (d) Robobees from Harvard [2].....</p>	2
<p>Figure 1-2. Biological flyers (a) Hummingbird (<i>Archilochus alexandri</i>) [9]; (b) Bumblebee (<i>Bombus pratorum</i>) [10]; (c) Fruit fly (<i>Drosophila melanogaster</i>) [11]; (d) Wasp (<i>Vespula germanica</i>) [12]. Pictures source: Wikimedia Commons. Pictures are under creative commons license..</p>	3
<p>Figure 2-1. Dimensionless variables of interest shown in reference to a bumblebee wing [41].....</p>	11
<p>Figure 2-2. Schematic of clap-and-fling mechanism. A-C represents <i>clap</i> where wings come closer and D-F represents <i>fling</i> where wings move away from each other. Light blue arrows represent force magnitude and direction whereas dark blue arrows indicate induced velocity. Reproduced with permission from ref. [44].....</p>	16
<p>Figure 2-3. Schematic of leading edge suction. The resultant force on a blunt airfoil is perpendicular to the freestream direction due to the suction force acting parallel to the flow. On a thin airfoil such as insect wing, the suction force acts normal to the wing surface due to presence of LEV, thus enhancing the resultant lift. Reproduced with permission from ref. [44].....</p>	17
<p>Figure 2-4. Evolution of LEV and TEV on a two dimensional translating wing. LEV and TEV are shed alternatively to constitute a von Karman vortex street. Magnitude of the aerodynamic force (blue arrows) varies during the motion with highest force observed when a well-defined LEV is formed at the suction side of the wing. Reproduced with permission from ref. [44].....</p>	19
<p>Figure 2-5. A Schematic of wing-wake interaction. Reproduced with permission from Ref [44].....</p>	21
<p>Figure 2-6. Schematics showing the kinematics of flapping insect flight [1]. (a,b) Positional angle, angle of attack and elevation angle are represented by ϕ, α and θ,</p>	

respectively. (c) Time history of evolution the three angles in a hovering flight [1] where ϕ is in green, α is in orange and θ is in blue. (d) Schematic illustrating the difference between geometric and aerodynamic angle of attack. Reproduced with permission from ref. [44]. (e) Schematic illustrating upstroke and downstroke. Reproduced with permission from ref. [44]...... 23

Figure 2-7. Three types of rotational modes observed in flapping flight [8]. Black arrow represents the direction of wing motion and blue arrows represent the pressure force direction and its magnitude..... 24

Figure 3-1. Wing motion and design space [38]. (a) Front view of a fruit fly wing with solid lines representing two dimensional wing section. (b) Schematic of the wing motion with amplitude h_a . The angles at mid and end of the strokes are α_m and α_e , respectively. Lift and drag directions are indicated relative to the wing orientation. Red dot corresponds to leading edge of the wing. (c) Considered design space in terms of effective stiffness Π_1 and reduced frequency k . The contours represent frequency ratio and dots are the test points. 27

Figure 3-2. Computational domain and mesh around the flat plate [7]. (a) and imposed boundary conditions (b) for the fluid flow. The wing is placed at the center of the computational mesh in (b). 33

Figure 3-3. Flowchart illustrating the Fluid Structure Interaction loop [74]. 34

Figure 4-1. Aerodynamic response at fruit fly scale. Variation of (a) time-averaged lift, \bar{C}_L , (b) time-averaged power input, \bar{C}_P and (c) efficiency, η . Trend line shows the direction along which reduced frequency, k increases [38]. Refer Table B-1 for individual values 37

Figure 4-2. Structural response at fruit fly scale. (a) mid-stroke angle, α_m and (b) end-stroke angle, α_e . Refer Figure 9b) for a pictorial representation of the angles [38]. Refer Table B-2 for individual values..... 39

Figure 4-3. Aerodynamic performance at bumblebee scale. (a) Variation of time-averaged lift coefficient \bar{C}_L , (b) time-averaged power input \bar{C}_P , and (c) propulsive efficiency η as a function of frequency ratio f/f_1 and reduced frequency k . Direction

of increase of reduced frequency k is indicated by the black arrow [40]. Refer to Figure 4-1 for the legend. Refer Table B-3 for individual values 42

Figure 4-4. Structural response at bumblebee scale. (a) Variation of midstroke angle α_m and (b) endstroke angle α_e as a function of frequency ratio f/f_1 and reduced frequency k . Direction of increase of reduced frequency k is indicated by the black arrow [40]. Refer Table B-4 for individual values..... 43

Figure 4-5. Time history of C_L and C_D over thirty cycles at bumblebee scale with $k=1.0$, $f/f_1=0.7$. C_D is symmetric about zero line where as C_L average is a positive quantity. 45

Figure 4-6. Non-periodic lift history at bumblebee scale for (a) highest lift motion (b) optimal efficiency motion. Lift history at three different frequency ratios are shown [40]. 46

Figure 4-7. Effects of doubling the number of points on the (a) time averaged lift (b) time averaged drag at bumblebee scale. Increasing the number of points does not smoothen the lift and drag curves. 47

Figure 4-8. Time averaged C_L and C_D at various averaging cycles at bumblebee scale. (a) highest lift motion (b) optimal efficiency motion. Dotted horizontal line represents the averaged value considered in the current study which corresponds to 6-10 cycles..... 49

Figure 4-9. Non-periodic evolution of passive pitch angle α for (a) highest lift motion (b) optimal efficiency motion at bumblebee scale. Response at three frequency ratios are shown. 49

Figure 4-10. Effect of normalization with instantaneous chord length at bumblebee scale. (a) time averaged lift and (b) time averaged drag coefficient. Normalized lift coefficient is shown in red..... 50

Figure 5-1. Aerodynamic contours at fruit fly [38], bumblebee [40] and water tunnel scales [62]. Contours of (a,d,g) time averaged, \bar{C}_L (b,e,h,) time averaged power input, \bar{C}_P (c,f,i) efficiency η for bumblebee scale (top row), fruit fly scale (middle

row) and water tunnel [62] (bottom row) in the design space of effective stiffness Π_1 and reduced frequency k . Refer to Tables B-1 and B-3 in Appendix B for individual values at fruit fly and bumblebee, respectively 52

Figure 5-2. Structural response contours at fruit fly [38], bumblebee [40] and water tunnel scales [62]. Contours of (left) phase lag ϕ and (right) passive pitch amplitude α_a for bumblebee (top row), fruit fly (middle row) and water tunnel (bottom row) scales in the design space of effectiveness Π_1 and reduced frequency k . Refer to Tables B-2 and B-4 in Appendix B for individual values at fly and bumblebee scales, respectively 55

Figure 5-3. Comparison of lift history and wing shapes at highest lift motions at bumblebee [40], fruit fly [38] and water tunnel [62] scales. (a) Time histories of lift for highest lift motions: (-) bumblebee scale (-) fruit fly scale (-) water tunnel scale [62]. Snapshots of wing displacements for (b) bumblebee (c) fruit fly and (d) water tunnel scale..... 56

Figure 5-4. Vorticity contours for maximum lift motions [38,40]. (a) water tunnel scale backward stroke (b) fruit fly scale backward stroke (c) bumblebee scale backward stroke (d) bumblebee scale forward stroke.....57

Figure 5-5. Enlarged view of Figure 5-4(c) at $t^* = 0.5$ which shows reversed von Karman vortex shedding at bumblebee scale LEV_0 and LEV_1 which together form a vortex pair is convected in the upward direction. 60

Figure 5-6. Comparison of lift history and wing shapes at optimal efficiency motions at bumblebee [40], fruit fly [38] and water tunnel [63] scales. (a) Time histories of lift for optimal efficiency motions: (-) bumblebee scale (-) fruit fly scale (-) water tunnel scale [63]. Snapshots of wing displacements for (b) bumblebee (c) fruit fly and (d) water tunnel scale..... 61

Figure 5-7. Vorticity contours for optimal efficiency motions [38,40]. (a) water tunnel scale backward stroke (b) fruit fly scale backward stroke (c) bumblebee scale backward stroke (d) bumblebee scale forward stroke..... 62

Figure 5-8. Scaling of dimensionless parameters at bumblebee, fruit fly and water tunnel scales [40]. (a) Scaling of normalized lift coefficient \bar{C}_L^* with shape deformation parameter γ . (b) Scaling of propulsive efficiency η with passive pitch amplitude α_a at bumblebee, fruit fly, and water tunnel scales. 65

Figure 5-9. Comparison of time history of (a) lift and (b) pitching angle for the most efficient motion at (–) fruit fly scale [38] with (–) experimental measurements [46] (–) three dimensional rigid wing computational data for fruit fly [51] (–) water tunnel scale [62]. The band around the experimental curve in (a) indicates the upper and the lower bounds. 68

Figure 5-10. Graphical representation of two dimensional stroke at the wing tip at bumblebee scale. Wing length is represented by R , stroke angle by Φ and mean chord length by c_m 70

Figure A-1. Variation of time averaged lift with frequency ratio f/f_1 at bumblebee scale performed over 0-10 cycles (first column), 6-10 cycles (second column) and 8-10 cycles (third column). Bottom row corresponds to normalized lift coefficient. Grey and blue regions are bounded by maxima and minima within the motion cycles. .. 79

Figure A-2. Variation of time averaged drag with frequency ratio f/f_1 at bumblebee scale performed over 0-10 cycles (first column), 6-10 cycles (second column) and 8-10 cycles (third column). Bottom row corresponds to normalized drag coefficient. Grey and blue regions are bounded by maxima and minima within the motion cycles. .. 80

Figure A-3. Lift history at bumblebee scale for (top) 0-10 cycles (middle) 6-10 cycles (bottom) 8-10 cycles. Lift coefficient without normalization is shown in red and normalized lift coefficient is in blue. 81

LIST OF TABLES

Table	Page
Table 3-1. Comparison of the dimensionless parameter values at bumblebee, fruit fly and water tunnel [7] scales.	30
Table 5-1. Performance metric at the highest lift and optimal efficiency motions for the bumblebee, fruit fly and water tunnel [62] scales.	53
Table 5-2: Geometric, kinematic and aeroelastic parameters for fruit fly and bumblebee [63].	55
Table B-1. Computational results at fruit fly scale: Aerodynamic parameters.....	82
Table B-2. Computational results at fruit fly scale: Structural parameters.....	88
Table B-3: Computational results at Bumblebee scale: Aerodynamic parameters.....	91
Table B-4: Computational results at Bumblebee scale: Structural parameters.....	98

LIST OF SYMBOLS AND ABBREVIATIONS

SYMBOL	DEFINITION	UNITS
c	Chord	[m]
C_L	Coefficient of lift	[1]
C_P	Coefficient of power input	[1]
E	Young's Modulus	[Pa]
f	Motion frequency	[1/s]
f_1	First natural frequency of the wing	[1/s]
F	Fluid force acting on the wing per unit length	[N/m]
h	Plunge motion of the wing	[m]
h_a	Plunge amplitude	[m]
h_s	Thickness of the wing	[m]
k	Reduced frequency, $\pi fc / U$	[1]
p	Pressure	[Pa]
Re	Reynolds number, Uc / ν	[1]
St	Strouhal number, $2fh_a / U$	[1]
t	Time	[s]
U	Maximum plunge velocity: $2\pi fh_a$ for hover	[m/s ²]
u	Velocity	[m/s]
v	Wing displacement: $v=w+h$	[m]
w	Wing displacement relative to the imposed motion h	[m]
α	Passive pitch angle	[degrees]

α_a	Passive pitch amplitude	[degrees]
α_m	Mid-stroke passive pitch angle	[degrees]
α_e	End-of-the-stroke passive pitch angle	[degrees]
Φ	Stroke angle	[degrees]
φ	Phase lag between passive pitch and plunge motion	[degrees]
γ	Non-dimensional relative shape parameter	[1]
η	Propulsive efficiency: \bar{C}_L / \bar{C}_P	[1]
ν	Kinematic viscosity of the fluid	[m ² /s]
Π_0	Effective inertia: $\rho^* h_s^* (k / \pi)^2$	[1]
Π_1	Effective stiffness: $Eh_s^* / (12\rho_f U^2)$	[1]
ρ_f	Density of the fluid	[kg/m ³]
ρ_s	Density of the wing structure	[kg/m ³]
ω	Vorticity, non-zero component of $\nabla \times \mathbf{u}$	[1/s]
$(\cdot)^*$	Non-dimensional variables	
$(\bar{\cdot})$	Time-averaged variables	
CFD	Computational Fluid Dynamics	
CSD	Computational Structural Dynamics	
LE	Leading Edge	
TE	Trailing Edge	
LEV	Leading Edge Vortex	
TEV	Trailing Edge Vortex	
TiV	Tip Vortex	

DEDICATION

CHAPTER 1

INTRODUCTION

1.1 Bio-inspired Micro air vehicles

Micro air vehicles (MAVs) are miniature flying vehicles often of the order of a few centimeters in physical dimensions. Due to their size and high maneuverability, MAVs are highly sought after in the fields of surveillance, remote sensing and information gathering capabilities [1]. Modern advancements in miniaturizing electronics and manufacturing techniques have made fabrication of these miniature vehicles a reality [2]. It is not farfetched to assume that in the future, a swarm of such robotic flyers may be employed in tandem to perform a coordinated task using communication and coordination algorithms.

MAVs come in predominantly rotary or flexible flapping wing configuration because of the limitations of fixed wing configurations suffer at these scales. The conventional aerodynamics that apply to a passenger airplane cannot be extended to these small scales [1]. This is mainly due to the operational Reynolds number at MAV scale which is orders of magnitude smaller, often around $O(10^2-10^4)$, than passenger airplanes

operating at a Reynolds number of the order of millions. Some of the state of the art MAVs that have been developed around the world are shown in Figure 1-1. From left to right these designs include, a fixed wing design by Ifju et al. [3], Nano Hummingbird developed by AeroVironment [4], which is inspired from hummingbirds, DelFly explorer from TU Delft [5], and the Harvard Robobees [2], which have dual flapping wings.

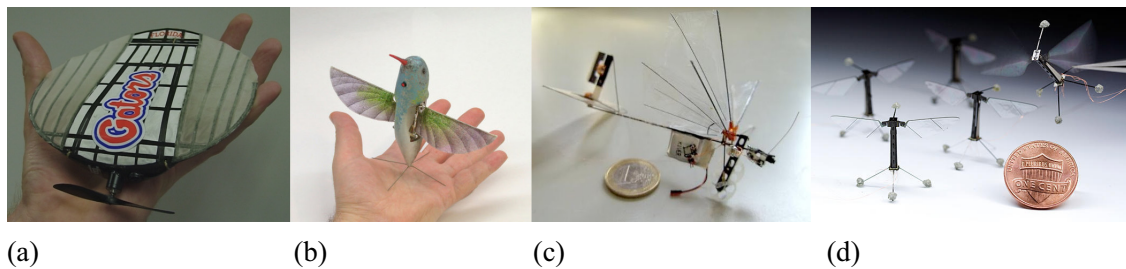


Figure 1-1. State of the art MAV designs (a) Fixed wing design from University of Florida [3]; (b) Nano Hummingbird from AeroVironment [4,6]; (c) DelFly form TU Delft [5,7]; (d) Robobees from Harvard [2].

Despite the attractive merits associated with MAVs, there are challenges in designing and improving current configurations. Their size, weight and flying speeds make them vulnerable to wind gusts. Their wings may deform significantly during flight. Aerodynamics, structural dynamics and flight dynamics are closely coupled with each other making MAVs a complex non-linear system that consequently poses considerable design challenges [1].

A closer look at Figure 1-1 reveals that some of the designs share resemblances with insects, birds and bats (see Figure 1-2). Such biological flyers are some of the most sophisticated flyers in nature. Not only are they comparable in size to the MAVs but also exhibit flight characteristics that we desire in our MAVs [1,8]. It is justified to be inspired from biological flyers because they perform extraordinary feats such as takeoff from

water and trees, landing upside down, flying in pouring rain [8], etc. They can glide, soar and hover [8]. Flapping wings are a common adaptation that is seen in almost all insects and birds.

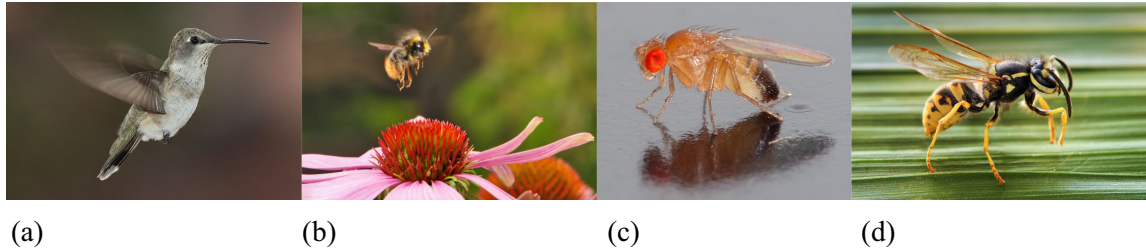


Figure 1-2. Biological flyers (a) Hummingbird (*Archilochus alexandri*) [9]; (b) Bumblebee (*Bombus pratorum*) [10]; (c) Fruit fly (*Drosophila melanogaster*) [11]; (d) Wasp (*Vespula germanica*) [12]. Pictures source: Wikimedia Commons. Pictures are under creative commons license.

Biological fliers use flapping wings to rapidly accelerate and decelerate in confined spaces [1]. They also showcase spectacular maneuvers to avoid obstacles and to conduct flight missions [1]. For example, a hummingbird utilizes coupled flapping wing and tail to quickly respond to wind gusts [1]. The wings of biological fliers are generally flexible and may substantially deform during flight [13]. As a result, the aerodynamics, structural dynamics, and flight dynamics are closely linked to each other [1]. Wing motions affect fluid forces on the wing, which in turn leads to changes in the wing shapes and motions. These highly coupled nonlinearities make a full understanding of the biological flight challenging [14].

To date, unsteady aerodynamics theories have been uncovered beyond the steady, stationary wing theories. Insects may utilize the clap and fling [15], delayed stall via prolonged leading edge vortices (LEVs) [16], wake-capture of a wing during the return

stroke [17,18], and rotational forces due to combined pitching and plunging to stay aloft [17,19]. These unsteady physical processes which are reviewed in Chapter 2 are particularly important for small fliers such as fruit flies, which operate at a Reynolds number $Re = Uc/\nu$ around $O(10^2)$, based on the mid-stroke velocity U , wing chord length c , and kinematic viscosity of air ν .

The Reynolds number for small birds such as hummingbirds is $Re = O(10^4)$, while for smaller insects, e.g. fruit flies or bees, $Re = O(10^2-10^3)$. The wings of these small insects are flexible and undergo large deformations, similar to bird and bat wings [20,21], (see e.g. fruit flies [22], flies (*Diptera*) [23], hoverflies [24], locust [25], etc.). In particular, an experimental study by Fontaine et al. [22] reports that a wing of fruit fly *Drosophila melanogaster* can undergo large deformations. A locust and a hawkmoth use wing deformations [24–26] to enhance the force generation and efficiency. Furthermore, several studies have suggested that insect wing rotations may be passive [23,27], where the resulting rotation is due to a dynamic balance between the wing inertial force, elastic restoring force, and fluid dynamic force.

Analysis of experimental measurements of honeybee flight [28] suggests that the kinematics of bees are less efficient than for example that of fruit flies. Fruit flies (*Drosophila*) exhibit large stroke amplitudes of 145-165 degrees, whereas numerous bee species (*Bombus*, *Xylocopa*, and Euglossine tribe) hover with shallow strokes, less than 130 degrees [28]. An ecological explanation is that bees consume floral nectar, providing power for ecologically useful but aerodynamically expensive behaviors, such as carrying payloads that may exceed their body mass [28]. Such low stroke amplitudes are less aerodynamically efficient as illustrated by a study of dynamically scaled rigid wing experiments [28,29].

Fruit fly and bumblebee wings are flexible [30]. The flexible wing design and the resulting passive deformations can enhance the lift and load-lifting capacities [31]. It is established that shape adaptation associated with flexibility can affect the effective angle of attack and hence the aerodynamic outcome [13]. Recent efforts have shown that wing flexibility can enhance propulsive force generation, while reducing the power consumption [13,32–34]. However, our understanding of fluid physics and the resulting structural dynamics has been insufficient to explain all the salient features of this coupled fluid-structure system.

Density ratio is a dimensionless parameter that characterizes the fluid-structure interaction of flexible wings. Density ratio is defined as $\rho^* = \rho_s/\rho_f$, where ρ_s is the wing density, and ρ_f is the density of the surrounding fluid, typically air has a density of 1.2 kg/m³. Therefore, the density ratio, relevant for natural fliers is of the order $O(10^3)$ [30,35]. A study of aeroelastic response of insect wings at a low density ratio system is justified as long as the resulting aeroelasticity matches the actual motion [13,36] as illustrated by analysis of a rigid wing with $\rho^* = 1.4$ [17], crane fly [27], and shown by the γ -scaling analysis [35]. However, a variation of the density ratio affects the resulting aerodynamic performance significantly [34]. The relationship between structural flexibility, flapping kinematics, and surrounding fluid has not been fully explored yet.

1.2 Research objectives

The overall objective of this study is to investigate the fluid-structure interaction (FSI) of fruit fly and bumblebee scale wings in hover. Buchwald and Dudley [37] reported that the bumblebees (Hymenoptera: *Bombus impatiens*) operate at Reynolds numbers between $Re = 1.6 \times 10^3$ and 3.0×10^3 , which is an order of magnitude higher than

that of fruit flies which operate at $Re = O(10^2)$. In this study, a comparison of hovering flexible wing aerodynamics is performed for $Re = 1.0 \times 10^2$ and 1.0×10^3 . The wing thickness normalized by the chord varied between 1.0×10^{-3} and 1.5×10^{-3} , which is a representative of bumblebee [14] and fruit fly wings [21], respectively. The density ratio, $\rho^* = \rho_s/\rho_f$, is set at $\rho^* = 2.0 \times 10^3$ [38] and $\rho^* = 1.0 \times 10^3$ [38] for a bumblebee and fruit fly, respectively. For these two scales, the amplitude of the plunge motion and the Young's modulus of the wing are varied to assess their effects on the aerodynamic performance and structural response. Moreover, the obtained performance metrics at the fruit fly and bumblebee scale with the γ -scaling relationship will be tested to verify whether any relation between lift and bending angle is universal in air and water as suggested by a recent study [39]. It has been shown in the past that aerodynamic performance scales with the dimensionless shape deformation parameter γ for a wide range of insects [35]. Despite the orders of magnitude at lower density ratio of water, the resulting wing displacements at the water tunnel scale resembled those of insects [13]. Relevant parameters of interest at bumblebee, fruit fly and water tunnel are tabulated in Chapter 3.

A carefully validated fully-coupled Navier-Stokes equation solver and a linear beam solver [35] are employed. The aeroelastic responses are reported on a design space with the frequency ratio f/f_1 and reduced frequency k as the design variables, where f is the motion frequency and f_1 is the first natural frequency of the wing in the chordwise direction.

The objectives of the research are as follows

- Report the aerodynamic performance and structural response at fruit fly scale and bumblebee scale where all relevant dimensionless parameters are from actual fruit fly

and bumblebee measurements. Recent experimental study with rigid wings [28] have suggested that bees (*Bombus hortorum* and *Bombus lucorum*) exhibit inefficient kinematics. This study verifies this trend for a particular bumblebee species (*Bombus impatiens*) for which experimental data is also available.

- Compare aeroelastic response at bumblebee and fruit fly scales against recently reported much lower density ratio results [13] (hence forth referred to as water tunnel scale). The scaling effects at these three insect scales, which differ by physical dimensions and operating conditions, are reported. The effects are assessed by systematically varying the motion amplitude and Young's modulus of the wing.

1.3 Thesis outline

Chapter 2 provides an overview of the aerodynamics and kinematics of insect flight along with definitions of important terminologies. In Chapter 3, the case setup and methodologies are introduced along with the design space, governing equations, numerical model and the computational grid. Chapter 4 presents the aeroelastic response at fruit fly and bumblebee scales. Aerodynamic and structural parameters are shown on the design space highlighting the trends. In Chapter 5, comparison of aeroelastic response at fruit fly and bumblebee scales is discussed. Vorticity contours at optimal points in the design space are discussed in detail to identify key mechanisms and their influence on the aeroelastic response. Quantitative comparison of numerical results with experimental data is also presented. This is followed by Chapter 6 with conclusions and recommendations for future work.

1.4 Content disclaimer

Majority of contents in this thesis including figures from Chapter 4 and 5 (Figure 4-1, Figure 4-2, Figure 4-3, Figure 4-4, Figure 4-6, Figure 4-8, Figure 5-1, Figure 5-2, Figure 5-3, Figure 5-6, Figure 5-6, Figure 5-7, Figure 5-8 and Figure 5-9) are taken from the following references [38,40], co-authored by the author.

- Sridhar, M. K. and Kang, C., “Aerodynamics of Flexible Flapping Wings at Bumblebee Scale in Hover Flight”, AIAA 2015-0254, 53th AIAA Aerospace Sciences Meeting, Kissimmee, Florida, January 5 - 9, 2015
- Sridhar, M. K. and Kang, C., "Effects of Flexible Wings in Hover Flight at Fruit Fly Scale," AIAA 2014-2311, 44th AIAA Fluid Dynamics Conference, Atlanta, Georgia, June 16 - 20, 2014

The author of this thesis has explicit permission from Chang-kwon Kang to reproduce the figures and text from the above publications in this thesis with appropriate citations.

CHAPTER 2

LITERATURE REVIEW

This chapter covers some of the important terminology that are associated with the theory of flapping wings. Section 2.1 covers definitions of key dimensionless parameters. Aerodynamics of insect flight is presented in Section 2.2 where unsteady lift enhancing mechanisms along with experimental observations are reviewed. Section 2.3 summarizes insect flight kinematics.

2.1 Terminology and dimensionless parameters

In this section, common terminology relevant to the current study is presented, including definitions of keywords and dimensionless variables extensively used throughout this work. Also see Chapter 5 for parameters specific to fruit fly (*Drosophila melanogaster*) and bumblebee (*Bombus terrestris*).

2.1.1 Hovering motion

In nature, hovering motion is restricted to insects and small birds. Animal size, moment of inertia of the wings and wing shape dictates whether it can hover or not [8]. In

hovering motion, the wing moves back and forth in an almost horizontal stroke plane. The type of hovering that is relevant in this study is *normal* hovering as seen in insects and hummingbirds, where the stroke deviation is so small that it is neglected. In normal hovering, lift is generated during the entire stroke [8]. Upper surface of the wing during the forward stroke becomes the lower surface during the backward stroke [8].

2.1.2 Dimensionless parameters for flexible flapping wing motion

Physical variables associated with a flexible wing are shown in Figure 2-1. The fluid density and dynamic viscosity are denoted by ρ_f and μ , respectively. U_{ref} is the reference velocity of the flow field. The wing geometry is characterized by its half span length R , thickness h_s and mean chord length c_m . The wing has a density of ρ_s and a Young's modulus of E . The geometric angle of attack is denoted by α . The parameters defined here are combined according to dimensional analysis resulting in dimensional numbers defined in Section 2.1.3.

2.1.3 Aeroelasticity

The forces that constitute the dynamic balance in aeroelasticity of insect or airplane wings are the aerodynamic force, structural dynamic force and inertial force. The three forces and their mutual interaction lead to various fluid-structure interaction phenomenon. Some of the common threats to integrity of structural components for passenger airplanes are flutter, limit cycle oscillations and dynamic response due to unsteady vortex shedding. Failing to address these issues may result in catastrophic failures. Flutter and eventual collapse of Tacoma Bridge is a famous example [41].

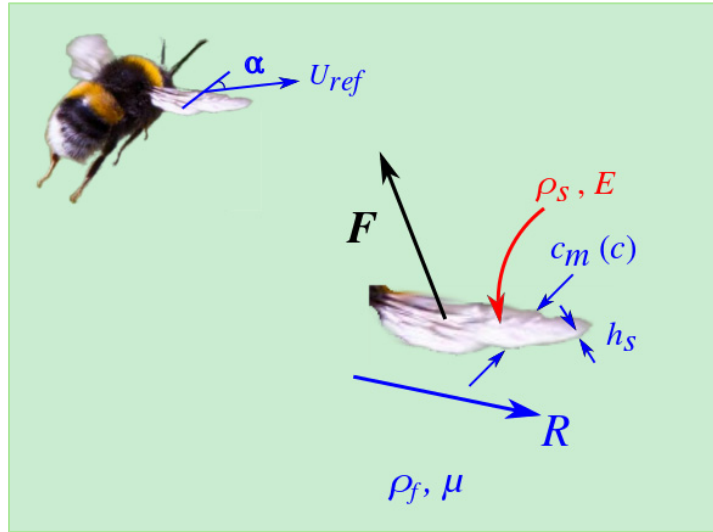


Figure 2-1. Physical variables of interest shown in reference to a bumblebee wing [42].

In the case of insect aerodynamics, wing flexibility can help generating high angles of attack, which directly enhance lift generation while reducing power [13,32–34]. Accurate measurements of forces and wing deformations of flexible flapping wings in air are still extremely challenging. The CFD/CSD coupled aeroelastic models can accurately represent the interaction between an elastic flexible wing of an insect and the surrounding fluid force [35]. These FSI numerical framework is often validated with experiments done in water tunnels [17–19] as the fluid dynamic forces in water are orders of magnitude greater than in air. The wing flaps under dynamic balance between inertial force, elastic force and the surrounding fluid dynamic force.

2.1.4 Scaling and dimensional analysis

Scaling refers to the process of constructing dimensionless scaling parameters and their functional relationships via Buckingham’s II theorem and dimensional analysis [43]. By this, we can reduce the usually large total number of involved parameters to as few as possible. It is also essential to perform dimensional analysis to maintain dynamic

similarity while conducting laboratory experiments. Additionally, the above process has led to additional useful parameters such as the shape deformation parameter γ [35], which can scale the time-averaged lift, power input, and efficiency of flexible flapping wings under different configurations. Section 5.4 discusses this parameter in greater detail.

2.1.5 Reynolds number

Reynolds number is a key dimensionless variable in fluid mechanics which is defined as the ratio of the inertial force to the viscous force as

$$Re = \frac{UL}{\nu} = \frac{2\pi fh_a c_m}{\nu}, \quad (2-1)$$

where L is a characteristic length scale and U is the characteristic velocity scale. In the current study, the mean chord length c_m is considered as the length scale and maximum translational velocity of the LE: $2\pi fh_a$ is considered as the reference velocity because in hovering motion there is no oncoming freestream flow (see Figure 2-1). The flapping frequency is denoted by f and h_a is the plunge amplitude. In insect flight, Reynolds number typically range from $O(10^1)$ to $O(10^4)$ and at this regime, the unsteady, inertia, pressure and viscous forces are all important [8].

2.1.6 Reduced frequency

Reduced frequency is a dimensionless variable which is a measure of unsteadiness in the flow field [8]. For two dimensional hovering wings, the reduced velocity can be defined as

$$k = \frac{2\pi fc_m}{2U} = \frac{c_m}{2h_a} \quad (2-2)$$

At higher k , unsteadiness is higher, where the inertial effects are more important than the viscous effects at a constant Reynolds number. At lower k , viscous effects dominate the inertial effects.

2.1.7 Strouhal number

Strouhal number is an important dimensionless parameter which is often associated with flows involving unsteady vortex shedding. Von Karman vortex shedding behind a cylinder is characterized by Strouhal number. In case of flapping aerodynamics, Strouhal number describes the ratio between wing velocity and the characteristic velocity [8]. It is defined as follows

$$St = \frac{fL}{U} = \frac{2fh_a}{U}. \quad (2-3)$$

For hovering flapping wings, St is a constant because the reference velocity is based on flapping velocity.

2.1.8 Frequency ratio

Frequency ratio is the measure of the wing flexibility and is defined as the ratio of the flapping frequency f and the first natural frequency of the wing f_1 . Natural frequency is measured in the chordwise direction between LE and TE of the wing [13]. For a linear beam, the frequency ratio can be rewritten in terms of reduced frequency, k , and Young's modulus, E , as

$$\frac{f}{f_1} = \frac{2\pi f}{[k^2 \{Eh_s^{*2} / (12\rho_s c^2)\}^{0.5}]}, \quad (2-4)$$

where $h_s^* = h_s/c$ is the thickness ratio and $\rho^* = \rho_s/\rho_f$ is the density ratio.

2.1.9 Effective stiffness

Effective inertia is obtained by normalizing wing stiffness by the fluid dynamic variables as [1,35]

$$\Pi_1 = \frac{Eh_s^{*3}}{12\rho_f U_{ref}^2}. \quad (2-5)$$

The numerator gives the elastic bending force and the denominator gives the fluid dynamic force. Parameter Π_1 indicates the ratio between wing stiffness and the dynamic pressure.

2.1.10 Shape deformation parameter

Shape deformation parameter γ is an indication of relative deformation of the LE with respect to TE and is defined as follows [13,35]

$$\gamma = \frac{\left\{1 + \frac{4}{\pi} \rho^* h_s^*\right\} Stk}{\Pi_0 ((f_1 / f)^2 - 1)}, \quad (2-6)$$

where $\Pi_0 = \rho^* h_s^* (k/\pi)^2$ is the effective inertia term. Shape deformation parameter measures the wing deformation due to the dynamic balance between the aerodynamic force, elastic restoring force, and wing inertial force. The TE displacement relative to LE can be seen as passive pitch, an effective angle of attack.

2.2 Aerodynamics of insect flight

2.2.1 Unsteady mechanisms

Flapping wing aerodynamics is characterized by a complex two-way interaction between the wing and the surrounding fluid. This inherently unsteady mechanism, which is commonly seen in biological flyers, is closely related to the wing shape, wing flexibility and the vortices shed from the wing. Over the years, modern flow visualization and experimentation techniques have helped us in understanding these complex mechanisms [44]. In the following section, four important unsteady mechanisms that enhance overall aerodynamic performance in flapping flight are introduced. For unsteady flows at low Reynolds numbers, a commonality is found in the formation of vortices on and around the wing and their non-linear interaction with the wing.

2.2.1.1 Clap-and-fling

The clap and fling mechanism was first introduced by Weis-Fogh [15] to explain the flight of a chalcid wasp (see also Figure 2-2). As the name suggests, this mechanism consists of two maneuvers: *Clap* (Figure 2-2 a-c), where the wings approach each other decreasing the gap between them and *Fling* (Figure 2-2 d-f), where the wings are pushed apart resulting in formation of LEVs. During *Clap*, as the wings approach each other, fluid between the wings is pushed out resulting in TEVs which act as stopping vortices. This results in additional propulsive force. On the other hand, during *Fling*, the wing rotates around the TE which causes the fluid to rush back into the gap formed between the wings. As the fluid fills the gap, it rolls up near the LE in a direction which contributes to the total lift generation. In Figure 2-2, the light blue lines correspond to the

magnitude and direction of the net force. Dark blue arrows correspond to the direction of the induced velocity. It is believed that this mechanism can result in modest, but significant lift enhancement [45].

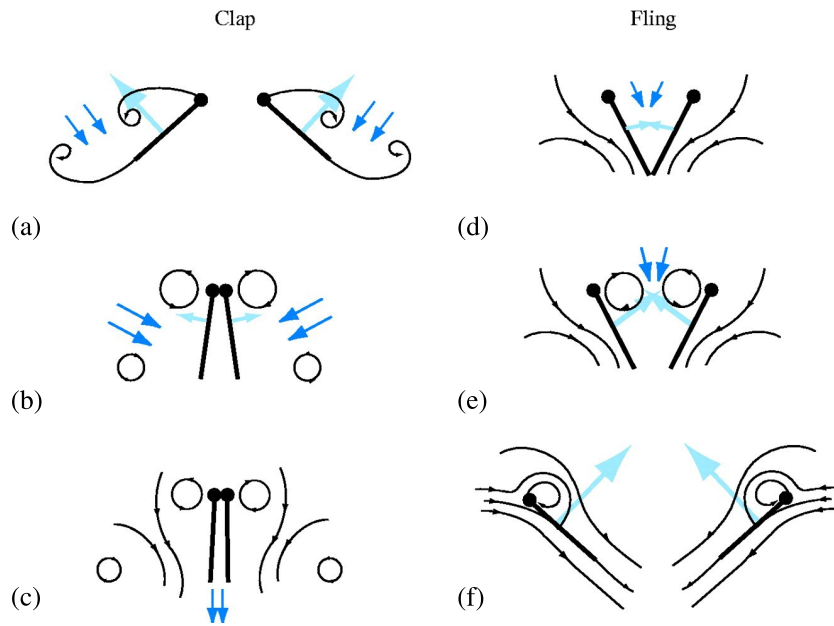


Figure 2-2. Schematic of clap-and-fling mechanism. A-C represents *clap* where wings come closer and D-F represents *fling* where wings move away from each other. Light blue arrows represent force magnitude and direction whereas dark blue arrows indicate induced velocity. Reproduced with permission from ref. [45].

2.2.1.2 Delayed stall of the leading edge vortices

Leading edge vortices (LEVs) are considered to be the one of the most important flow features associated with aerodynamics of insect flight [16,45]. Figure 2-3(b) shows the streamlines over an insect wing cross section at an angle of attack and the corresponding LEV.

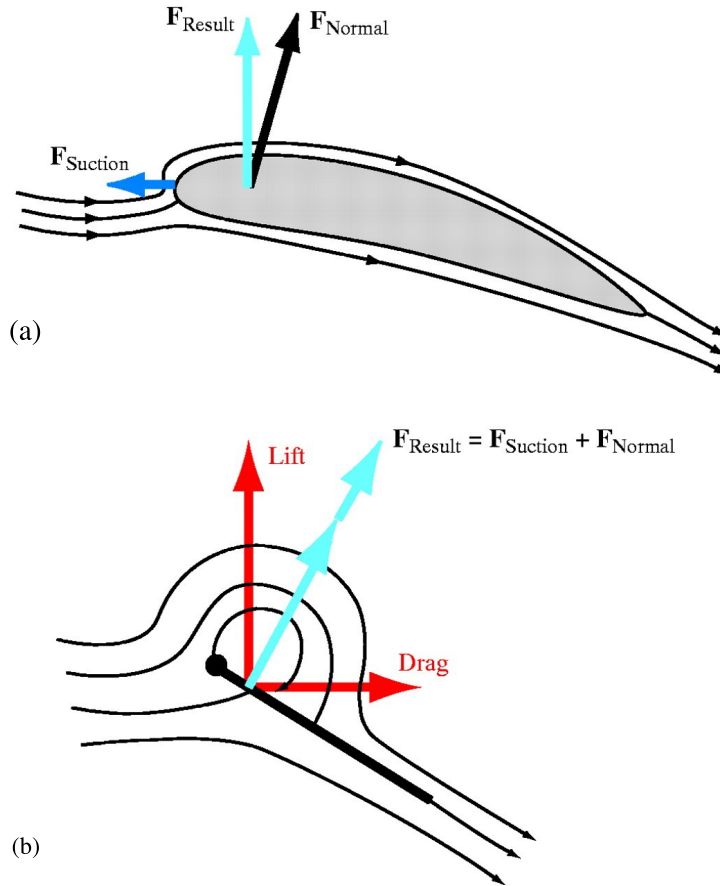


Figure 2-3. Schematic of leading edge suction. (a) The resultant force on a blunt airfoil is perpendicular to the freestream direction due to the suction force acting parallel to the flow. (b) On a thin airfoil such as insect wing, the suction force acts normal to the wing surface due to presence of LEV, thus enhancing the resultant lift. Reproduced with permission from ref. [45].

As the fluid flows over the wing, it separates at the sharp LE and forms a vortex which remains attached to the rest of the wing length. This vortex at the LE of the wing is known as the LEV and it has a positive effect on the lift generated due to its lower pressure core, creating additional suction. When the force vectors are superimposed on the wing, it is seen that the direction of the suction force is tilted due to the presence of the vortex and it *adds* to the normal force on the wing section, thus enhancing the resultant force. On a conventional finite thickness wing, as shown in Figure 2-3(a), the

suction force due to turning of the fluid would act perpendicular to the freestream. The wing orientation as shown in Figure 2-3(b), is not exaggerated. It is common for wings to continue to exhibit high angles of attack during a flapping stroke. As long as the vortex remains attached to the wing, it imparts momentum to the fluid in the downward direction which results in higher lift force. But for some kinematics, the vortex can become unstable and detach from the wing. When the LEV convects away from the wing, the lift generated is not as high as before. The presence of a vortex at the LE of the wing which results in higher lift forces is also termed as *delayed stall* [45]. A schematic of a two dimensional wing in translation, showing the evolution of LE and TE vortices is shown in Figure 2-4.

2.2.1.3 Tip vortex

The tip vortex in unsteady flows can influence the total force exerted on the wing in the following ways [1]:

- creating a low pressure near the wing tip.
- interacting with a LEV.
- constructing a wake structure by downward and radial movement of the root vortex and TiV.

TiVs can either promote or make little impact on the aerodynamics of low aspect ratio flapping wings [1]. A study conducted in 2009 [46] reports that for a low aspect-ratio flapping wing, tip vortices can increase lift both by creating a low-pressure region near the wing tip and by anchoring the leading-edge vortex (LEV) to delay or even prevent it from shedding.

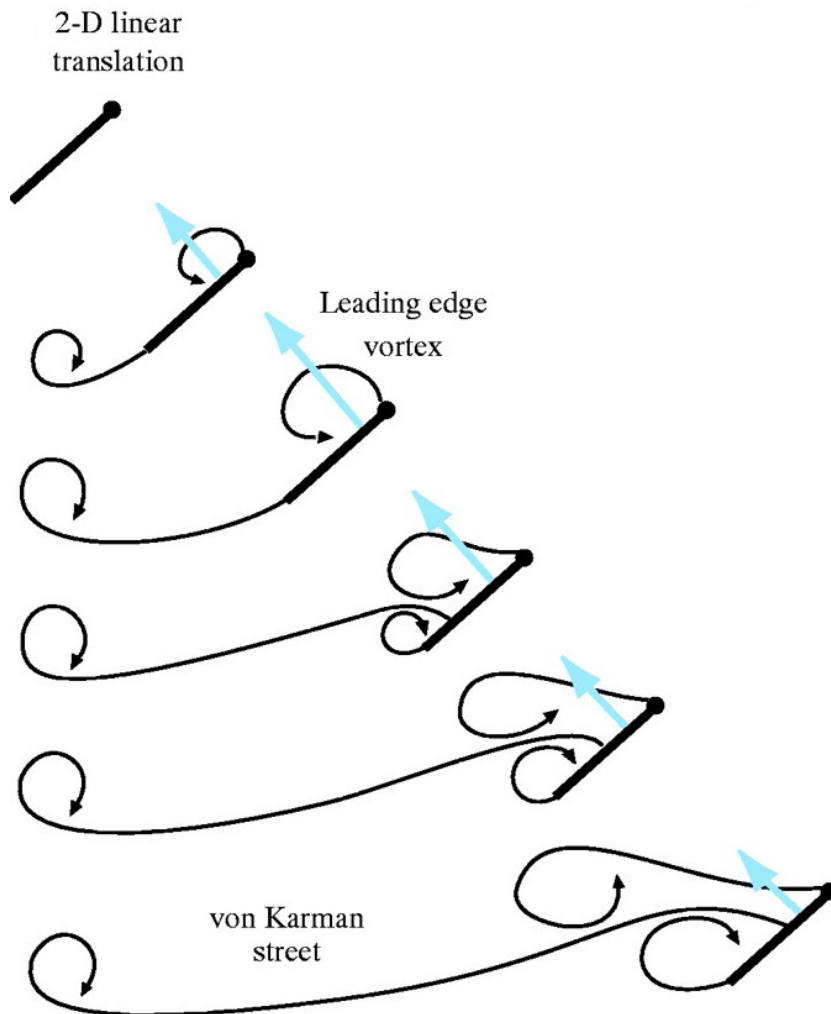


Figure 2-4. Evolution of LEV and TEV on a two dimensional translating wing. LEV and TEV are shed alternatively to constitute a von Karman vortex street. Magnitude of the aerodynamic force (blue arrows) varies during the motion with highest force observed when a well-defined LEV is formed at the suction side of the wing. Reproduced with permission from ref. [45].

2.2.1.4 Wake capture

Insect wing motion involves two phases: upstroke and downstroke. Wing pronation occurs at the end of the upstroke when the wing reorients itself to begin the downstroke. Similarly, wing supination occurs when the wing transitions from the downstroke to upstroke. During pronation and supination, the wings are flipped in the

opposite direction in a very short amount of time. Vortices, shed from the edges of the in the previous stroke, can interact with the wing in the return stroke, leading to an intriguing nonlinear wing-wake interaction for flapping wings. A schematic of this interaction is shown in Figure 2-5 where a wing cross section initially moving to the right flips its direction and comes in contact with a vortex shed in the previous stroke. As the wing interacts with the detached vortex, a peak is seen in the lift history. This non-linear wing-wake interaction which results in increase of lift is known as *wake capture*. Depending on the wing kinematics and orientation, the lift can also suffer from the wing-wake interaction [13].

2.2.2 Effects of flexibility

2.2.3 Experimental observations

Insects flap their wings at high frequencies, greater than $O(10^1)$ Hz. For example, a fruit fly (*Drosophila melanogaster*) beats its wing at around 218 Hz [47] and a bumblebee (*Bombus impatiens*) beats its wings at 181 Hz [37]. When combined with the small physical scales poses a challenge in terms of extracting the wing kinematics and flow behaviors experimentally. In addition to this, because insects rely on visual feedback, care must be taken not to affect the insect behavior [45]. However, with modern advancements in flow visualization techniques such as DPIV (Digital Particle Image Velocimetry) and high-speed photography, experimentalists have been able to duplicate the actual insect kinematics. To estimate the forces, these kinematics are produced with dynamically scaled robotic models on which the aerodynamic forces are measured [17,47,48]. However, achieving dynamic similarity for flapping motions in air

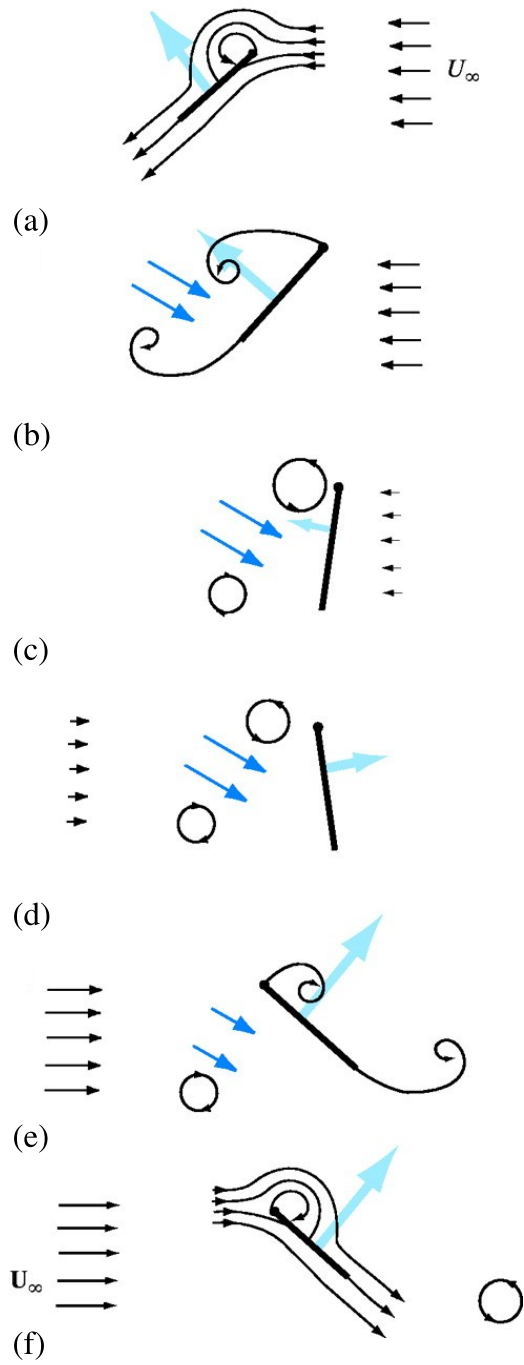


Figure 2-5. A Schematic of wing-wake interaction. Reproduced with permission from Ref. [45].

is extremely challenging in water due to the orders of magnitudes difference in the density for flexible flapping wings.

A second approach is to use computational fluid dynamics (CFD) methods to simulate the wing motion. The kinematics extracted from actual insect motion serves as input to the computational model which solves full Navier-Stokes equations which in turn provide fundamental basis for simulating forces from the measured kinematics [45]. A full description is provided in Section 3.2. One of the first CFD simulations of flapping wing flight was done by Liu et al. in 1998 [49]. They studied the unsteady aerodynamics and instantaneous force production of a hovering hawkmoth (*Manduca sexta*). This has since been followed by numerous other CFD simulations both in two [50] and three dimensions [51–53]. A comprehensive list of references related to CFD simulations of insect flight is compiled in Refs. [1,8].

2.3 Kinematics of insect flight

Flapping wing kinematics is the result of wing and body movements. A schematic of the angles associated with a three dimensional wing motion is shown in Figure 2-6. The angles which define the kinematics of flapping wings [8] are:

- a) Body angle (χ)– Inclination of the body to the horizontal plane
- b) Stroke plane angle (β) – Defined by the wing base and the wing tip of the maximum and minimum sweep positions [1]

Three dimensional wing beat kinematics can be described by three angles relative to the stroke plane angle:

- a) Positional or flapping angle (ϕ) – Flapping about x -axis

- b) Elevation angle (θ) – Wing rotation around z -axis
- c) Feathering angle or Angle of Attack (α) – Wing rotation about y -axis

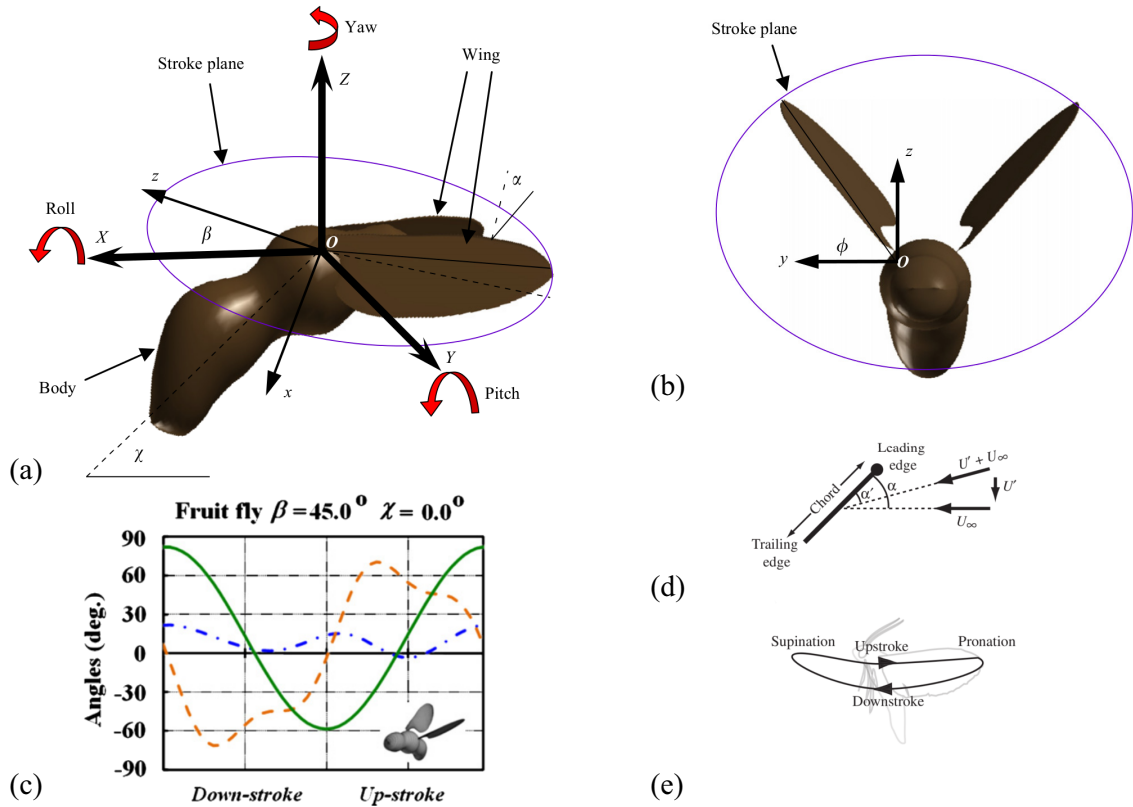


Figure 2-6. Schematics showing the kinematics of flapping insect flight [1]. (a,b) Positional angle, angle of attack and elevation angle are represented by ϕ , α and θ , respectively. (c) Time history of evolution the three angles in a hovering flight [1] where ϕ is in green, α is in orange and θ is in blue. (d) Schematic illustrating the difference between geometric and aerodynamic angle of attack. Reproduced with permission from ref. [45]. (e) Schematic illustrating upstroke and downstroke. Reproduced with permission from ref. [45].

Figure 2-6(c) shows time history of flapping, elevation and angle of attack associated with a fruit fly. Positional angle follows a sinusoidal shape. Elevation angle has the lowest amplitude. The geometric angle of attack is asymmetric and includes the high frequency component of flapping frequency.

For two-dimensional wing motions, the plunging motion can be described by

$$h(t) = h_a \sin(2\pi ft + \varphi), \quad (2-7)$$

where h_a is the plunge amplitude, f is the plunging frequency and φ is the phase difference between pitching and plunging motion. Depending on the magnitude of the phase difference, three types of rotational modes can be defined: advanced ($\varphi > 90^\circ$), symmetric ($\varphi \approx 90^\circ$) and delayed ($\varphi < 90^\circ$). Figure 2-7 shows the three rotational modes for a wing motion along x -axis. A synchronized motion is characterized by vertical wings at the end of each stroke.

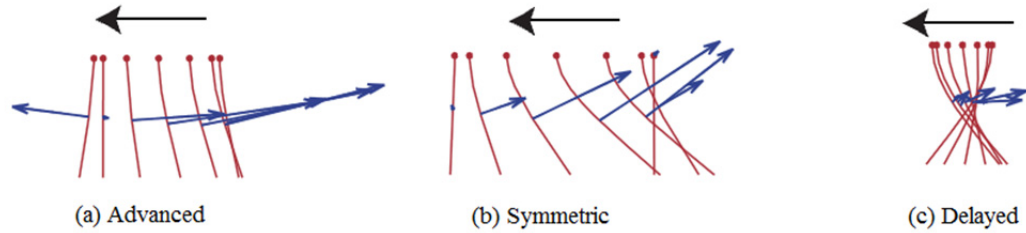


Figure 2-7. Three types of rotational modes observed in flapping flight [14]. Black arrow represents the direction of wing motion and blue arrows represent the pressure force direction and its magnitude.

In fixed wing terminology, angle of attack (or *geometric* angle of attack) refers to the angle made by the airfoil chord with the freestream velocity direction. However, in unsteady flows, there is no single angle of attack at each wing section since the flow direction varies along the chord [1]. For forward flight studies deal with a quantity called *aerodynamic* angle of attack, α_e defined [1] as

$$\alpha_e = \tan^{-1} \left(\frac{-\dot{h}}{U_\infty} \right) - \alpha \quad (2-8)$$

where U_∞ is the freestream velocity and \dot{h} is the velocity due to plunge motion, perpendicular to the freestream. A schematic of the difference between geometric and aerodynamic angle of attack is shown in Figure 2-6(d). For hovering motion, since there is no freestream, the instantaneous angle between the chord of the wing and the plunge direction is considered as the angle of attack.

CHAPTER 3

METHODS

3.1 Case setup and governing equations

Fruit fly and bumblebee wings are three-dimensional and highly anisotropic with diverse vein structures as seen in Figure 3-1(a). The wing thickness varies across span and chord. Moreover, the wing motion is three-dimensional with a wing rotation at the wing root. In addition, studies of neuromuscular control indicate that flies can actively modulate stroke deviation by altering the activity of steering muscles [54,55]. While normal hovering with a flat plane strokes are observed, flies often exhibit U-shaped trajectories [29].

In this study, a normal hovering motion is considered, neglecting any stroke deviation angles. For our purpose, it is sufficient to address only the chordwise flexibility and represent the flexible wing as a homogeneous elastic flat plate [30,35], with the plunge motion imposed at the leading edge to represent the leading edge vein [56]. While three-dimensional effects, such as spanwise flow, that seem to stabilize the LEVs [57] or LEV-tip-vortex interaction [46] are noticeable in general for flapping wings, the

chordwise flexibility is essential and warrants this independent study [1]. Also, the characteristics of the LEVs in two-dimensions for plunging motions are representative of three-dimensional flapping wings as long as the stroke-to-chord ratio is within the range of typical insects, *i.e.* around 4 to 5 [58–60], which is considered in this study.

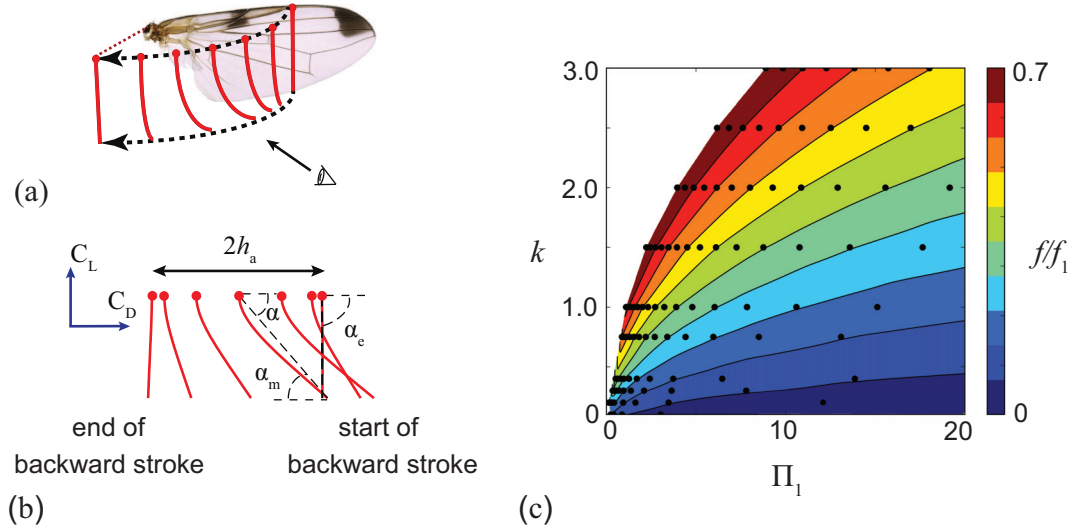


Figure 3-1. Wing motion and design space [38]. (a) Front view of a fruit fly wing with solid lines representing two dimensional wing section. (b) Schematic of the wing motion with amplitude h_a . The angles at mid and end of the strokes are α_m and α_e , respectively. Lift and drag directions are indicated relative to the wing orientation. Red dot corresponds to leading edge of the wing. (c) Considered design space in terms of effective stiffness Π_1 and reduced frequency k . The contours represent frequency ratio and dots are the test points.

A sinusoidal plunge motion h with amplitude h_a and frequency f (see Figure 3-1(b)) is imposed on the leading-edge (LE) of the wing as function of time, t , by

$$h(t) = h_a \cos(2\pi ft). \quad (3-1)$$

In the absence of a free-stream for hovering wings, the maximum translational velocity U of the flat plate at the LE is set as the reference velocity, such that $U = 2\pi fh_a$ [13,28,61]. Note that reduced frequency k in hover becomes a geometric quantity:

$k = \pi c/U = c/(2h_a)$. The Strouhal number, another important parameter in flapping wing aerodynamics, becomes a constant for hovering motions due to the absence of freestream: $St \sim fh_a/U = 1/(2\pi)$.

A dimensionless flow field is considered. The flow is initiated by the hovering motion, equation (3-1). The flow field is governed by the unsteady Navier-Stokes equations with constant fluid density ρ_f and viscosity μ ,

$$\begin{aligned} \nabla^* \cdot \mathbf{u}^* &= 0 \\ \frac{k}{\pi} \frac{\partial \mathbf{u}^*}{\partial t^*} + (\mathbf{u}^* \cdot \nabla^*) \mathbf{u}^* &= -\nabla^* p^* + \frac{1}{Re} \Delta^* \mathbf{u}^* \end{aligned} \quad (3-2)$$

where the velocity field is \mathbf{u} , pressure is p , and time is t . The superscript (*) indicates dimensionless variables. The dimensional variables are non-dimensionalized with a reference velocity U , inverse of the motion frequency $1/f$, and chord c , respectively.

A two-dimensional, elastic wing structure is considered with uniform thickness h_s and density ρ_s and Young's modulus E . Thickness ratio of $h_s^* = h_s/c = 1.5 \times 10^{-3}$ and 1.0×10^{-3} are considered, motivated by the fruit fly [62] and bumblebee wing [37], respectively. The plate is modeled as a Euler-Bernoulli beam with 51 nodes equally distributed over the plate with flat edges [13]. As the flat plate follows the imposed horizontal motion at the LE, the resulting fluid dynamic force dynamically balances with the wing inertia and the elastic bending forces, modeled locally as a linear Euler-Bernoulli beam as

$$\Pi_0 \frac{\partial^2 v^*}{\partial t^{*2}} + \Pi_1 \Delta^{*2} v^* = F^*, \quad (3-3)$$

where v is the displacement due to bending motion, $\Pi_0 = \rho^* h_s^* (k/\pi)^2$ is the effective inertia, the inertia of the wing normalized by the fluid dynamic variables [35], and

$\Pi_1 = Eh_s^*/(12\rho_f U^2)$ is the effective stiffness, the wing stiffness normalized by the fluid dynamic variables [35], and F is the distributed transverse fluid force per unit length on the wing, such that $F^* = F/(\rho_f U^2)$. The resulting wing camber deformations $w = v-h$ can also be regarded as a pitch rotation $\alpha(t^*)$, the angle between the trailing-edge (TE) and LE (see Figure 3-1(b)).

The density ratio of fruit fly and bumblebee wing and air are approximately $\rho^* = 2.0 \times 10^3$ [37] and $\rho^* = 1.0 \times 10^3$ [35], respectively. The remaining dimensionless parameters, i.e. the frequency ratio f/f_1 and the reduced frequency k , are varied by changing the Young's modulus E and the plunge amplitude h_a , respectively, to probe their influence on the resulting aerodynamics and the structural deformations. The range selection of h_a is motivated by the plunge amplitudes observed in biological fliers [27,58]. It is reported in the literature that the natural fliers operate at a sub natural frequency range: $f/f_1 \leq 0.8$ [32], and in this study, the Young's modulus is adjusted, such that the frequency ratio is at a similar range: $0.04 \leq f/f_1 \leq 0.7$. Table 3-1 summarizes the involved dimensionless parameters and their range. The design space employed at bumblebee scale is the same as that at fruit fly scale. Moreover, for a consistent comparison against the aeroelastic response at water tunnel scale $\rho^* = 7.8$ [63], the effective stiffness Π_1 is considered instead of f/f_1 which can be uniquely expressed in terms of k and f/f_1 , to represent the design space, as shown in Figure 3-1(c).

The structural response can be converted in a passive pitch angle by measuring the TE displacement relative to the LE [63]. Passive pitch angle acts as an effective angle of attack, measured in terms of the angular amplitude α_a and the phase lag φ . Analysis of the time history of the wing deformations from the high-fidelity solution [63] shows that the angle of attack due to passive pitch can be approximated by a first-order harmonic as

$$\alpha_{FH} = 90^\circ - \alpha_a \cos(2\pi t^* + \varphi). \quad (3-4)$$

Table 3-1. Comparison of the dimensionless parameter values at bumblebee, fruit fly and water tunnel [13] scales. The design variables are the reduced frequency k and the frequency ratio f/f_1 .

	Bumblebee	Fruit fly	Water tunnel
Reynolds Number, Re	1.0×10^3	1.0×10^2	1.0×10^2
Density ratio, ρ^*	2.0×10^3	1.0×10^3	7.8
Thickness ratio, h_s^*	1.0×10^{-3}	1.5×10^{-3}	2.0×10^{-2}
Reduced frequency, k	0.1, 0.2, 0.3, 0.4, 0.75, 1.0, 1.5, 2.0, 2.5, 3.0	same	$0.25 < k < 3.75$
Frequency ratio, f/f_1 (Motion amplitude, h_a)	20 equally spaced values $\in [0.04, 0.7]$ (0.17 to 5.0)	same	$0.06 < f/f_1 < 0.82$
(Young's Modulus, E)	$(3.38 \times 10^8 \text{ to } 5.26 \times 10^{13})$		

The departure from the first-order sinusoidal motion increases with increasing wing deformations. Here, the wing deformations at the TE of the wing is determined at the middle and the end of the strokes, $w_m = w^*(0.25)$ and $w_e = w^*(0.5)$, where again $w = v \cdot h$ is the wing deformation relative to the imposed plunge motion h at the LE. The relative wing deformations are converted to passive pitch angles α as $\alpha_m = \arctan(w_m)$ and $\alpha_e = \arctan(w_e)$. Based on these two angles, a first-order harmonic approximation can be constructed for the passive pitch, equation (3-4), by solving for the phase lag φ and the angular amplitude α_a with $\alpha_{FH}(0.25) = \alpha_m$ and $\alpha_{FH}(0.5) = \alpha_e$.

Parameters of interest for the aerodynamic performance are also expressed in dimensionless quantities. The lift and drag coefficients are defined as

$$C_L = \frac{L}{\frac{1}{2} \rho_f U^2 c} \quad \text{and} \quad C_D = \frac{D}{\frac{1}{2} \rho_f U^2 c}, \quad (3-5)$$

where L and D are the lift and drag per unit span (see Figure 3-1(b)). Lift is required to stay aloft in air, while drag is responsible for a part of the power consumption. An overbar notation indicates time-averaging, which is defined as

$$\bar{C}_L = \frac{f}{4} \int_{m/f}^{(m+4)/f} C_L(t) dt, \quad (3-6)$$

for example for the lift coefficient C_L . The resulting forces in this study are not exactly periodic in time and to have a representative value for the time averaged force and to avoid initial transient effects. Thus, $m = 6$ is considered. The time averaged values are averaged over four motion cycles. For a more comprehensive treatment of the dimensional analysis and non-dimensionalization, refer to Kang et al. [64].

To measure the cost of performance, the time-averaged power input is defined as

$$\bar{C}_P = \frac{f}{4} \int_{m/f}^{(m+4)/f} C_D(t) \dot{h}(t) dt, \quad (3-7)$$

where \dot{h} is the plunge velocity of the wing, measured at the LE of the wing. The time-averaged power input is also called the mean profile power [29]. The dimensionless parameter \bar{C}_P is a better representation of the cost of performance than \bar{C}_D . The reason is that the time history of drag is almost symmetric through the two half-strokes in one motion cycle. Regardless of the maximum value of C_D within a motion cycle, \bar{C}_D would become zero if C_D was purely symmetric. For the range of Reynolds numbers relevant for fruit flies, the total mechanical power required to flap the wings is dominated by the time-averaged power input, which is the cost to overcome drag on the flapping wings [65].

The ratio between the time-averaged lift coefficient and the time-averaged power input gives a metric for the propulsive efficiency, which is called efficiency η . The efficiency η is defined as

$$\eta = \frac{\bar{C}_L}{\bar{C}_P}. \quad (3-8)$$

For a dynamically-scaled, rigid, fruit fly wing, the efficiency varied extensively, even within sub regions of the parameter maps in which the values of lift are high enough to support flight [29]. While, this ratio is called the propulsive efficiency, the resulting value can be higher than 1. For a rigid, dynamically-scaled fruit fly wing, the efficiency varied between -4 and 4 [29].

3.2 Numerical framework and solver functionalities

The fluid-structure interaction is based on a time-domain partitioned solution process in which the partial differential equations governing the fluid and the structure are solved independently and spatially coupled through the interface between the fluid and the structure [35]. An interface module is added to the fluid solver to communicate the parallelized flow solutions on the three-dimensional wetted surface to and from the serial structural solver. At each time step the fluid and the structural solvers are called one after the other until sufficient convergence on the displacements on the shared boundary surface are reached in an inner-iteration before advancing to the next time step [64].

The governing equations for the fluid given by equation (3-2) are solved using an in-house three-dimensional, unstructured, pressure-based finite volume solver [66,67] written in a rule-based framework [68]. The geometric conservation law [69] is satisfied [70]. Radial basis function interpolation method used to deform the computational mesh (see Figure 3-2) at each time step [71]. The spatial and temporal sensitivity studies at $Re=1.0\times 10^3$ as well as the computational setup are shown in Kang and Shyy [63].

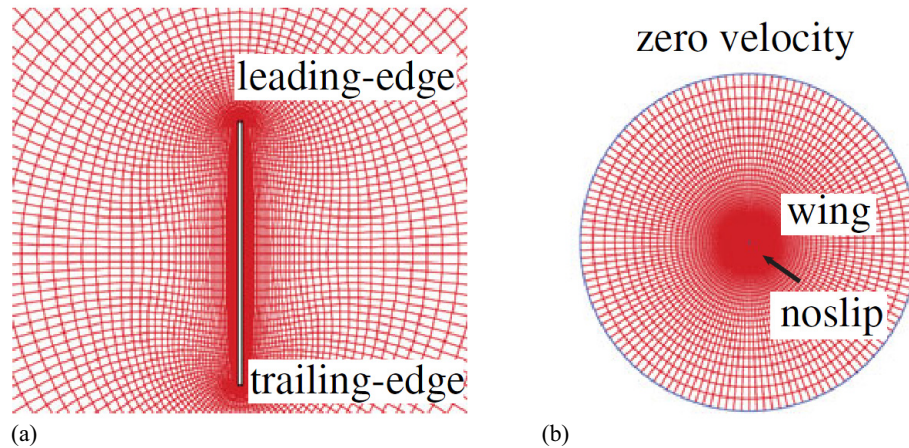


Figure 3-2. (a) Computational domain and mesh around the flat plate [13]. (b) Imposed boundary conditions for the fluid flow. The wing is placed at the center of the computational mesh in (b). The outer boundary is located 63 chord lengths away from the flat plate. There are 61×9 cells on the chord and edges of the flat plate.

The dynamics of the wing structure given by equation (3-3) is solved using a finite element representation. The structural damping is not considered in this study. Two degrees of freedom, namely the displacement and bending, are allowed at each node. Computations performed for an airfoil composed of a rigid teardrop and elastic flat plate at higher Reynolds number and for various motion frequencies [35] showed that a linear Euler-Bernoulli beam is sufficient for qualitative analysis of the fluid-structure interaction coupling. The flat plate is modeled with 51 nodes equally distributed over it.

The FSI coupling is a time-domain partitioned solution process. The governing partial differential equations for the fluid and the structure are solved independently and coupled spatially through the interface between the fluid and the structure. At each time step the flow field is iterated and the structural displacement field such that sufficient convergence on the deformed wing displacement is achieved, before advancing to the next time step. In order to accelerate and ensure the convergence of the FSI the Aitken relaxation method has been incorporated [64]. Full details of this algorithm and careful

validation analysis against well-documented experimental results can be found in Refs [64,72–74]. A flowchart illustrating this coupling is shown in Figure 3-3.

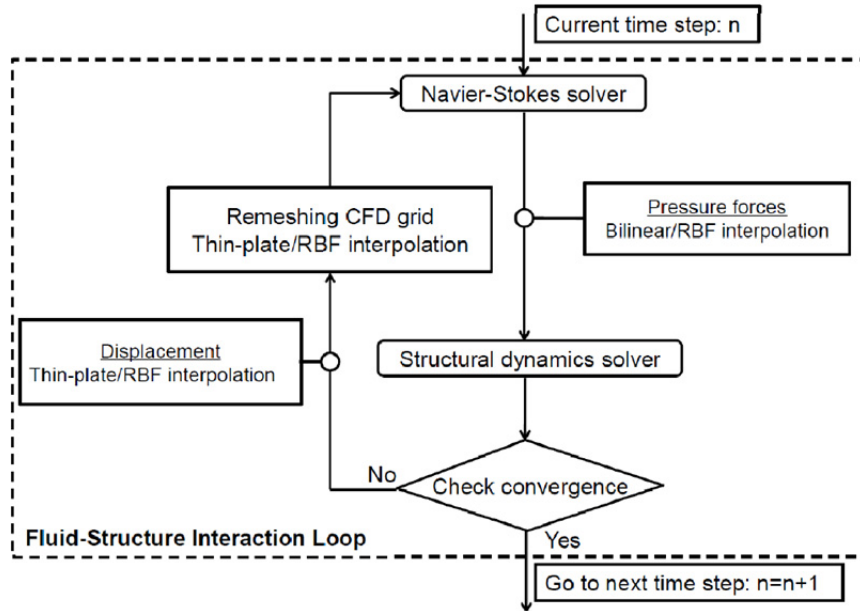


Figure 3-3. Flowchart illustrating the Fluid Structure Interaction loop [75].

3.3 Assumptions

An actual insect wing shown in Figure 3-1(a) is highly anisotropic and complex. In this study, a two dimensional approximation of an actual three dimensional wing is considered. The two dimensional wing is approximated by a flat plate with a uniform thickness based on actual insect measurements. By imposing a hovering motion at the LE of the wing, the wing deforms as it moves and we focus on chordwise deformation. The imposed hovering motion at the LE, equation (3-1), follows a straight line without any stroke deviations. Insect wings in three dimensional exhibit stroke deviations in the form of figure-of-eight motion. A first order harmonic approximation, equation (3-4), of wing motion is considered for calculating α_a and ϕ . Wing camber is modeled in CFD

simulation but is not included in the analysis in Chapter 5. In an earlier study [63] it was concluded that wing camber deformation is negligible when the wing deformation is small, but as flexibility increases, the wing camber also becomes important. An abstracted and simplified representation of the actual wing motion enables us to explain the first order mechanisms that enable flight in low Reynolds number flight.

CHAPTER 4

RESULTS

Aeroelastic response at fruit fly and bumblebee scales in air is studied to assess the similarities and differences at both scales. A two dimensional hovering motion of a flexible flapping wing is considered and the resulting coupled relationship between wing flexibility, kinematics and surrounding fluid dynamic forces is explored. Key aerodynamic parameters such as lift coefficient, power, efficiency and structural parameters angular amplitude and phase lag, are evaluated in a two dimensional design space. In this chapter, the aforementioned parameters for fruit fly and bumblebee are presented in Sections 4.2 and 4.3, respectively. While the aerodynamic and structural dynamic responses at the fruit fly scales are almost periodic, the responses at bumblebee scales are non-periodic, which is reported in Section 4.3.3. Effects of normalization of lift coefficient is presented in Section 4.3.4.

4.1 Aeroelastic response at fruit fly scale

4.1.1 Aerodynamic performance at fruit fly scale

The variation of aerodynamic performance with frequency ratio ff_1 at varying reduced frequency k is presented in Figure 4-1. A frequency ratio range $ff_1 \leq 0.7$ and reduced frequency of $0.1 \leq k \leq 3.0$ is considered. See also Table 3-1 for the individual values. The maximum and minimum values of k corresponds to minimum and maximum plunge amplitudes of $h_a = 0.16$ and $h_a = 5.0$, respectively.

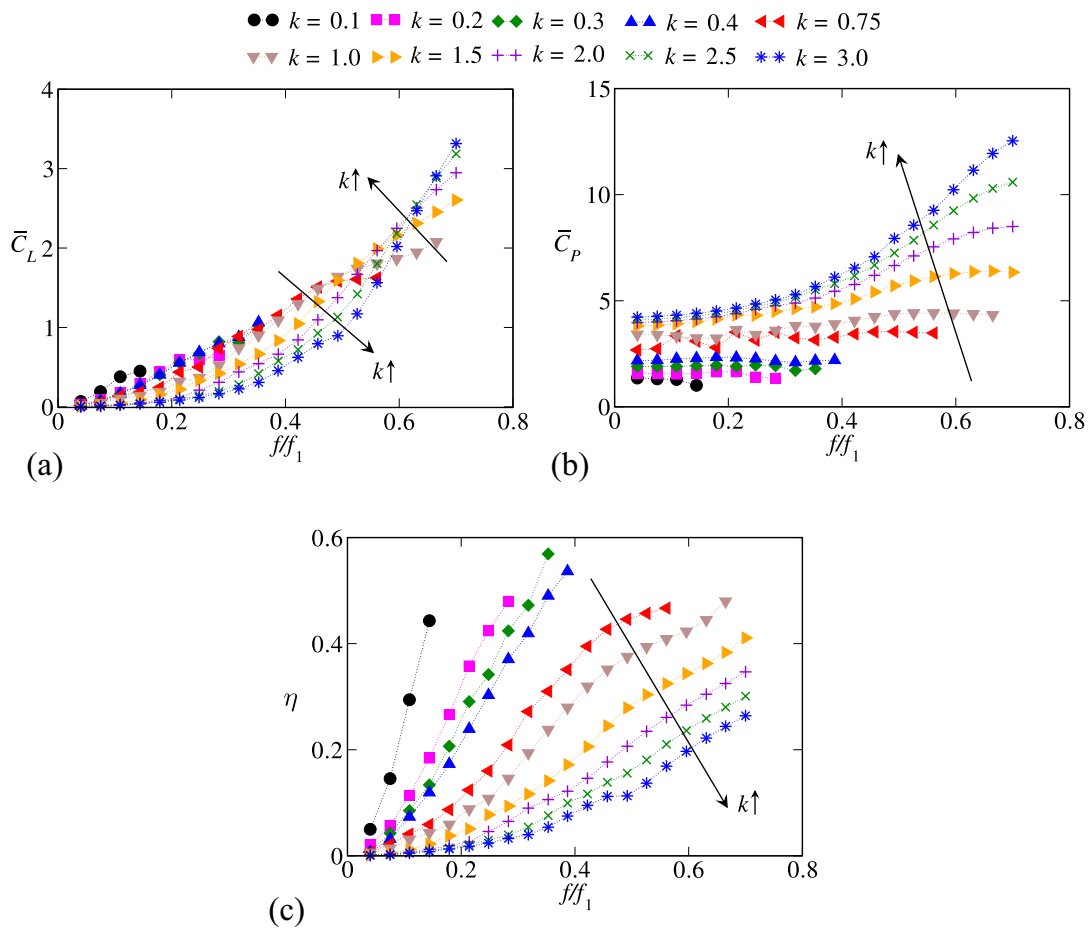


Figure 4-1. Aerodynamic response at fruit fly scale. Variation of (a) time-averaged lift, \bar{C}_L , (b) time-averaged power input, C_P and (c) efficiency, η . Trend line shows the direction along which reduced frequency, k increases [38]. Refer Table B-1 for individual values.

The time-averaged lift coefficient \bar{C}_L is an important performance metric for hovering flight as a flier needs to generate sufficient lift to sustain its weight. Figure 4-1(a) shows that the flexible wing can generate a \bar{C}_L between 0 and 3.3 for the considered parameters. For a fixed value of reduced frequency k , as frequency ratio f/f_1 increases, an increase in lift \bar{C}_L is observed. At small f/f_1 , the wing is almost rigid and flaps vertically. Therefore hardly any lift is produced at smaller f/f_1 . As f/f_1 increases, wing deformations increase, which are reported in Section 4.2.2. As discussed by Kang and Shyy [63] the passive pitch acts as an effective angle of attack and directly affects the lift. Larger wing deformations correlate to higher passive pitch angles, and, hence, higher angles of attack and lift. For $k \leq 1$, the increase in \bar{C}_L is faster than for $k > 1$. Both the location of the maximum lift and the frequency ratio at which lift becomes maximum increase with k . Highest lift among the considered cases is 3.3, obtained for case with $k = 3.0$ and $f/f_1 = 0.7$.

Figure 4-1(b) shows the time-averaged power input, \bar{C}_P as a function of the frequency ratio f/f_1 and reduced frequency k for the same data points as for \bar{C}_L . Time-averaged power input varies considerably between 1.0 and 12.5. Magnitude of \bar{C}_P increases with increase in k and f/f_1 , similar to \bar{C}_L . However, the variation of \bar{C}_P is almost zero for $f/f_1 \geq 0.3$, indicating that \bar{C}_P correlates stronger to k than to f/f_1 . In fact, for the cases considered, none of the curves that connect \bar{C}_P at constant k intersected each other except at one point ($k = 0.75$; $f/f_1 = 0.1$) for an almost rigid wing case. Consequently, increasing k at fixed f/f_1 always introduced higher \bar{C}_P . For $f/f_1 > 0.3$, \bar{C}_P increases substantially and this increase is more pronounced for higher k .

The propulsive efficiency, which is the ratio of \bar{C}_L and \bar{C}_P is illustrated in Figure 4-1(c). Because the increase of \bar{C}_P with k is more pronounced than for \bar{C}_L , the propulsive

efficiency increases steeper for lower k . While $k = 3.0$, $f/f_1 = 0.7$ produces the highest lift of $\bar{C}_L = 3.3$, \bar{C}_P was $\bar{C}_P = 12.5$ resulting in a propulsive efficiency of $\eta = 0.26$. On the other hand, when $k = 0.3$ and $f/f_1 = 0.35$, produces a moderate value $\bar{C}_L = 1.0$. However, \bar{C}_P has a relatively lower value of 1.8. As a result, the efficiency value $\eta = 0.6$ is the highest among the considered cases. Therefore, the wing structures and kinematics that corresponds to the highest lift does not result in the optimal efficiency mode.

4.1.2 Structural response at fruit fly scale

Figure 4-2 shows the structural response of a flexible wing in hover at the fruit fly scale. The passive pitch at the middle α_m and at the end of the stroke α_e are shown for the same values of k and f/f_1 reported in Section 4.2.1. A rigid wing produces a constant angle of attack of 90 degrees, corresponding to a vertical orientation. Wing deformations and passive pitch changes the mid-stroke angle of attack to $\alpha_m < 90$ degrees and the end-stroke angle of attack $\alpha_e > 90$ degrees.

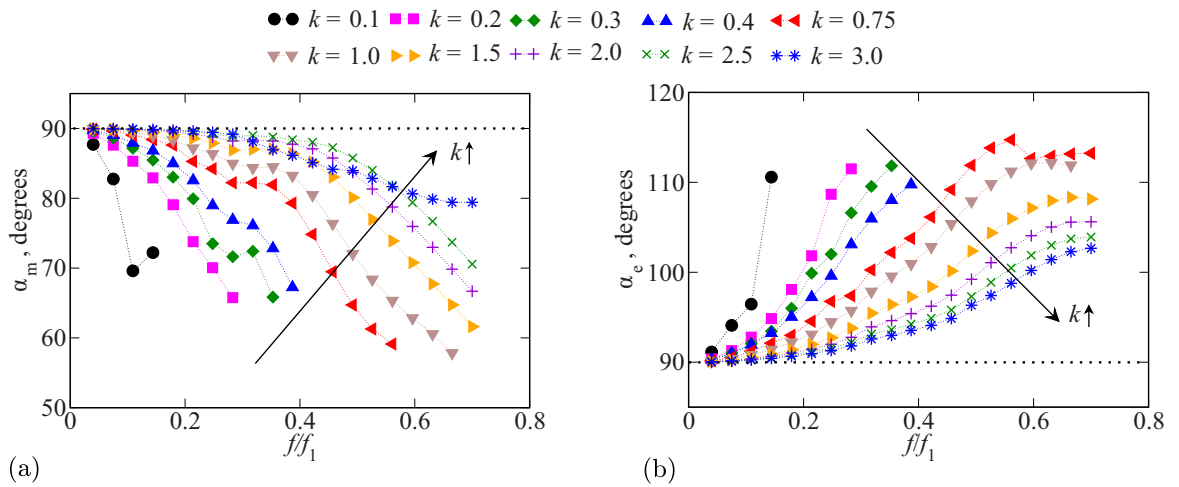


Figure 4-2. Structural response at fruit fly scale. (a) mid-stroke angle, α_m and (b) end-stroke angle, α_e . Refer Figure 3-1(b) for a pictorial representation of the angles [38]. Refer Table B-2 for individual values.

Figure 4-2 shows that, in general, larger wing deformations are obtained for lower reduced frequencies k and higher frequency ratios f/f_1 . This behavior can be explained with the help of the shape deformation factor γ [63,64] which relates wing deformation at TE relative to the LE as shown in equation 2-6.

For hovering motion, St is constant. Also, because in this study both the density ratio ρ^* and thickness ratio h_s^* are assumed to be constants, γ simplifies to

$$\gamma \sim \frac{1}{k \left\{ (f_1 / f)^2 - 1 \right\}}, \quad (4-1)$$

which shows that γ is inversely proportional to k . This is also confirmed by discussion in Chapter 5. Moreover, increasing frequency ratio f/f_1 results in a higher γ , consistent with the current results. Also, design space in Figure 3-1(c) shows that the iso-lines of the frequency ratios are clustered in the lower bottom-left region. For lower values of k , e.g. $k = 0.2$, a slight decrease of Π_1 of the wing, which is proportional to the Young's modulus, substantially increase the frequency ratio f/f_1 .

At fruit fly scale, it is observed that the end-stroke angle is $\alpha_e > 90$ degrees for all cases as shown in Figure 4-2(b). When $\alpha_e > 90$ degrees, the wing orientation is such that the passive pitch rotation advances the imposed plunge motion. Such an advanced mode suggests that the phase lag is $\varphi > 90$ degrees, which will be discussed in Section 5.1. Similarly, the passive pitch angle at the start of the stroke was always less than 90 degrees.

4.2 Aeroelastic response at bumblebee scale

4.2.1 Aerodynamic performance at bumblebee scale

The aerodynamic performance, i.e. time-averaged lift coefficient, \bar{C}_L , time-averaged power \bar{C}_P , and propulsive efficiency η at bumblebee scale is shown in Figure 4-3 as a function of frequency ratio f/f_1 for $0.1 < k < 3.0$.

The time-averaged lift coefficient increases with increase in f/f_1 at a fixed k (see Figure 4-3(a)). The dependence of \bar{C}_L on k at fixed f/f_1 is more complex. At lower f/f_1 , the time-averaged lift coefficient \bar{C}_L increases with decreasing k . In particular, the lift is notably higher when $k = 0.1$ and f/f_1 is between 0.04 and 0.3. For higher f/f_1 , the trend in k is not monotonic. For $k > 2.0$, lift slowly increases up to $f/f_1 = 0.4$ beyond which lift increases steeply. However, the highest \bar{C}_L values are obtained for $k = 0.75$ and 1.0. The highest lift of 1.43 is obtained in the design space for $k = 1.0$ and $f/f_1 = 0.7$.

Time-averaged power in the design space varies between 0.8 and 6.2 (see Figure 4-3(b)). At $k = 0.1$ and $k = 0.2$, \bar{C}_P slightly decreases as f/f_1 increases. A similar decreasing trend was found as a function of f/f_1 at $Re = 150$ and $\rho^* h_s^* = 1$ for $k = 0.4$ by Yin and Luo [34]. At $k = 0.3$ and $k = 0.4$, the reduction in power input flattens with an increase in f/f_1 . For higher k , \bar{C}_P increases with f/f_1 . The maximum time-averaged power of $\bar{C}_P = 6.2$ is obtained when $k = 3.0$ and $f/f_1 = 0.7$.

Propulsive efficiency η , which is defined as the ratio between \bar{C}_L and \bar{C}_P , is shown in Figure 4-3(c). Despite the complex trends in \bar{C}_L and \bar{C}_P , efficiency monotonically increases with f/f_1 and decreases with k . The optimal efficiency of $\eta = 0.95$ is achieved at $k = 0.1$ and $f/f_1 = 0.7$. The motion with the highest lift of 1.43 ($k = 1.0$; $f/f_1 = 0.7$) corresponds

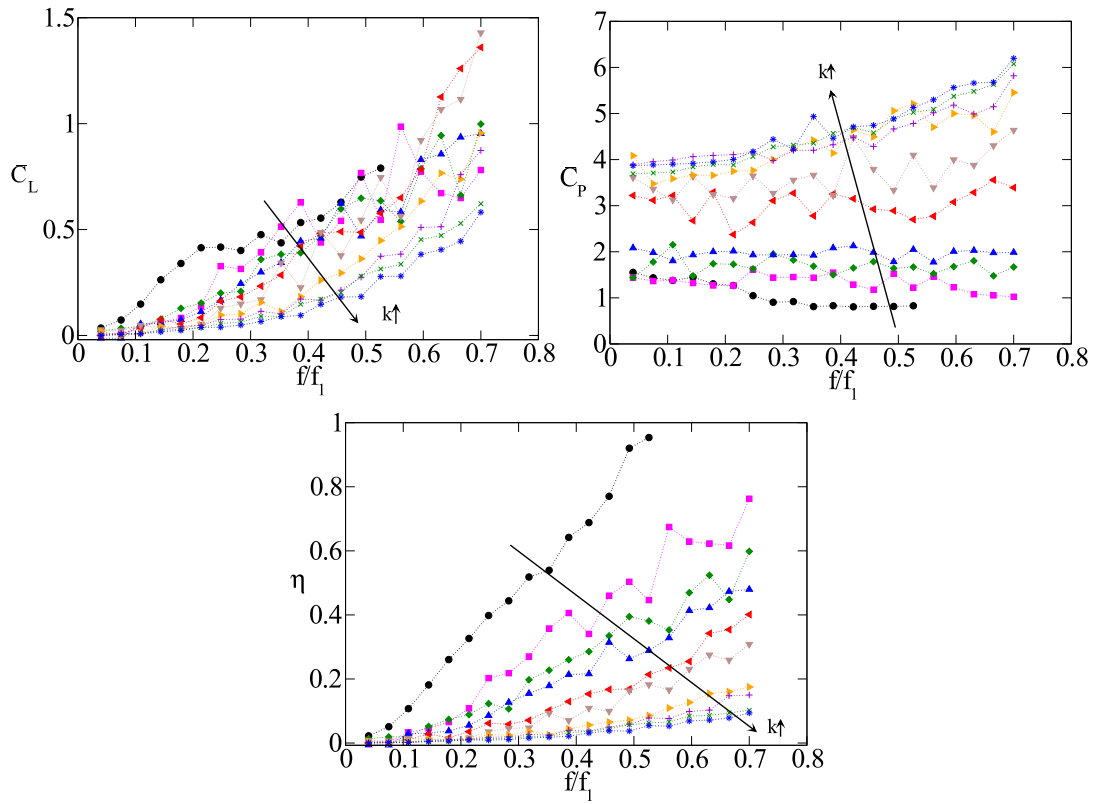


Figure 4-3. Aerodynamic performance at bumblebee scale. (a) Variation of time-averaged lift coefficient \bar{C}_L , (b) time-averaged power input \bar{C}_P , and (c) propulsive efficiency η as a function of frequency ratio f/f_1 and reduced frequency k . Direction of increase of reduced frequency k is indicated by the black arrow [40]. Refer to Figure 4-1 for the legend. Refer Table B-3 for individual values.

to a moderate efficiency of $\eta = 0.3$. The highest f/f_1 at a lowest reduced frequency of $k = 0.1$ results in both relatively high \bar{C}_L and the lowest \bar{C}_P , resulting in the highest efficiency motions. On the other hand, at $k = 3.0$, where the wing moves back and forth in the shortest amplitude (based on $h_a/c = 2/k$), the efficiency remains the lowest due to the highest power requirement.

4.2.2 Structural response at bumblebee scale

Figure 4-4 illustrates the structural response of a flexible wing in hover at the bumblebee scale. The qualitative behavior is similar to that at the fruit fly scale as seen in Figure 4-2. The passive pitch at the middle of the stroke α_m and at the end of the stroke α_e are shown for the same values of k and f/f_1 as in Figure 4-4. A rigid wing produces a constant angle of attack of 90 degrees, corresponding to a vertical orientation. Wing deformations and passive pitch changes the mid-stroke angle of attack to $\alpha_m < 90$ degrees as seen in Figure 4-4(a) and the end-stroke angle of attack to $\alpha_e > 90$ degrees.

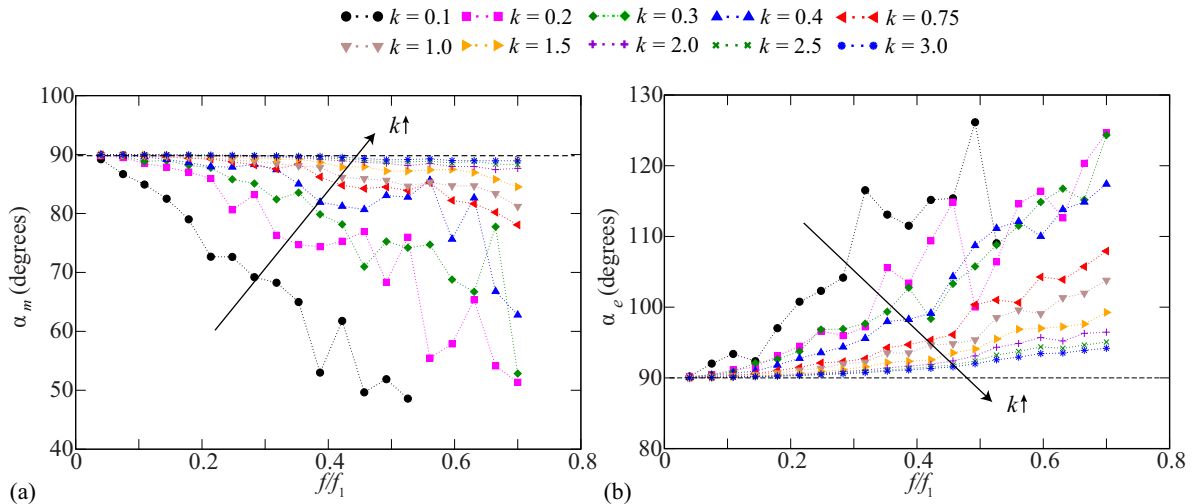


Figure 4-4. Structural response at bumblebee scale. (a) Variation of midstroke angle α_m and (b) endstroke angle α_e as a function of frequency ratio f/f_1 and reduced frequency k . Direction of increase of reduced frequency k is indicated by the black arrow [40]. Refer Table B-4 for individual values.

In general, larger wing deformations are obtained for lower reduced frequencies k and higher frequency ratios f/f_1 (see Figure 4-4) at bumblebee scale. This behavior can be explained with the help of the shape deformation factor γ [63,64], which relates wing

deformation at TE relative to the LE as equation (2-6). For hovering motion, St is constant. Also, because in this study both the density ratio ρ^* and thickness ratio h_s^* are assumed to be constants, γ simplifies to equation (4-1) which shows that the wing deformation, measured by γ is inversely proportional to k , consistent with discussion in Chapter 5. Moreover, increasing frequency ratio f/f_1 results in a higher γ , and larger deformations. When the relative deformations reach an angle around 50 degrees, which is far beyond the validity of the employed linear Euler-Bernoulli beam model, equation (3-3), the coupled FSI fails to converge. Only fully converged results are reported in this study.

The end-stroke angle is $\alpha_e > 90$ degrees for all motions as shown in Figure 4-4(b). When $\alpha_e > 90$ degrees, the wing orientation is such that the passive pitch rotation advances the imposed plunge motion. Such an advanced rotational mode suggests that the phase lag is $\varphi > 90$ degrees. This will be discussed in Section 5.1.

4.2.3 Non-periodic aeroelastic response

Figure 4-5 shows time history of C_L and C_D up to thirty cycles at bumblebee scale. The non-periodic response is evident. Both aerodynamic performance in Figure 4-3 as well as structural response in Figure 4-4 at exhibit noticeable fluctuations in f/f_1 . For example, when $k = 1.0$, the change in lift coefficient as shown in Figure 4-3(a) is around 28% between $f/f_1 = 0.67$ and $f/f_1 = 0.7$. Also, the midstroke angle of attack in Figure 4-4(a) oscillates for $k = 0.2$ for $f/f_1 > 0.4$.

The fluctuations in \bar{C}_L are much weaker for $k > 1.5$. For $k > 1.5$, \bar{C}_P increases with f/f_1 without significant oscillations. Additionally, for $k > 1.5$, the responses are clustered

together. In order to illustrate the cause of these fluctuations, three frequency ratios at $k = 1.0$: $f/f_1 = ($ st lift.

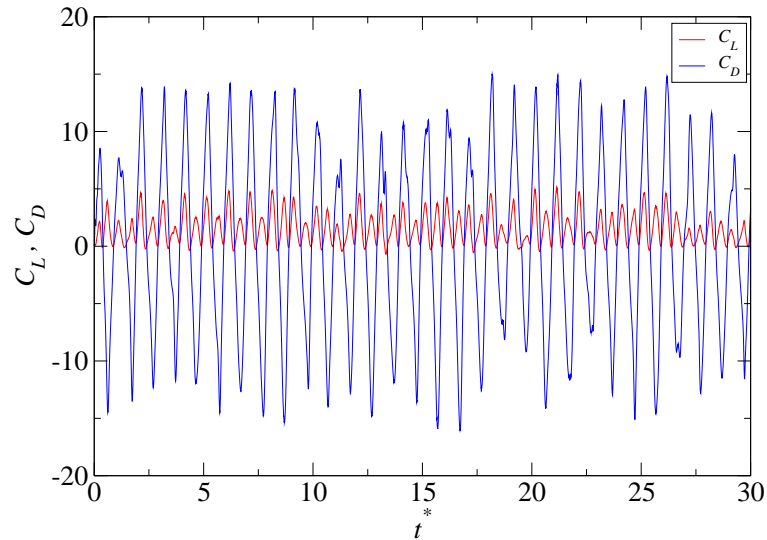


Figure 4-5. Time history of C_L and C_D over thirty cycles at bumblebee scale with $k=1.0$, $f/f_1=0.7$. C_D is symmetric about zero line where as C_L average is a positive quantity.

The highest lift motion ($k = 1.0$; $f/f_1 = 0.70$) will be explored more in detail in Section 5.2. Figure 4-6(a) and (b) show the time histories of lift C_L at highest lift and optimal motions respectively. The corresponding passive pitch angle α for $6 < t^* < 10$, i.e. over four motion cycles, is shown in Figure 4-9(a) and (b). For all three frequency ratios, the resulting time histories are not periodic in time. For example, for the highest lift motion in Figure 4-6(a) at $f/f_1 = 0.70$, the lift coefficient at the middle of the forward stroke in the seventh cycle ($t^* = 7.75$) is $\bar{C}_L = 2.08$, which jumps up $\bar{C}_L = 3.0$ in the next motion cycle at $t^* = 8.75$. As a result, the time-averaged lift and drag coefficient strongly depend on which cycles are used for averaging as shown in Figure 4-8. In Figure 4-8(a) and (b), the resulting time-averaged force coefficients are plotted against the period of cycles that are used in the averaging for highest lift and optimal efficiency motion respectively. At highest lift motion, when the first five cycles are taken for time-

averaging, the resulting time-averaged lift coefficient is $\bar{C}_L = 1.14$. If the next five cycles are used, i.e. from the fifth to tenth cycles, the time-averaged lift coefficient increases to $\bar{C}_L = 1.43$. Moreover, the time-averaged values change if ten cycles are used for time-averaging, rather than five as before. At optimal efficiency motion as shown in Figure 4-8(b), the magnitudes of averaged lift and drag coefficients also vary depend on which cycles were chosen for averaging.

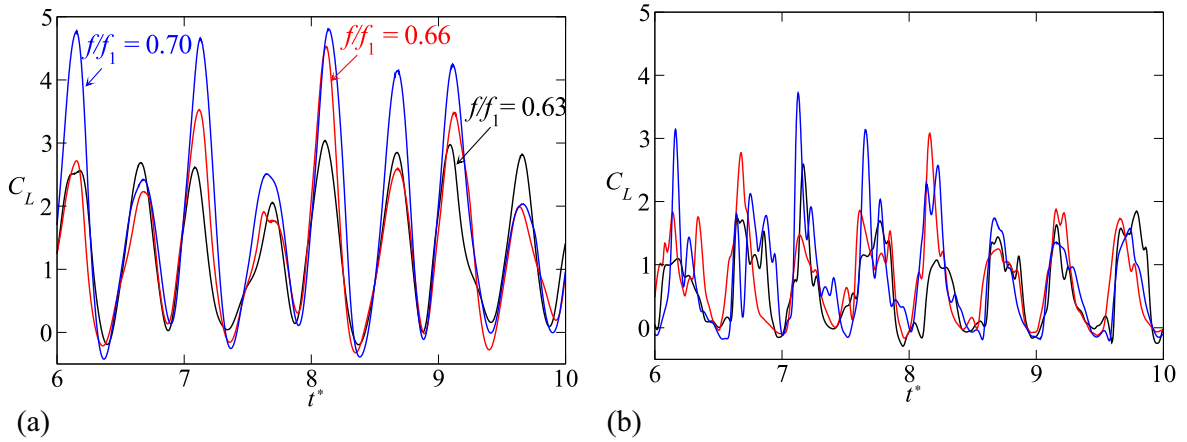


Figure 4-6. Non-periodic lift history at bumblebee scale for (a) highest lift motion (b) optimal efficiency motion. Lift history at three different frequency ratios are shown [40].

Furthermore, to verify the effects of number of points along the frequency ratio axis, the resolution is doubled from twenty to forty as shown in Figure 4-7. The averaging is performed over four cycles consistent with fruit fly scale. With twenty points between $0.04 < f/f_1 < 0.7$ (red dots), there are noticeable fluctuations in the time averaged lift coefficient. The oscillations are much stronger in case of the drag coefficient. Doubling the number of points (black dots) does not smoothen the oscillations. In fact, as seen in Figure 4-7, the oscillations are present even with the finer resolution of the horizontal axis.

The observed fluctuations may be related to the qualitative character of the resulting vortex dynamics at the considered $Re = 1.0 \times 10^3$. At the Reynolds number relevant to a hovering hawkmoth, $Re = 4.0 \times 10^3$ to 6.0×10^3 , an intense and conical LEV was observed on the wing [76]. On the other hand, at a lower Reynolds number, corresponding to a hovering fruit fly at $Re = 120$, such vortex structures were simpler

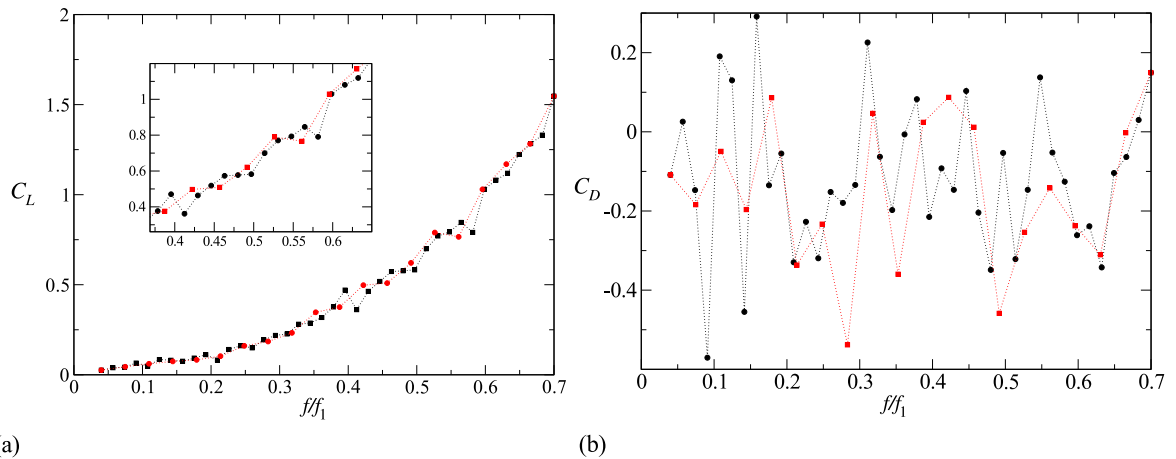


Figure 4-7. Effects of doubling the number of points on the (a) time averaged lift (b) time averaged drag at bumblebee scale. Increasing the number of points does not smoothen the lift and drag curves.

[76,77]. Moreover, a dynamically scaled wing experiment [77] showed that the net force coefficients were slightly higher at $Re = 1400$ than at $Re = 120$, corresponding to comparatively greater vorticity production with more complex structure in the flow. Slightly higher force production and more chaotic vortical evolution were observed for a flexible wing at $Re = 1.0 \times 10^3$ compared to $Re = 1.0 \times 10^2$ [38]. The complex vortical structures, which will be discussed in Section 5.2.2, and their nonlinear interactions with hovering wings leads to a non-periodic aeroelastic response of the flexible wing at the bumblebee scale.

As a result of these wing-wake interactions, the time-averaged quantities fluctuate significantly for these motions at the bumblebee scale, compared to those at the fruit fly scale. Moreover, Figure A-1(a-c) in the Appendix A, illustrates that the number of cycles taken in the time-averaging also affects the trend in f/f_1 . The time-averaged lift coefficient is calculated for the optimal efficiency motion over 10, 4, and 2 cycles. The trend of \bar{C}_L is indicated by the black solid curve. The grey regions around the black curve are bounded by the maximum and minimum lift coefficients encountered in the considered 10, 4, and 2 cycles. Figure A-1(a) clearly shows that the fluctuating trend in \bar{C}_L smoothens out when averaged over 10 cycles, whereas the oscillations significant for the averaging occur over 2 cycles. The magnitude of oscillations present at the bounds of data directly influences the averaged profile.

In this study, the time-averaging is consistently performed over 4 cycles for a consistent comparison to the fruit fly scale which also involves time-averaging over the same 4 cycles. The trends at the fruit fly scales are significantly smoother, which is most likely due to the nearly periodic aeroelastic response and the simpler vortical structures as discussed in Section 5.1.

4.2.4 Normalization of lift coefficient

The considered flexible wings undergo significant deformation during hovering motion. Since a linear Euler-Bernoulli beam is used to model the wing, the wing length is not conserved within a flapping wing stroke. When the wing deformation is substantial, such as around the midstroke where the plunge velocity is the maximum, the instantaneous wing length increases relative to the original chord.

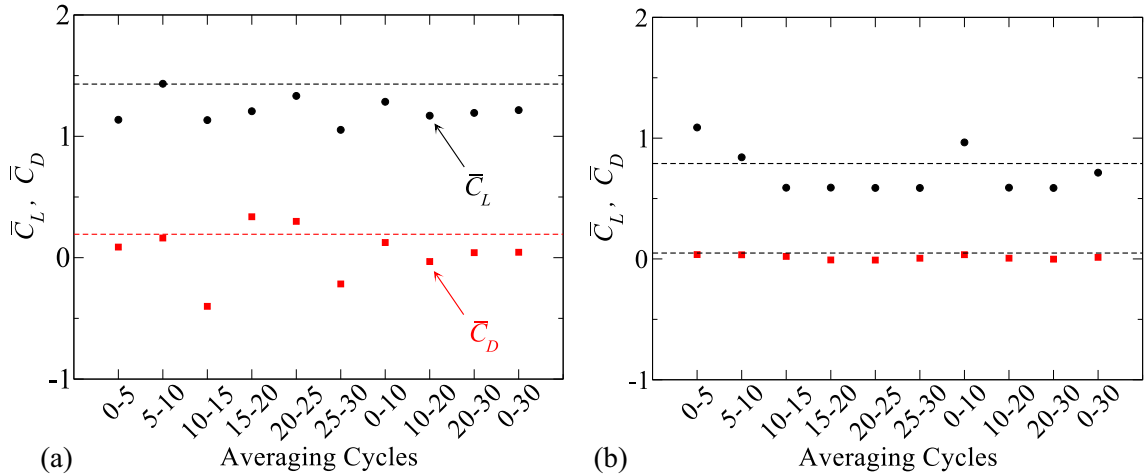


Figure 4-8. Time averaged C_L and C_D at various averaging cycles at bumblebee scale. (a) highest lift motion (b) optimal efficiency motion. Dotted horizontal line represents the averaged value considered in the current study which corresponds to 6-10 cycles.

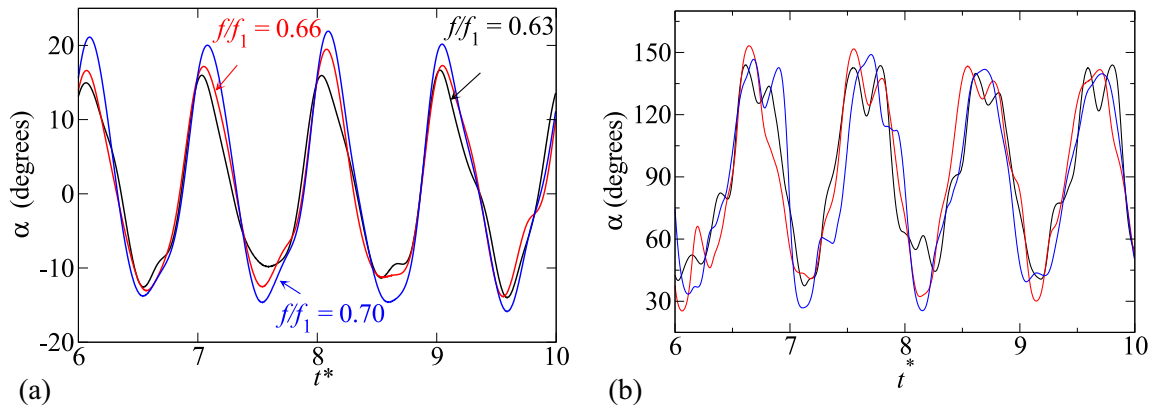


Figure 4-9. Non-periodic evolution of passive pitch angle α for (a) highest lift motion (b) optimal efficiency motion at bumblebee scale. Response at three frequency ratios are shown.

In order to assess the effects of the time varying chord on the lift coefficient, the normalized lift coefficient is introduced as the lift coefficient normalized by the instantaneous chord length. This is a more accurate representation of the instantaneous lift coefficient since it takes into account the instantaneous wing configuration. Figures 4-10(a) and (b) shows the lift and drag coefficient at bumblebee scale calculated by averaging over four motion cycles at $k = 1.0$, $ff_1 = 0.70$. The time averaged lift without normalization shown in black is plotted along with the normalized lift in Figure 4-10(a).

The difference between the two is not significant. The effect of normalization is only slightly noticeable at $f/f_1 > 0.5$. This is because as f/f_1 increases, the wing flexibility also increases. But even at highest f/f_1 , the percentage change in lift coefficient with and without normalization is as low as 5%. Similar argument holds good for time averaged drag coefficient as well, justifying the use of equation (3-3) throughout the thesis.

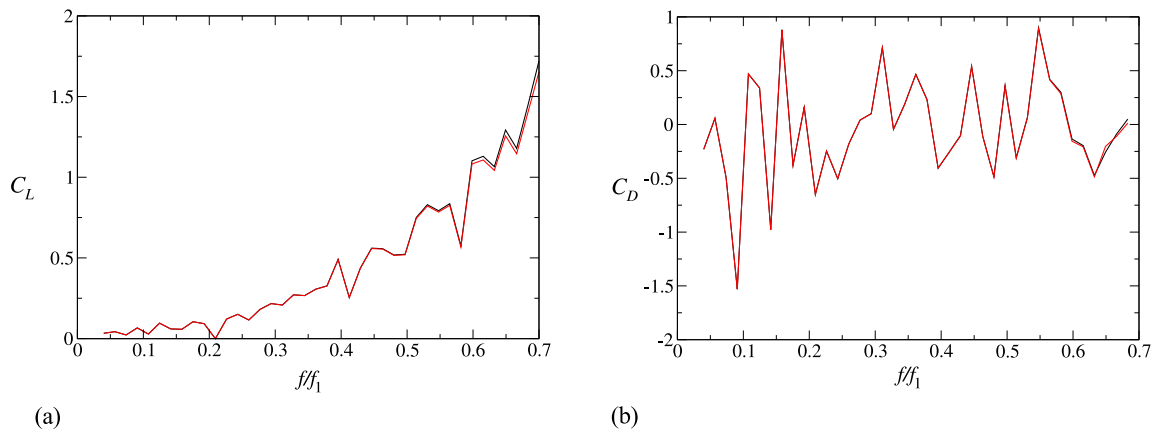


Figure 4-10. Effect of normalization with instantaneous chord length at bumblebee scale. (a) time averaged lift and (b) time averaged drag coefficient. Normalized lift coefficient is shown in red.

CHAPTER 5

DISCUSSION

In this chapter, a comparison of aeroelastic response at fruit fly and bumblebee scales is presented including a detailed analysis of selective optimal points in the design space. Scaling of lift coefficient at fruit fly and bumblebee scales is reported in section 5.4. Finally, current results are compared with experimental measurements from actual insects in Section 5.5 to provide a qualitative insight on the implications of the current results to the insect flight.

5.1 Comparison of aeroelastic response at fruit fly, bumblebee and water tunnel scales

To explore the scaling effects on the fluid-structure interaction of hovering wings, a comparison of the results at the bumblebee scale ($\rho^* = 2.0 \times 10^3$, $h_s^* = 1.0 \times 10^{-3}$, $Re = 1.0 \times 10^3$) with the aerodynamic performance at the fruit fly scale ($\rho^* = 1.0 \times 10^3$; $h_s^* = 1.5 \times 10^{-3}$; $Re = 1.0 \times 10^2$) and water tunnel scale: ($\rho^* = 7.8$; $h_s^* = 2.0 \times 10^{-2}$; $Re = 1.0 \times 10^2$) [63] was made.

Contours of \bar{C}_L , \bar{C}_P , and η at the bumblebee scale is shown in Figure 5-1, together with the contour at the fruit fly scale and water tunnel scale. The contours are generated with k along vertical axis and effective stiffness ratio Π_1 along horizontal axis. The effective stiffness is inversely proportional to $f/f_1 \sim k/\Pi_1^{1/2}$, which is also evident from the design space as shown in Figure 3-1(c).

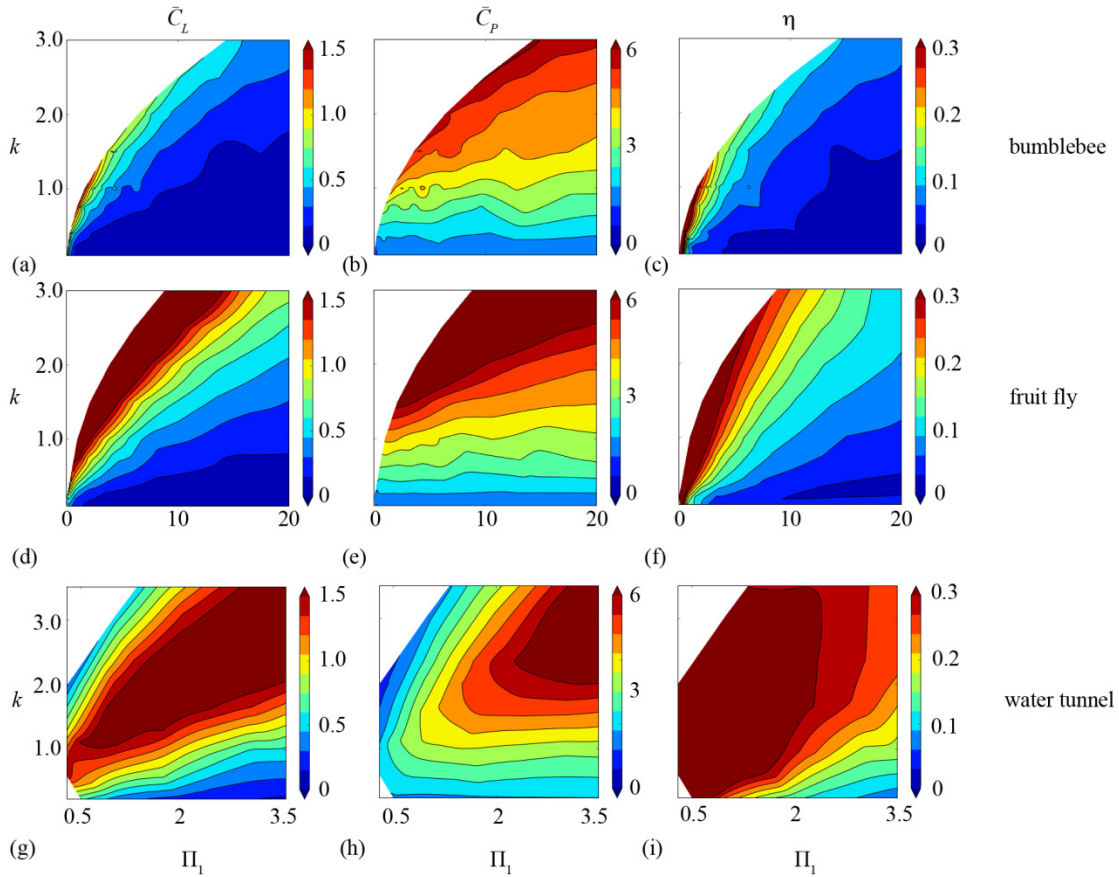


Figure 5-1. Aerodynamic contours at fruit fly [38], bumblebee [40] and water tunnel scales [63]. Contours of (a,d,g) time averaged, \bar{C}_L (b,e,h,) time averaged power input, \bar{C}_P (c,f,i) efficiency η for bumblebee scale (top row), fruit fly scale (middle row) and water tunnel [63] (bottom row) in the design space of effective stiffness Π_1 and reduced frequency k . Refer Tables B1 and B3 in Appendix B for individual values at fruit fly and bumblebee scales, respectively.

Compared to the fruit fly scale at $Re = 1.0 \times 10^2$, \bar{C}_L at the bumblebee scale at $Re = 1.0 \times 10^3$ is slightly lower in magnitude, which may contradict other studies in the

literature [77,78] that the force magnitude increased slightly with the Reynolds number. However, both density ratio ρ^* and thickness ratio h_s^* are different as well. As a result, the structural dynamics responds differently with slightly smaller passive pitch angles at bumblebee scale and the combined effect is that \bar{C}_L is lower.

The qualitative trend observed in Section 4.2.1 is also reflected in the design space. Maximum \bar{C}_L is concentrated near the lower k and lower Π_1 region, indicating higher f/f_1 . The location of maximum \bar{C}_L is qualitatively different than at the fruit fly scale. At the fruit fly scale, the maximum lift is obtained for the highest reduced frequency and frequency ratio (see Figure 4-1(a)). At water tunnel scale [63], location of maximum \bar{C}_L is at much lower f/f_1 ($f/f_1 = 0.34$, $k = 2.0$). Parameters corresponding to highest lift in the design space at all three scales are presented in Table 5-1.

Table 5-1. Performance metric at the highest lift and optimal efficiency motions for the bumblebee, fruit fly and water tunnel [63] scales.

	Scale	k	f/f_1	\bar{C}_L	\bar{C}_P	η
Highest lift	Fruit fly	3.0	0.70	3.30	12.70	0.27
	Water tunnel	2.0	0.34	1.78	5.19	0.34
	Bumblebee	1.0	0.70	1.43	4.63	0.30
Optimal efficiency	Fruit fly	0.3	0.35	1.00	1.80	0.60
	Water tunnel	0.6	0.24	1.45	2.18	0.66
	Bumblebee	0.1	0.53	0.79	0.82	0.95

On the other hand, both time-averaged power input \bar{C}_P and propulsive efficiency η are similar between fruit fly and bumblebee scales. The power consumed is similar in qualitative trend, although the magnitude is lower for the bumblebee scale at higher k and

f/f_1 , i.e. lower Π_1 . The efficiency, as a consequence, is higher in the lower left region of the design space, albeit the region of higher efficiency is confined to a small region. The performance metrics at the highest lift and optimal efficiency motions at the three scales including the water tunnel scale [63] ($\rho^* = 7.8$; $h_s^* = 2.0 \times 10^{-2}$; $Re = 1.0 \times 10^2$) are summarized in Table 5-1. As discussed earlier, the lift coefficient for the highest lift and optimal efficiency motions are lower for the bumblebee scale. However, the overall highest efficiency is obtained for the bumblebee scale.

Similar to the midstroke angle α_m , the angular amplitude α_a obtained from equation (3-4) at bumblebee scale decreases with k and increases with f/f_1 and varies between 0.01 degrees and 52.5 degrees as shown in Figure 5-2. Compared to the fruit fly scale, the resulting wing deformations are smaller, which is consistent with the observed lift coefficients with lower magnitudes. At fruit fly scale, the angular amplitude α_a increases with k and f/f_1 and varied between 58 degrees and 90 degrees, whereas the phase lag φ varies between 90 degrees and 101 degrees. Figure 5-2 shows that as k increases, the rate of increase of α_a decreases with f/f_1 . For the lowest reduced frequency $k = 0.1$, α_a of 27 degrees is reached at a frequency ratio of $f/f_1 = 0.14$. However, for $k = 1$, the same α_a is achieved at $f/f_1 \approx 0.51$. The phase lag φ at bumblebee scale follows the trend observed for the endstroke angle α_e (see Figure 4-4(b)). The resulting rotational modes are advanced for all considered motions, which is also seen at the fruit fly scale. On the other hand, water tunnel scale [63] exhibited all three rotational modes [13]: advanced, symmetric, and delayed.

These rotational modes also scaled with f/f_1 [13]. As discussed earlier [38], the resulting advanced rotational mode may be due to the lack of the aerodynamic damping

force to counteract the wing rotation due to inertial force at the stroke ends. The ratio between the inertial force and aerodynamic forces scales with the mass ratio $\rho^* h_s^*$ [79]. For the bumblebee and fruit fly scales, $\rho^* h_s^* = 2$ and $\rho^* h_s^* = 1$, respectively, which is significantly higher than at the water tunnel scale, $\rho^* h_s^* = 0.156$.

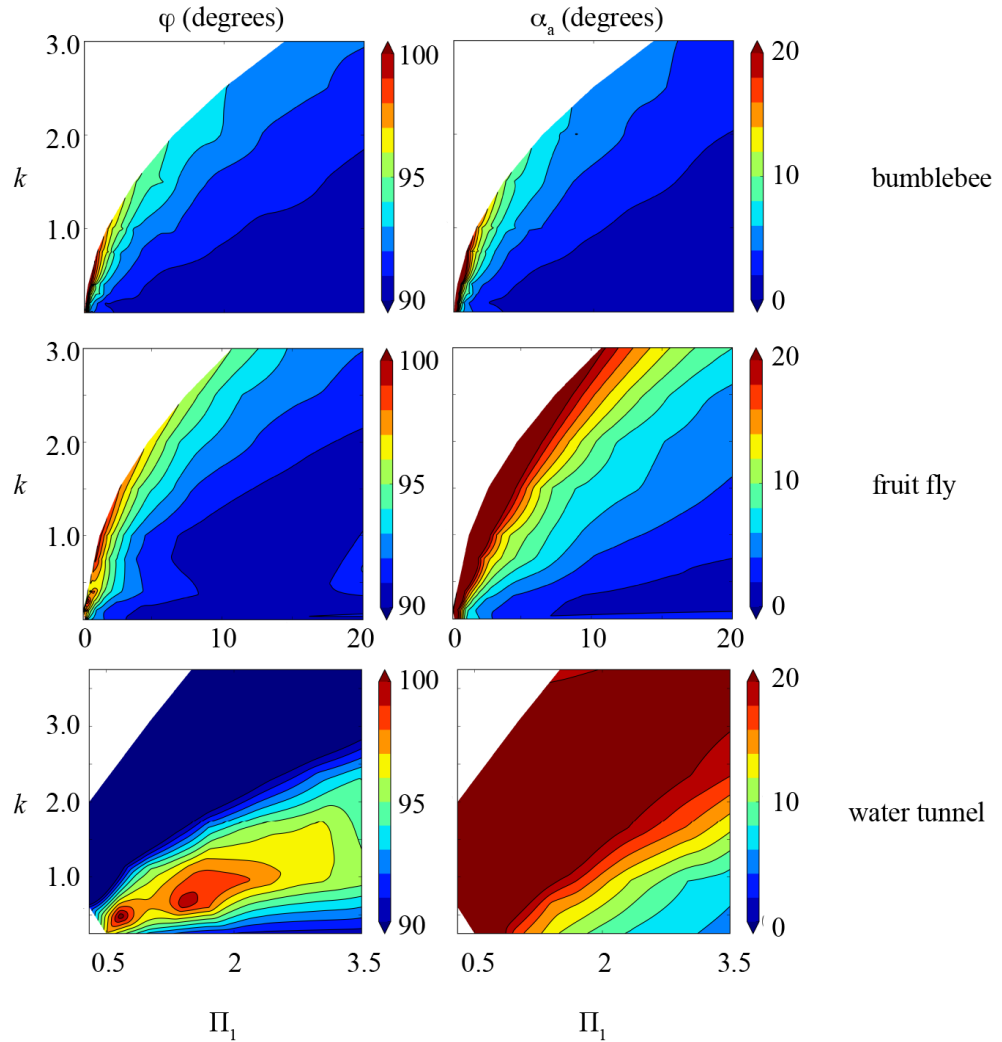


Figure 5-2. Structural response contours at fruit fly [38], bumblebee [40] and water tunnel scales [63]. Contours of (left) phase lag φ and (right) passive pitch amplitude α_a for bumblebee (top row), fruit fly (middle row) and water tunnel (bottom row) scales in the design space of effectiveness Π_1 and reduced frequency k . Refer Tables B2 and B4 in Appendix B for individual values at fruit fly and bumblebee scales, respectively.

5.2 Highest lift motion

To explore the interaction between the flexible wing and the surrounding fluid, the time history of lift and the wing shapes at fruit fly and bumblebee scales at highest lift motions and corresponding vorticity contours are plotted in Figure 5-3 and Figure 5-4 respectively. Results for the highest lift at the water tunnel scale [63] are also included.

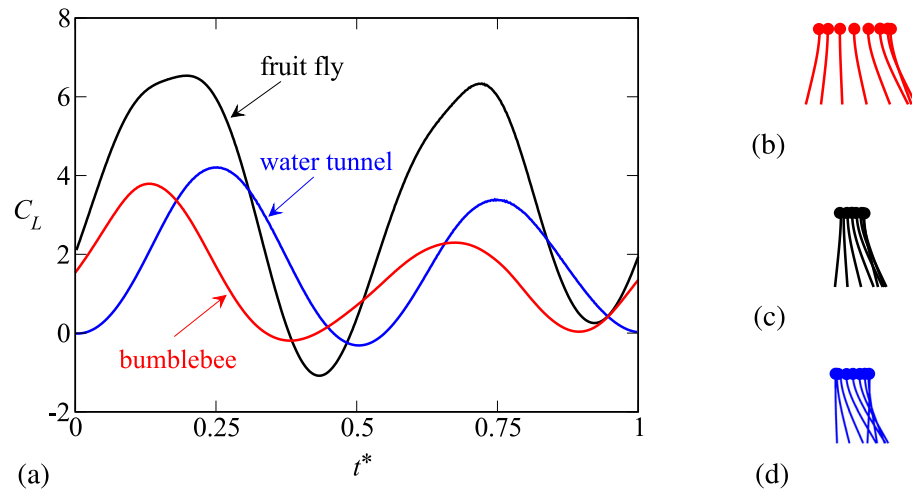


Figure 5-3. Comparison of lift history and wing shapes at highest lift motions at bumblebee [40], fruit fly [38] and water tunnel [63] scales. (a) Time histories of lift for highest lift motions: (-) bumblebee scale (-) fruit fly scale (-) water tunnel scale [63]. Snapshots of wing displacements for (b) bumblebee (c) fruit fly and (d) water tunnel scale.

Vorticity structures at water tunnel, fruit fly and bumblebee and scales are shown as five snapshots in time for highest lift motions during a backstroke in Figure 5-4. The backstroke begins at the right-most image and evolves as it moves to the left in equal time intervals. Moreover, for the bumblebee scale, the vorticity contours in the following forward stroke are also included as the backward stroke is not representative of the forward stroke.

Highest lift at fruit fly scale corresponds to $\bar{C}_L = 3.3$ is achieved at $k = 3.0$ and $f/f_1 = 0.7$. Figure 5-4(b) shows the vorticity contours for the maximum lift case for a backward stroke at the fruit fly scale. Vorticity is non-dimensionalized by U/c . Positive

vorticity corresponds to a counter-clockwise rotation, while negative values represent clockwise rotating fluid elements. The stroke starts at the right at $t^* = 0.0$ and ends at the left at $t^* = 0.5$. Through the stroke, a small-sized, counter-clockwise rotating LEV is seen.

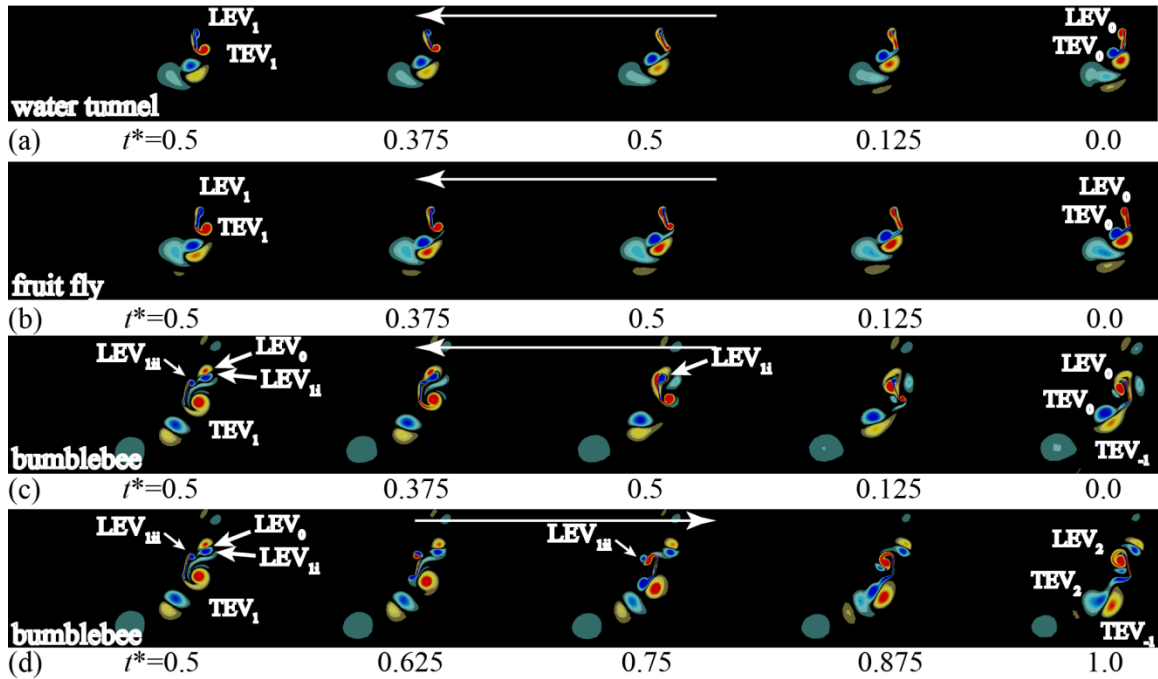


Figure 5-4. Vorticity contours for maximum lift motions [38,40]. (a) water tunnel scale backward stroke (b) fruit fly scale backward stroke (c) bumblebee scale backward stroke (d) bumblebee scale forward stroke.

The subscript in the vorticity contours refer to the current cycle: 1, previous stroke: 0, and two strokes ago: -1. For example, LEV_0 indicates a LEV that is shed in the previous stroke. As the wing moves towards the mid-stroke, the TEV formed during the previous cycle (TEV_0) is shed and is replaced by a counter-clockwise vortex. While a large LEV structure is associated with high lift for aping wings, the highest lift is obtained for a flexible wing motion without a pronounced presence of a LEV. A possible explanation for the high lift is the relatively higher motion frequency corresponding to $k = 3.0$. Higher motion frequency results in a higher added mass force [28,64]. The wing

shapes are clustered together, which is a reflection of a higher k , or a lower plunge amplitude of $2h_a = 1/3 \approx 0.33$.

At bumblebee scale with $k = 1.0$ and $f/f_1 = 0.7$, flow field is more complex than at the fruit fly scale with higher number of vortical structures near the wing. Two LEVs form during the backward stroke: LEV_{1i} and LEV_{1ii} . The subscript 1 corresponds to the current stroke, whereas the subscript 0 refers to the previous stroke. During the beginning of the stroke, a clockwise rotating (blue) leading edge vortex LEV_{1i} forms. Around $t^* = 0.125$, the counterclockwise rotating (red) LEV_0 , formed in the previous stroke, interacts with the wing. Subsequently, LEV_0 interacts with LEV_{1i} . As a result, a pair of vortices, rotating in opposite directions are formed and convects upward. Upward direction is consistent with the upward induced velocity of the vortex pair. In the meantime, a new clockwise LEV_{1ii} is generated at the LE. The vortex pair at the LE is smaller in size when compared to the TEVs, which are more prominent. At the TE, a new vortex TEV_1 is formed and is being convected away in the downward direction along with TEV_0 . The overall vortex structures at bumblebee scale which operates at $Re = 1.0 \times 10^3$ are chaotic in nature as reported in the literature [80]. In the subsequent forward stroke, only one vortex forms at the leading edge, LEV_2 , which will interact with the wing in the next motion cycle.

Similar pattern of a dominant TEV is seen at fruit fly scale as well. Vortex at LE continued to maintain its smaller size throughout the stroke whereas a bigger TEV_1 is seen at the end of the stroke. As opposed to what is observed at bumblebee scale, no pairing of LEV is apparent. Instead, the LEV at fruit fly scale propagated along the wing to the TE where it is shed alternatively. Hence, vortex shedding took place only in downward direction as opposed to both TE and LE as seen in bumblebee scale. Another

significant difference is that at bumblebee scale, the strokes are not symmetric, i.e. the vortical structures at $t^* = 0$ is not similar and a mirror image to $t^* = 0.5$, which is approximately symmetric at the fruit fly scale.

Magnitude of lift at bumblebee scale is almost half of what is achieved at fruit fly scale as shown in Figure 5-3(a). Simulations at bumblebee scale was carried out at a Reynolds number of $Re = 1 \times 10^3$, which is an order of magnitude higher than at fruit fly scale. Higher Reynolds number resulted in chaotic vortical behavior but the resulting lift coefficient was lower in magnitude when compared to fruit fly scale. Earlier work with rigid wings [77,80] and flexible wings [78] showed that increase in Reynolds number resulted in higher lift coefficient. In these studies, Reynolds number alone was varied while keeping the thickness ratio and density ratio the same. This resulted in stronger vortical activity with higher forces.

In current study, all three parameters i.e. Reynolds number, thickness ratio and density ratio are varied between fruit fly and bumblebee scale. The product of density ratio and thickness ratio known as the mass ratio is different between the two scales, see also Table 3-1 for a comparison of parameters. In addition, bumblebee exhibit lower mid stroke angles as shown in Figure 4-4(a) when compared to mid stroke angles at fruit fly scale in Figure 4-2(a). Aerodynamic reasons behind achieving a lower lift magnitude may be due to reversed von Karman vortex shedding in the upper direction as shown enlarged in Figure 5-5.

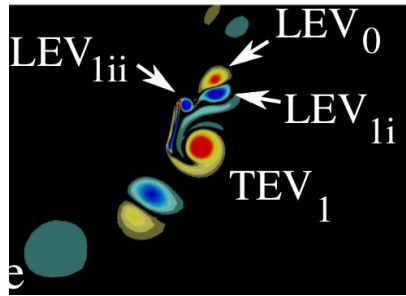


Figure 5-5. Enlarged view of Figure 5-4(c) at $t^* = 0.5$ which shows reversed von Karman vortex shedding at bumblebee scale LEV_0 and LEV_1 which together form a vortex pair is convected in the upward direction.

5.3 Optimal efficiency motion

Figure 5-6 shows the lift history and wing shapes at optimal efficiency motions at fruit fly, bumblebee and water tunnel scales. The lift history at all three scales exhibit dual peak behavior. The backward stroke ($0 \leq t^* \leq 0.5$) results in higher lift coefficient near $t^* = 0.25$ at all three scales. At $t^* = 0.25$, the wing is at its midstroke where the wing deformation, and hence, passive pitch angle, is also the highest (see also Figure 4-2 and Figure 4-4). Vorticity structures at water tunnel, fruit fly and bumblebee and scales are shown as five snapshots in time for optimal efficiency motions during a backstroke in Figure 5-7. The backstroke begins at the right-most image and evolves as it moves to the left in equal time intervals. Moreover, for the bumblebee scale, the vorticity contours in the following forward stroke are also included as the backward stroke is not representative of the forward stroke.

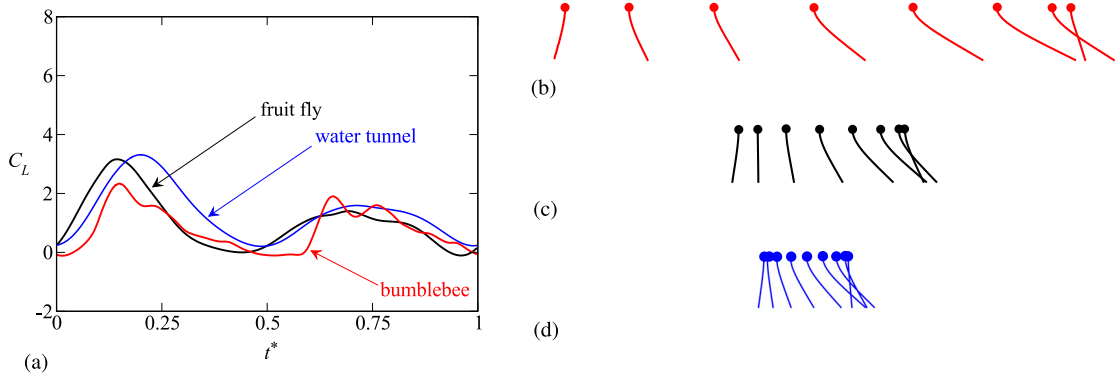


Figure 5-6. Comparison of lift history and wing shapes at optimal efficiency motions at bumblebee [40], fruit fly [38] and water tunnel [63] scales. (a) Time histories of lift for optimal efficiency motions: (-) bumblebee scale (-) fruit fly scale (-) water tunnel scale [63]. Snapshots of wing displacements for (b) bumblebee (c) fruit fly and (d) water tunnel scale.

For bumblebee scale, the lift generation is small at the beginning of the stroke, $0 \leq t^* \leq 0.1$, which corresponds to the first wing-wake interaction with TEV_0 . As soon as the TEV_0 interacts with LEV_{1i} at the suction side of the wing, the lift steeply increases at around $t^* = 0.125$ (see Figure 5-6(a)). This is also partly due to the wing-wake interaction with LEV_{0ii} . The second lift peak may be correlated to the formation of secondary vortex at the leading edge, LEV_{1ii} . Therefore, the presence of multiple wiggles at bumblebee scale may correspond to the dual wing-wake interactions taking place during a cycle as illustrated in the vorticity contours in Figure 5-7(c). For bumblebee scale, the optimal efficiency is achieved at lowest reduced frequency, $k = 0.1$, which corresponds to the largest amplitude $h_a = 5c$. The optimal efficiency for the fruit fly wings was found for $k = 0.3$ or $h_a = 1.67c$. It is quite remarkable to note that the resulting time histories of lift at bumblebee, fruit fly and water tunnel scales for optimal efficiency are similar (see Figure 5-6(a)), despite the differences in k , Re , ρ^* and h_s^* .

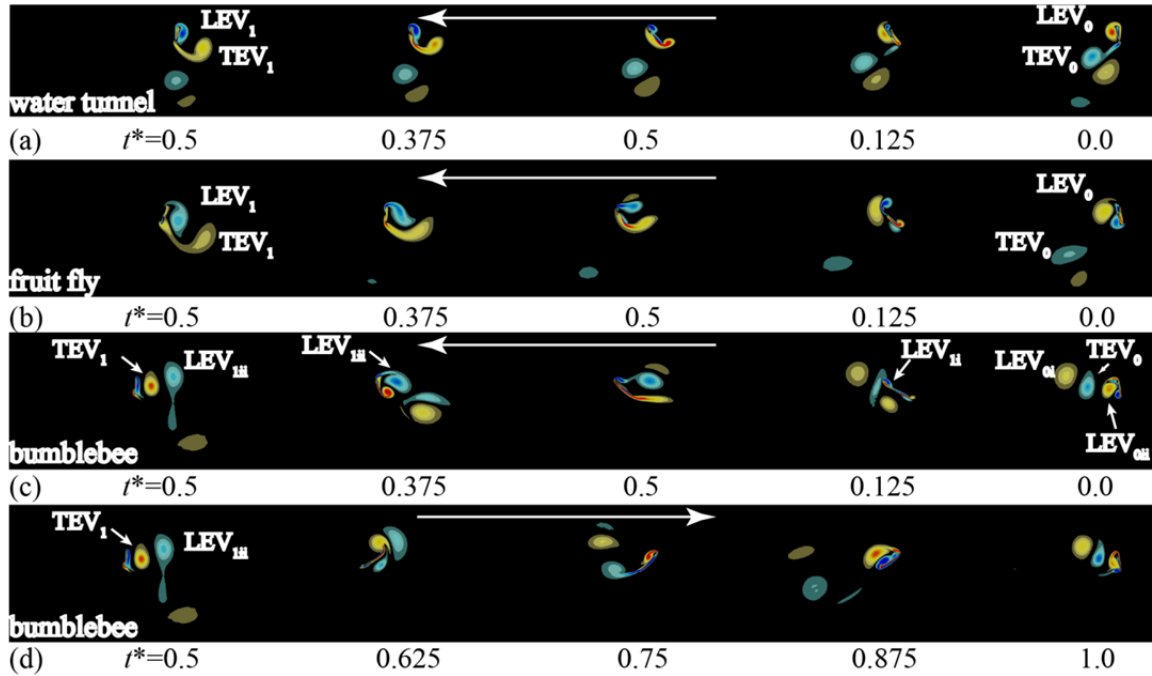


Figure 5-7. Vorticity contours for optimal efficiency motions [38,40]. (a) water tunnel scale backward stroke (b) fruit fly scale backward stroke (c) bumblebee scale backward stroke (d) bumblebee scale forward stroke.

Figure 5-7(b) shows the vorticity contours for the optimal efficiency case with $k = 0.3$ and $f/f_1 = 0.35$ at the fruit fly scale. The corresponding lift, power input, and efficiency were 1.0, 1.8 and 0.6 respectively. For the vorticity, a well-defined vortex LEV_0 at the LE of the flat plate is observed at the beginning of the backward stroke. LEV_0 is generated and shed during the previous cycle. As the wing translates to the middle of the stroke, the wing interacts with LEV_0 . Such wing-wake interaction can have a positive effect on the lift, depending on the wake and wing orientation. Wake-capture can enhance unsteady lift, as discussed numerously in the literature [17,61,63]. A similar vortical evolution was observed at the water tunnel scale (see Figure 5-7(a)), suggesting that the wing interaction with a well-defined LEV may enhance lift without suffering too much on the power consumption. In the meantime, a new LEV_1 in the clockwise

direction is generated, which reaches its maximum intensity at around the mid-stroke and eventually sheds away from the wing. At the TE, a smaller vortex forms at $t^* = 0.0$. The TEV is less pronounced than for the maximum lift case. Moreover, the TEV shed in the previous strokes seem to have diffused away in a much higher rate.

Vorticity contours for optimum efficiency motion at bumblebee scale with $k = 0.1$ and $f/f_1 = 0.53$ shown in Figure 5-7(c) gives rise to LE and TE vortices, which when shed are comparable in size. At $t^* = 0$, LEV_{0ii} , shed in the previous stroke is located upstream of the wing, interacts with the wing during the beginning of the stroke. A similar wing-wake interaction is observed for the fruit fly scale. However, remarkably, TEV_0 also formed in the previous stroke does not convect downward. Instead, TEV_0 interacts with the wing and with the LEV_1 that is being formed in the current stroke. The presence of these three vortices of varying intensities in the path of the wing during the backstroke results in multiple wing wake interactions. The first wing wake interaction may mitigate lift generation as the induced velocity from the TEV_0 and LEV_{0ii} is downward, decreasing the effective angle of attack. The second interaction between LEV_{0i} can be a potential lift enhancer often observed as a local peak in the lift history [17,18,80]. Moreover, again, the vortical structures at $t^* = 0$ and 0.5 are not similar to each other. At $t^* = 0$, three large scale vortices are observed upstream of the wing, while there are only two at $t^* = 0.5$. At fruit fly scale, wing-wake interaction at LE during back stroke takes place with one vortex. A single LEV and a single TEV are formed during the stroke.

5.4 Scaling of the time averaged lift

Current study focusses on the aeroelastic responses of a flapping wing at fruit fly and bumblebee scales. A comparison between the two insects is given in Table 5-2. Fruit

Table 5-2: Geometric, kinematic and aeroelastic parameters for fruit fly and bumblebee [64].

Insect	c_m [mm]	R [mm]	$f = \omega/(2\pi)$ [Hz]	ϕ_a [deg]	Re [10^3]	k [1]	St [1]	h_s^* [10^{-3}]	ρ^* [10^3]
Fruit Fly	0.96	3.0	240	75	0.25	0.19	0.25	0.6	1.1
Bumblebee	3.22	10.9	181	72	2.2	0.18	0.25	1.0	2.1

fly (*Drosophila melanogaster*) wings are about 3 mm in length whereas bumblebee (*Bombus impatiens*) wings are larger around 25 mm. Bumblebee wings are also thicker and denser when compared to fruit fly wings. Fruit flies flap their wings at higher frequency when compared to bumblebees with different stroke amplitudes. Moreover, fruit flies operate at a Reynolds number of $O(10^2)$ whereas bumblebees operate at higher Reynolds number of $O(10^3)$. It has been shown in Chapter 3 that there are indeed differences in aerodynamic and structural response at these two scales. Additionally, water tunnel scale results [63] when compared to fruit fly results in air showed similar aerodynamic features but structural response was dissimilar. At water tunnel scale, the density ratio $\rho^*=7.8$ is much lower when compared to fruit fly wing in air. These three scales not only differ by size and structural properties but also in kinematics and operating conditions.

Despite the similarities and differences seen at these varying scales, it is observed that the resulting lift coefficient scales with the dimensionless shape deformation parameter γ as shown in Figure 5-8(a). Normalized lift coefficient \bar{C}_L^* , is defined as

$$\bar{C}_L^* = \frac{\bar{C}_L}{\rho^* h_s^* k \{(f_1/f)^2 - 1\}}, \quad (5-1)$$

is carefully constructed according to dimensionless analysis using Buckingham's Π -theorem and using first order analysis of fluid-structure interaction of flapping wings [64]. Shape deformation parameter γ relates the deformation at the TE of the wing relative to the deformation at LE which can be seen as a passive pitch angle, or an angle of attack. Angle of attack is a critical measure of aerodynamics for both stationary wings [43] and flapping wings [1,63].

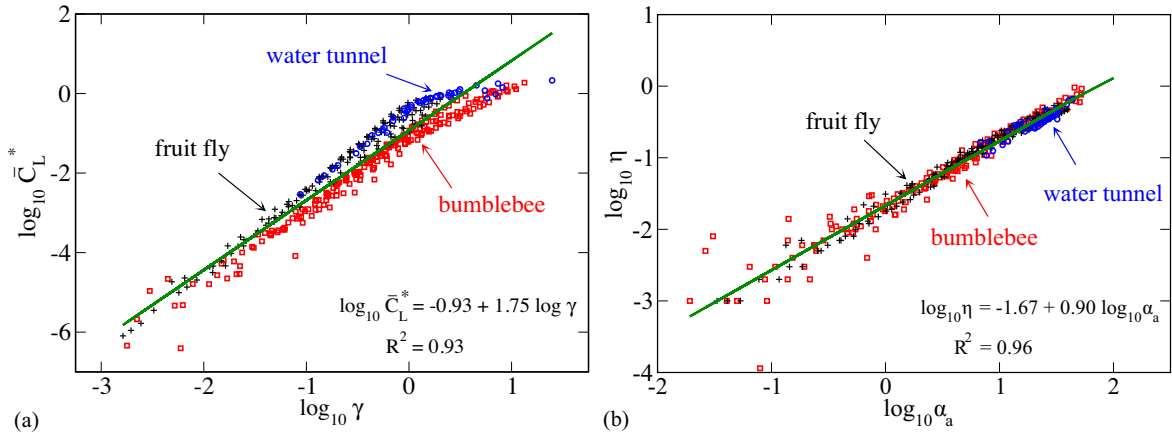


Figure 5-8. Scaling of dimensionless parameters at bumblebee, fruit fly and water tunnel scales [40]. (a) Scaling of normalized lift coefficient \bar{C}_L^* with shape deformation parameter γ . (b) Scaling of propulsive efficiency η with passive pitch amplitude α_a at bumblebee, fruit fly, and water tunnel scales.

Figure 5-8(a) shows on a logarithmic axis, scaling of the normalized lift coefficient with γ . Lift coefficients at fruit fly and water tunnel scales lie closely

correlated whereas lift coefficient at bumblebee scale is consistently lower. Although the higher Reynolds number of bumblebees suggest also a higher lift coefficient [77,80], the density and thickness ratios are also different, leading to smaller passive pitch angles and lower lift coefficient. Moreover, the observation of the reversed von Karman vortex street [8,81] also constitutes a nonlinear aeroelastic phenomenon that is not captured by the scaling analysis of flexible flapping wings [64].

The overall agreement of the γ -scaling suggests the role of rotational component of lift for purely passive pitching is not as important as for rigid wing with active rotation [63,82] as the γ -scaling does not account for the rotational force. Rotational force is weaker for a flexible wing as the pressure gradient due to the wing rotation partly becomes balanced by the elastic wing deformations [63,82]. Nevertheless, there is a strong scaling observed at all three scales.

A strong correlation between the propulsive efficiency, η , and angular amplitude, α_a , at fruit fly, bumblebee and water tunnel scales is shown in Figure 5-8(b). At the bottom left corner, scatter is observed. This region corresponds to highly rigid wings which flap almost vertically with negligible angular amplitude. Presence of such strong correlation may indicate existence of a universal mechanism involving flexible bending as suggested by a recent study [39]. Further investigation is needed to understand the physical reasons behind the strong correlation.

5.5 Comparison to experimental measurements of fruit flies and bumblebees

Flapping motion of a fruit fly (*Drosophila*) is characterized by a large-amplitude, low-frequency stroke [28]. For a rigid, dynamically-scaled robot, such motion was more

aerodynamically efficient than a short-amplitude, high-frequency motion of a honeybee [28,29]. An ecological explanation was that bees consume oral nectar, providing a high-energy source to carry much heavier loads [28]. These studies were based on measured wing kinematics of hovering fruit flies and bees. Based on these kinematics, quasi-steady models and dynamically scaled rigid wings were used to estimate the time history of lift.

Figure 5-9(a) shows a comparison of the reported lift on a fruit fly [47], and the resulting lift for the optimal efficiency motion from current numerical study (Section 5.3.1). Despite the difference that in the experiments the wing was three-dimensional and rigid with active rotations, while it is two-dimensional and purely passive in this study, overall time history of lift agree qualitatively. The timing of the lift peaks agrees well with the experimental data.

Moreover, Figure 5-9(b) shows the comparison of the passive pitch angle from the current aeroelastic computation with the fruit fly kinematics [47]. Similar to lift, the overall trend is strikingly similar. However, there are two main differences. First, the experimental amplitude is higher. Second, computational results show advanced rotation at the start of the stroke, whereas the experimental observation shows a slight delay. These differences may be attributed to the simplifying approximations in the current computational setup: two-dimensional plunging vs three-dimensional flapping; normal hovering vs a motion with nonzero elevation angles; uniform stiffness and thickness distribution of the wing vs anisotropic, non-uniform thickness distribution of the wing between root and tip: e.g. $h_s = 42.8 \times 10^{-6}$ m at the root and $h_s = 3.0 \times 10^{-6}$ m at the tip [62].

For a tethered fruit fly, a peak lift coefficient of $\bar{C}_L = 1.9$ was measured [29]. A lift of $\bar{C}_L = 1.6$ was shown to be sufficient to support body weight of a fruit fly. Fruit flies are reported to flap with a frequency of 218 Hz and a stroke angle of 140 degrees [47]. The

mean wing length was $l = 2.39$ mm and mean chord length was 0.90 mm, based on the regression area a in m^2 , $a = -2.023 \times 10^{-6} + 11.748 \times 10^{-3}$ and an aspect ratio of 2.65. The corresponding two-dimensional peak lift coefficient is $\bar{C}_L = 0.4$, which is obtained in the upper left region of the design space (see Figure 3-1(c)). The most efficiency case produces a lift of $\bar{C}_L = 1.0$ that exceeds the required value to support the weight of a fruit fly.

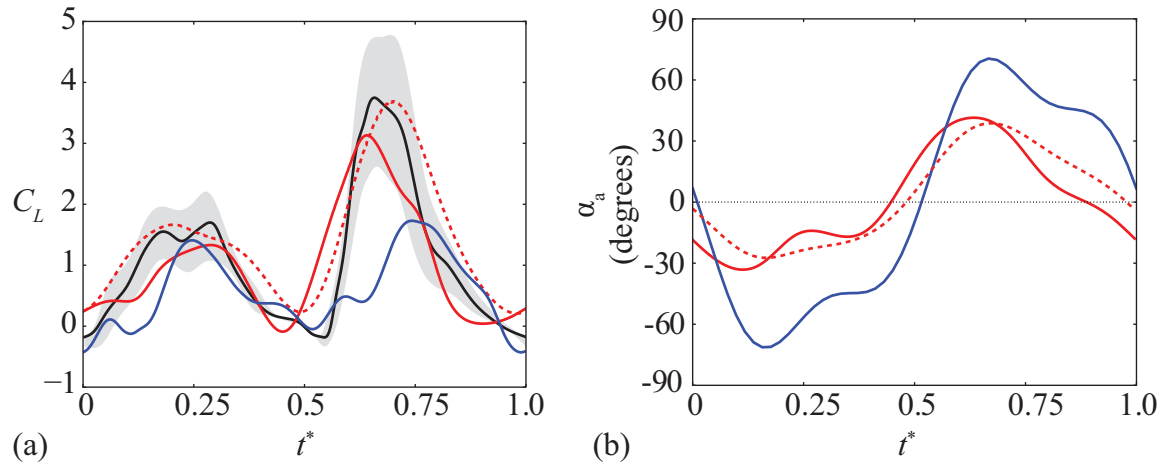


Figure 5-9. Comparison of time history of (a) lift and (b) pitching angle for the most efficient motion at (–) fruit fly scale [38] with (–) experimental measurements [47] (–) three dimensional rigid wing computational data for fruit fly [52] (–) water tunnel scale [63]. The band around the experimental curve in (a) indicates the upper and the lower bounds.

The reduced frequency and the frequency ratio for the optimal efficiency case were $k = 0.3$ and $f/f_1 = 0.35$. The aforementioned fruit fly parameters correspond to a reduced frequency of 0.2, which is close to the optimal efficiency case. The flexural chordwise stiffness of a fruit fly wing is unknown, but for dragonflies the operating frequency ratio is $f/f_1 = 0.16-0.46$ [83,84]. These comparisons suggest that the structural properties and kinematics of the fruit fly wing are optimized for an efficient passive wing rotation for a optimal flight.

Buchwald and Dudley [37] reported the measurements of the wing and the wing kinematics of hovering bumblebees (*Bombus impatiens*). The wing length was $R = 10.9$ mm and the mean chord $c_m = 3.22$ mm. Flapping stroke angle was $\Phi = 144$ degrees with a frequency of $f = 181$ Hz. If a two-dimensional approximation of the stroke at the wing tip is considered as the plunge motion as shown in Figure 5-10, the plunge amplitude becomes $h_a \approx \Phi R/2 = 13.7$ mm, where Φ in radians is used. The reduced frequency becomes $k = c_m/(2h_a) \approx 0.12$. Note that the reduced frequency for the fruit fly would become 0.15 instead of 0.19. The reason for these differences is that the mean tip velocity was used as reference velocity for $k = 0.19$, whereas maximum velocity is used as the reference velocity.

As shown in Figure 4-3(c), the optimal efficiency is obtained for $k = 0.1$ in the current study, which is close to the reduced frequency observed for a bumblebee of $k = 0.12$. Propulsive efficiency is highest at reduced frequency of $k = 0.1$ for all considered frequency ratios. Moreover, the lift generation is also the highest for $ff_1 < 0.3$. For higher frequency ratios, increasing reduced frequency to $k = 0.2$ enhances lift slightly. Operating frequency ratio for a bumblebee wing is unknown, but for dragonflies the operating frequency ratio is $ff_1 \in [0.16, 0.46]$ [83,84]. The qualitative agreement suggests that the structural properties and kinematics of the bumblebee wing may be optimized for an efficient passive wing rotation for an optimal flight.

Previous finding suggested that the kinematics of bees are aerodynamically less efficient than for example that of fruit flies [28]. The inefficiency of the bee kinematics was attributed to the smaller stroke amplitude with higher stroke frequencies, compared to those of fruit flies. However, the propulsive efficiency results in the current study suggests that the bee kinematics at $k = 0.1$ achieve high efficiencies. The discrepancy in

these results is due to the measured stroke angle of $\Phi = 144$ degrees for the hovering bumblebees, reported by Buchwald and Dudley [37]. On the other hand, Altshuler et al. [28] considered a stroke angle of $\Phi < 130$ degrees based on Ellington's data [85] on bumblebee (*Bombus hortorum*): $\Phi = 121$ degrees and bumblebee (*Bombus lucorum*): $\Phi = 130$ degrees. The corresponding reduced frequencies are $k = 0.14$ and $k = 0.13$ based on $R = 10.9$ mm and $c_m = 3.22$ mm, respectively, which still result in efficient performance.

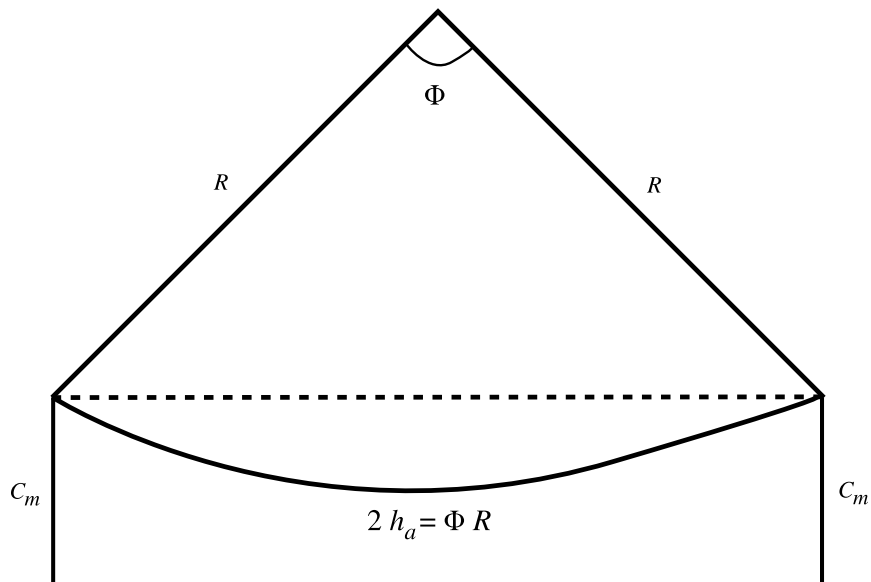


Figure 5-10. Graphical representation of two dimensional stroke at the wing tip at bumblebee scale. Wing length is represented by R , stroke angle by Φ and mean chord length by c_m .

CHAPTER 6

CONCLUSION

6.1 Summary

Aerodynamic and structural dynamic response was investigated for flexible flapping wings in hovering motion at fruit fly and bumblebee scales using a well validated numerical framework. Aerodynamic performance metrics, i.e. time-averaged lift \bar{C}_L , power \bar{C}_P and efficiency η , as a function of reduced frequency k and frequency ratio f/f_1 are explored. Reduced frequency is related to the plunge amplitude h_a of the motion, whereas frequency ratio is inversely proportional to the wing stiffness. The ranges of the reduced frequency and frequency ratio are also motivated by insect flight and were $0.1 < k < 3.0$ and $0.04 < f/f_1 < 0.7$, respectively. The resulting wing rotation is purely passive, due to a dynamic balance between wing inertia, elastic restoring force, and aerodynamic force.

At fruit fly scale, considered parameters are $Re = 100$, density ratio of $\rho^* = 1.0 \times 10^3$ and thickness ratio of $h_s^* = 1.5 \times 10^{-3}$. Whereas at bumblebee scale, density ratio of $\rho^* = 2.0 \times 10^3$ and thickness ratio of $h_s^* = 1.0 \times 10^{-3}$ at $Re = 1.0 \times 10^3$ are considered.

Simulations are carried out in a well validated numerical framework. A well-validated, coupled Navier-Stokes equation solver and linear Euler-Bernoulli beam solver are used to obtain the flow field and wing displacements respectively. The resulting forces and displacement are iterated at every time step until dynamic balance between the forces is achieved.

6.2 Concluding remarks

The observations from the current study at fruit fly and bumblebee scales are as follows.

For the fruit fly scale:

- Both time-averaged lift \bar{C}_L and power input \bar{C}_P increased with an increase in f/f_1 and k . The correlation of \bar{C}_P to k is stronger than that of \bar{C}_L .
- The highest lift is $\bar{C}_L = 3.3$, achieved at $k = 3.0$ and $f/f_1 = 0.7$. However, maximum power is required for this low-amplitude, high-frequency motion. As a result, the propulsive efficiency η is relatively lower.
- Optimal efficiency of $\eta = 0.6$ is obtained at $k = 0.3$ and $f/f_1 = 0.3$. The corresponding lift and power input coefficients are $\bar{C}_L = 1.0$ and $\bar{C}_P = 1.8$ respectively.
- The lift coefficient for the most efficient case is $\bar{C}_L = 1.0$, which is sufficient for a fruit fly to sustain its weight. The corresponding reduced frequency of $k=0.3$ is close to the value of $k = 0.2$ for a hovering fruit fly. The resulting passive pitch time history qualitatively agrees with the measured wing kinematics of fruit flies. These results suggest that fruit fly flight aims to conserve energy, rather than to generate large forces.

Current results, valid for the fruit fly scale, is compared to the previously reported results at the water tunnel scale: $\rho^*=7.8$ and $h_s^*=2.0 \times 10^{-2}$:

- Aerodynamic characteristics are similar in both scales. The case with the highest lift also required the highest power input. In both scales, the vortical evolution is characterized by more pronounced activities near the TE than at the LE for the highest lift cases. The most efficient case is found at a lower k and f/f_1 in both scales. The corresponding vortical evolution is characterized by a large LEV and its interaction with the wing.
- However, the structural response is different. At the fruit fly scale, all considered cases resulted in advanced rotation, while the phase lag φ exhibited advanced, symmetric, and delayed rotations, depending on f/f_1 for the water tunnel scale.
- The lift coefficient for both fruit fly and water tunnel scales could be scaled with the shape deformation parameter γ , despite their differences in the structural response.

For the bumblebee scale:

- Time-averaged lift increases with frequency ratio and but decreases with reduced frequency for reduced frequency $k < 1.5$. As the reduced frequency increases, wing deformation at the midstroke decreases, such that the resulting lift decreased as well. On the other hand, higher reduced frequency yields higher power input.
- The highest lift is $\bar{C}_L=1.43$, achieved at $k=1.0$ and $f/f_1=0.7$. But a moderate \bar{C}_P at this low-amplitude motion results in a relatively lower efficiency. Two LEVs were observed in the backward stroke, whereas a single LEV is generated during the forward stroke. The first LEV in the backward stroke paired with the LEV from the forward stroke and convect upwards.

- Optimal efficiency of $\eta = 0.95$ is achieved at $k = 0.1$ and $f/f_1 = 0.53$. At this optimal efficiency motion, a low power input $\bar{C}_P = 0.83$ and relatively high $\bar{C}_L = 0.79$ are observed. Dual LEVs are generated during the stroke, which interact with the wing in the subsequent stroke. Remarkably, a TEV convects upwards and interacts with the wing, resulting in a triple wing-wake interaction with the LEVs and the TEV during the backward stroke.

Comparison of the results at bumblebee scale with fruit fly scale shows the following observations:

- The overall vortex topology at the bumblebee scale is more chaotic, consistent with the higher Reynolds number.
- At the fruit fly scale, increasing reduced frequency resulted in a higher wing deformations at higher frequency ratios. As a result, the highest lift is obtained at the highest reduced frequency, frequency ratio combination in the design space. However, at the bumblebee scale, increasing reduced frequency beyond $k > 0.4$, leads to a lower deformations and, hence, lower lift. The highest lift is found at an intermediate reduced frequency at the highest frequency ratio.
- Despite the higher Reynolds number, the resulting lift coefficient is lower for the bumblebee scale due to the combined aeroelastic effects.
- Only advanced rotational modes are observed, which is also seen in at fruit fly scale.
- Normalized lift coefficient scales well with the shape deformation parameter γ for bumblebee, fruit fly, and water tunnel scales. A strong correlation between efficiency η and angular amplitude α_a is also observed for the three scales.

At fruit fly scale, the optimal efficiency motion resulted in a lift coefficient $\bar{C}_L = 1.0$, sufficient to sustain its flight. Reduced frequency of $k = 0.3$ at this optimal flight was comparable to that obtained from measurements. Furthermore, lift history corresponding to the optimal motion closely matched experimental measurements indicating that fruit fly flight is also optimal in nature.

Finally, the optimal efficiency motion for bumblebee is observed when the reduced frequency is $k = 0.1$ and frequency ratio $f/f_1 = 0.53$. The optimal reduced frequency is close to that of operating reduced frequency of bumblebees, which may suggest that bumblebee kinematics aims to optimize the performance, contrary to the previous analysis that the bee flight is aerodynamically inefficient. The discrepancy is in the measured stroke angles, which are $\Phi = 144$ degrees for the hovering bumblebees (*Bombus impatiens*), whereas the previous analysis used $\Phi < 130$ degrees, reported for bumblebee (*Bombus hortorum*) and bumblebee (*Bombus lucorum*). However, for $121 < \Phi < 130$ degrees, the corresponding reduced frequencies are $0.13 < k < 0.14$, which still belong to efficient motions.

6.3 Implications, consequences and limitations

A real fruit fly wing is highly anisotropic, complex, and three-dimensional with a wing rotation at the wing root. Moreover, we assumed a normal hovering motion without any stroke deviation, while fruit flies exhibit U-shaped or figure-of-eight-shaped trajectories. Therefore caution should be used made when extrapolating the current results to insect flight. Nevertheless, the involved simplifying assumptions to the considered chordwise flexible, two dimensional motion have been widely discussed and justified in the literature. Such abstracted configurations enable an analysis of the

important, first-order mechanism. The results discussed here may help our understanding of this intriguing, yet complex, multi-disciplinary fight of insects and development and design of bio-inspired micro robotic flyers.

6.4 Recommendation for future research

Current numerical computations were carried out by making certain simplifying assumptions. These assumptions were needed to understand the first order mechanisms associated with flapping wing flight, an area which is still in its infancy. Many intriguing observations were made in the current study which warrants an independent study in itself. Recommendations for future research in this topic are given below which addresses the improvements and observations that can be studied in further detail. The recommendations are:

1. Scaling effects at fruit fly and bumblebee scales was reported. In spite of the difference in operational Reynolds number and physical properties, the normalized lift coefficient scaled with shape deformation parameter γ . The same analysis can be extended to Hawkmoth (*Manduca sexta*) scale which is a larger insect with wing span close to 100 mm with an operational Reynolds number of $Re=6.0 \times 10^3$. Hawkmoth wings are known to deform dramatically during flight and is an ideal candidate to apply the FSI model to understand the kinematics of flapping flight and its effects on aeroelastic performance. In order to extend the studies to Hawkmoth scale, a finer mesh with higher number of grid points is needed. This mesh has to be carefully selected based on a grid and time sensitivity study.

2. In the current study, the three dimensional, highly anisotropic insect wing is simplified as a two dimensional flat plate. Additionally, stroke deviations were neglected. These simplifications help us to understand first order principles associated with flapping flight. But a more realistic model will involve CFD simulation of the full insect wing along with the body as seen in Figure 2-6(a) and (b). An actual insect wing follows a figure-of-eight shape motion. Hence, a more realistic model must take the stroke deviation into account.
3. Optimum points in the design space such as maximal lift and optimal efficiency can be identified with a more rigorous optimization process. One such method is by using surrogate models such as response surfaces or kriging which is an interpolation method that uses Gaussian process to predict optimal points.
4. Further investigation is needed to assess the possibility of performing water tunnel experiments to investigate the dynamic similarity of the physics of flexible flapping wings in air.
5. Figure 5-8(b) shows a strong scaling between propulsive efficiency η and angular amplitude α_a at fruit fly, bumblebee and water tunnel scales. This intriguing observation was merely reported in the current study. The reasons behind the existence of such scaling should be further explored.
6. Figures 5-3 and Figure 5-6 shows the wing shapes for the bumblebee and fruit fly at highest lift and optimal efficiency motions, respectively. The wing shapes obtained are purely advanced. For many insects it is reported that wings shapes are either symmetric or delayed [28,47,62]. The reasons behind purely advanced modes in the current study are currently unknown. A possible explanation is that the aerodynamic damping force at stroke reversal is not strong enough to

counteract the wing rotation due to inertial forces. Further analysis is needed to understand this behavior. A recent analytical study by Kang and Shyy [14] which focuses on interplay between aerodynamic, inertial and acceleration related forces may serve as a starting point.

7. Kang and Shyy [1] recently reported an analytical approach to predict aerodynamic performance and instantaneous deformation of flapping wings based on a linear beam equation with the Morrison equation. Results from current high fidelity simulations study can be used to compare with the kinematics prediction from the analytical model.

APPENDICES

APPENDIX A

TIME AVERAGING AT BUMBLEBEE SCALE

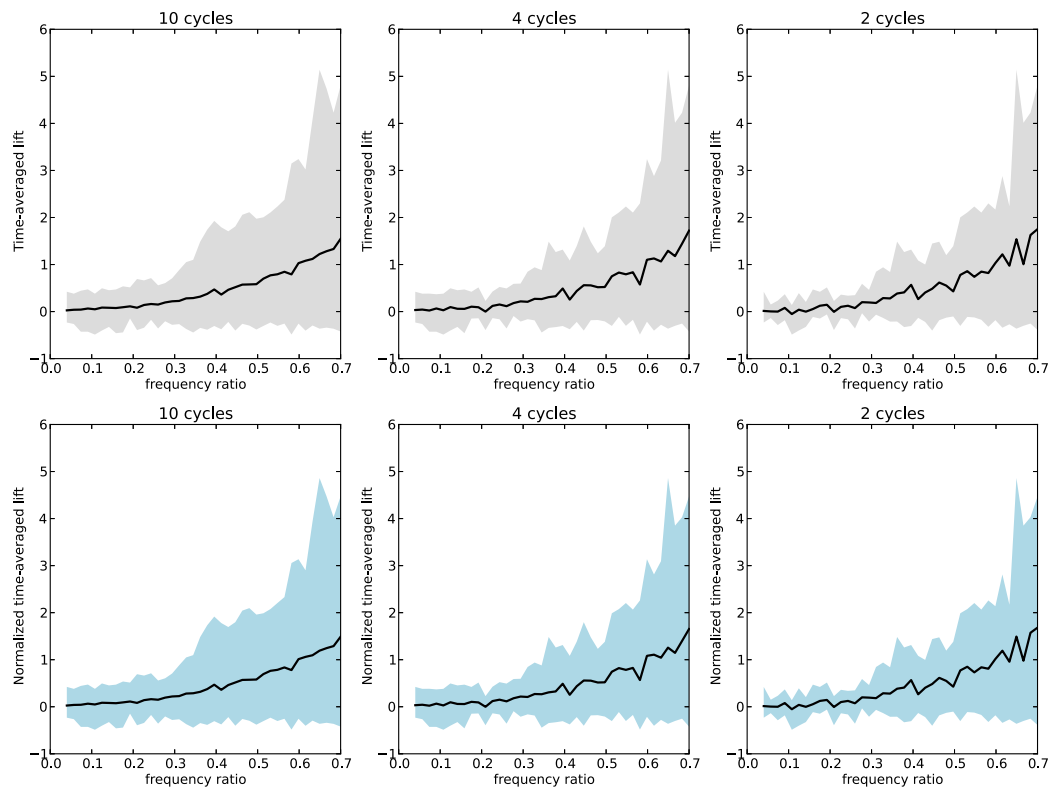


Figure A-1. Variation of time averaged lift with frequency ratio f/f_1 at bumblebee scale performed over 0-10 cycles (first column), 6-10 cycles (second column) and 8-10 cycles (third column). Bottom row corresponds to normalized lift coefficient. Grey and blue regions are bounded by maxima and minima within the motion cycles.

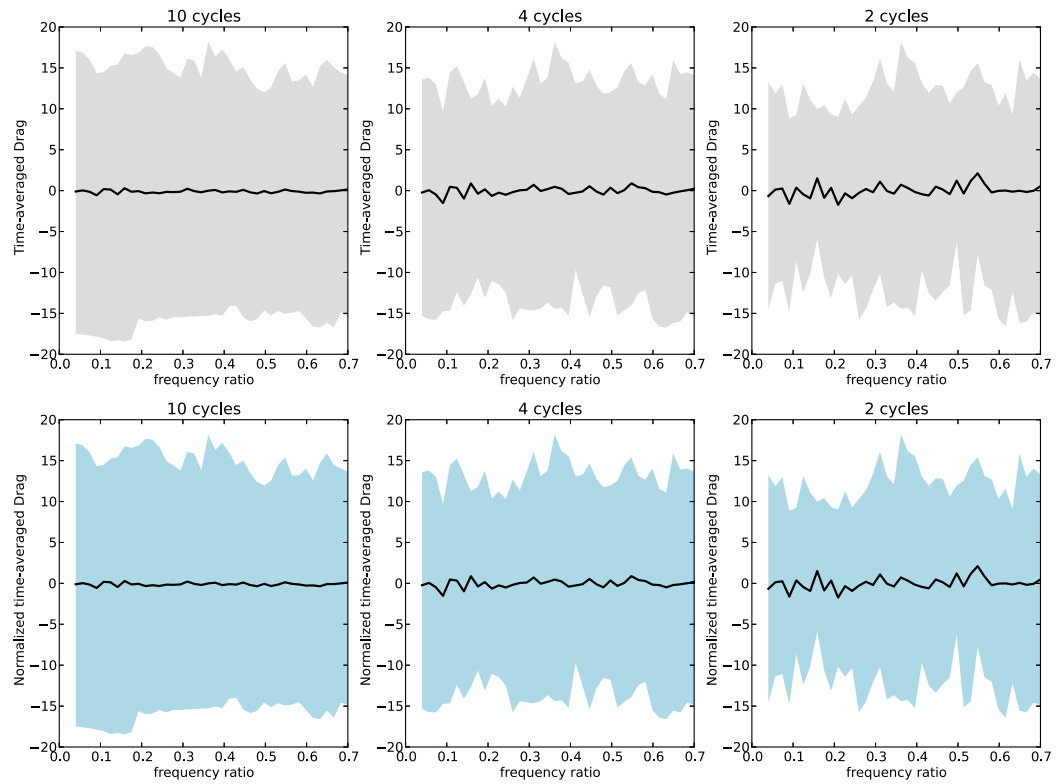


Figure A-2. Variation of time averaged drag with frequency ratio f/f_1 at bumblebee scale performed over 0-10 cycles (first column), 6-10 cycles (second column) and 8-10 cycles (third column). Bottom row corresponds to normalized drag coefficient. Grey and blue regions are bounded by maxima and minima within the motion cycles.

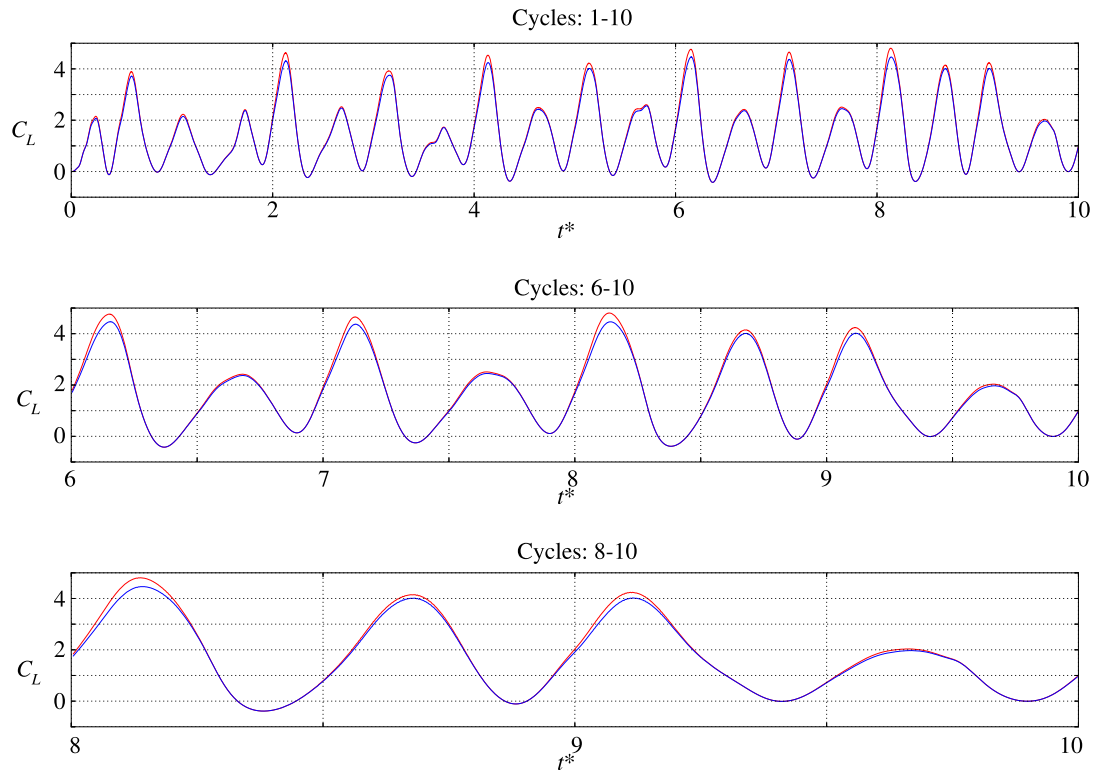


Figure A-3. Lift history at bumblebee scale for (top) 0-10 cycles (middle) 6-10 cycles (bottom) 8-10 cycles. Lift coefficient without normalization is shown in red and normalized lift coefficient is in blue.

APPENDIX B

TABLE OF COMPUTATIONAL RESULTS

Table B-1. Computational results at fruit fly scale: Aerodynamic parameters

Cases	k	f/f_1	E	γ	\bar{C}_L	\bar{C}_D	h_a	\bar{C}_P	η	Π_1
1	0.1	0.04	1.29E+010	0.049	0.068	-0.209	5	1.355	0.05	3.641
2	0.1	0.075	3.71E+009	0.171	0.192	-0.088	5	1.318	0.146	1.043
3	0.1	0.109	1.73E+009	0.37	0.379	0.013	5	1.288	0.294	0.486
4	0.1	0.144	9.96E+008	0.648	0.45	-0.139	5	1.014	0.443	0.28
5	0.2	0.04	5.18E+010	0.024	0.033	0.139	2.5	1.576	0.021	14.564
6	0.2	0.075	1.48E+010	0.086	0.09	0.165	2.5	1.567	0.057	4.172
7	0.2	0.109	6.91E+009	0.185	0.176	0.207	2.5	1.547	0.114	1.944
8	0.2	0.144	3.98E+009	0.324	0.292	0.357	2.5	1.581	0.184	1.12
9	0.2	0.179	5.87E+008	0.505	0.44	0.305	2.5	1.651	0.266	0.165
10	0.2	0.214	1.81E+009	0.73	0.592	0.346	2.5	1.655	0.358	0.51
11	0.2	0.248	1.34E+009	1.003	0.594	0.244	2.5	1.399	0.424	0.378
12	0.2	0.283	1.03E+009	1.33	0.643	0.032	2.5	1.341	0.48	0.291
13	0.3	0.04	1.17E+011	0.016	0.016	-0.015	1.667	1.901	0.008	32.768
14	0.3	0.075	3.34E+010	0.057	0.081	0.13	1.667	1.901	0.043	9.386
15	0.3	0.109	1.56E+010	0.123	0.162	0.215	1.667	1.903	0.085	4.375

16	0.3	0.144	8.96E+009	0.216	0.258	0.215	1.667	1.931	0.134	2.521
17	0.3	0.179	5.82E+009	0.336	0.404	0.298	1.667	1.957	0.207	1.637
18	0.3	0.214	4.08E+009	0.487	0.555	0.363	1.667	1.911	0.291	1.148
19	0.3	0.248	3.02E+009	0.669	0.671	0.259	1.667	1.963	0.342	0.85
20	0.3	0.283	2.32E+009	0.886	0.819	0.235	1.667	1.932	0.424	0.654
21	0.3	0.318	1.84E+009	1.143	0.809	0.145	1.667	1.712	0.472	0.519
22	0.3	0.353	1.50E+009	1.444	1.021	0.116	1.667	1.794	0.569	0.422
23	0.4	0.04	2.07E+011	0.012	0.014	-0.07	1.25	2.18	0.007	58.254
24	0.4	0.075	5.93E+010	0.043	0.07	0.046	1.25	2.196	0.032	16.687
25	0.4	0.109	2.77E+010	0.093	0.166	0.167	1.25	2.262	0.074	7.777
26	0.4	0.144	1.59E+010	0.162	0.273	0.198	1.25	2.287	0.119	4.482
27	0.4	0.179	1.03E+010	0.252	0.405	0.191	1.25	2.341	0.173	2.911
28	0.4	0.214	7.26E+009	0.365	0.555	0.293	1.25	2.319	0.239	2.041
29	0.4	0.248	5.37E+009	0.502	0.688	0.316	1.25	2.271	0.303	1.51
30	0.4	0.283	4.13E+009	0.665	0.798	0.334	1.25	2.153	0.371	1.162
31	0.4	0.318	3.28E+009	0.857	0.878	0.286	1.25	2.094	0.419	0.922
32	0.4	0.353	2.67E+009	1.083	1.065	0.242	1.25	2.171	0.49	0.75
33	0.4	0.387	2.21E+009	1.347	1.179	0.249	1.25	2.198	0.536	0.621
34	1	0.04	1.29E+012	0.005	0.021	0.016	0.5	3.412	0.006	364.089
35	1	0.075	3.71E+011	0.017	0.047	-0.021	0.5	3.394	0.014	104.294
36	1	0.109	1.73E+011	0.037	0.102	-0.043	0.5	3.328	0.031	48.608
37	1	0.144	9.96E+010	0.065	0.139	0.012	0.5	3.234	0.043	28.011
38	1	0.179	6.47E+010	0.101	0.19	0.071	0.5	3.224	0.059	18.192
39	1	0.214	4.54E+010	0.146	0.318	0.14	0.5	3.621	0.088	12.758
40	1	0.248	3.36E+010	0.201	0.366	0.058	0.5	3.397	0.108	9.44
41	1	0.283	2.58E+010	0.266	0.522	-0.134	0.5	3.59	0.146	7.266
42	1	0.318	2.05E+010	0.343	0.739	-0.129	0.5	3.818	0.194	5.764
43	1	0.353	1.67E+010	0.433	0.899	-0.052	0.5	3.783	0.238	4.685
44	1	0.387	1.38E+010	0.539	1.089	0.025	0.5	3.896	0.28	3.882

45	1	0.422	1.16E+010	0.661	1.296	0.147	0.5	4.061	0.319	3.27
46	1	0.457	9.92E+009	0.805	1.489	0.221	0.5	4.239	0.351	2.791
47	1	0.492	8.57E+009	0.972	1.64	0.187	0.5	4.368	0.375	2.411
48	1	0.526	7.48E+009	1.169	1.739	0.114	0.5	4.416	0.394	2.103
49	1	0.561	6.58E+009	1.401	1.805	0.056	0.5	4.416	0.409	1.851
50	1	0.596	5.84E+009	1.679	1.863	0.043	0.5	4.405	0.423	1.641
51	1	0.631	5.21E+009	2.013	1.945	0.053	0.5	4.374	0.445	1.465
52	1	0.665	4.68E+009	2.422	2.076	0.033	0.5	4.328	0.48	1.316
53	1.5	0.04	2.91E+012	0.003	0.006	0.074	0.333	3.815	0.002	819.200
54	1.5	0.075	8.34E+011	0.011	0.021	0.075	0.333	3.851	0.005	234.661
55	1.5	0.109	3.89E+011	0.025	0.047	0.074	0.333	3.913	0.012	109.368
56	1.5	0.144	2.24E+011	0.043	0.09	0.059	0.333	4.008	0.022	63.025
57	1.5	0.179	1.46E+011	0.067	0.157	-0.009	0.333	4.131	0.038	40.932
58	1.5	0.214	1.02E+011	0.097	0.22	0.098	0.333	4.324	0.051	28.705
59	1.5	0.248	7.55E+010	0.134	0.334	-0.199	0.333	4.311	0.077	21.239
60	1.5	0.283	5.81E+010	0.177	0.42	-0.208	0.333	4.491	0.094	16.348
61	1.5	0.318	4.61E+010	0.229	0.538	-0.183	0.333	4.62	0.116	12.97
62	1.5	0.353	3.75E+010	0.289	0.665	-0.139	0.333	4.705	0.141	10.541
63	1.5	0.387	3.11E+010	0.359	0.834	-0.128	0.333	4.856	0.172	8.735
64	1.5	0.422	2.62E+010	0.441	1.046	-0.15	0.333	5.088	0.206	7.356
65	1.5	0.457	2.23E+010	0.536	1.327	-0.062	0.333	5.414	0.245	6.28
66	1.5	0.492	1.93E+010	0.648	1.592	0.021	0.333	5.706	0.279	5.424
67	1.5	0.526	1.68E+010	0.779	1.806	0.039	0.333	5.943	0.304	4.732
68	1.5	0.561	1.48E+010	0.934	1.992	0.023	0.333	6.137	0.325	4.164
69	1.5	0.596	1.31E+010	1.119	2.159	0	0.333	6.281	0.344	3.693
70	1.5	0.631	1.17E+010	1.342	2.31	-0.009	0.333	6.371	0.363	3.297
71	1.5	0.665	1.05E+010	1.615	2.453	-0.001	0.333	6.398	0.383	2.962
72	1.5	0.7	9.51E+009	1.954	2.605	0.017	0.333	6.342	0.411	2.675
73	2	0.04	5.18E+012	0.002	0.004	0.02	0.25	3.972	0.001	1456.35

74	2	0.075	1.48E+012	0.009	0.013	0.021	0.25	4.005	0.003	417.175
75	2	0.109	6.91E+011	0.019	0.028	0.022	0.25	4.06	0.007	194.432
76	2	0.144	3.98E+011	0.032	0.051	0.022	0.25	4.139	0.012	112.045
77	2	0.179	2.59E+011	0.05	0.081	0.02	0.25	4.246	0.019	72.767
78	2	0.214	1.81E+011	0.073	0.115	0.009	0.25	4.393	0.026	51.032
79	2	0.248	1.34E+011	0.1	0.211	-0.01	0.25	4.595	0.046	37.758
80	2	0.283	1.03E+011	0.133	0.309	-0.117	0.25	4.764	0.065	29.062
81	2	0.318	8.20E+010	0.171	0.44	-0.19	0.25	4.893	0.09	23.058
82	2	0.353	6.66E+010	0.217	0.544	-0.162	0.25	5.127	0.106	18.739
83	2	0.387	5.52E+010	0.269	0.664	-0.142	0.25	5.447	0.122	15.529
84	2	0.422	4.65E+010	0.331	0.843	-0.135	0.25	5.766	0.146	13.078
85	2	0.457	3.97E+010	0.402	1.096	-0.103	0.25	6.196	0.177	11.165
86	2	0.492	3.43E+010	0.486	1.375	-0.056	0.25	6.658	0.207	9.643
87	2	0.526	2.99E+010	0.584	1.669	-0.036	0.25	7.112	0.235	8.412
88	2	0.561	2.63E+010	0.701	1.968	-0.024	0.25	7.542	0.261	7.403
89	2	0.596	2.33E+010	0.839	2.248	-0.02	0.25	7.916	0.284	6.565
90	2	0.631	2.08E+010	1.007	2.503	-0.022	0.25	8.217	0.305	5.861
91	2	0.665	1.87E+010	1.211	2.736	-0.015	0.25	8.422	0.325	5.265
92	2	0.7	1.69E+010	1.466	2.947	0.004	0.25	8.499	0.347	4.755
93	2.5	0.04	8.09E+012	0.002	0.003	0.007	0.2	4.109	0.001	2275.55
94	2.5	0.075	2.32E+012	0.007	0.011	0.007	0.2	4.144	0.003	651.835
95	2.5	0.109	1.08E+012	0.015	0.024	0.008	0.2	4.201	0.006	303.800
96	2.5	0.144	6.22E+011	0.026	0.042	0.008	0.2	4.283	0.01	175.071
97	2.5	0.179	4.04E+011	0.04	0.066	0.008	0.2	4.391	0.015	113.699
98	2.5	0.214	2.84E+011	0.058	0.097	-0.001	0.2	4.529	0.021	79.737
99	2.5	0.248	2.10E+011	0.08	0.14	0.006	0.2	4.718	0.03	58.997
100	2.5	0.283	1.61E+011	0.106	0.194	-0.013	0.2	4.912	0.039	45.41
101	2.5	0.318	1.28E+011	0.137	0.279	-0.026	0.2	5.16	0.054	36.028
102	2.5	0.353	1.04E+011	0.173	0.418	-0.085	0.2	5.505	0.076	29.28

103	2.5	0.387	8.63E+010	0.215	0.577	-0.15	0.2	5.805	0.099	24.264
104	2.5	0.422	7.27E+010	0.265	0.72	-0.149	0.2	6.173	0.117	20.435
105	2.5	0.457	6.20E+010	0.322	0.926	-0.115	0.2	6.68	0.139	17.445
106	2.5	0.492	5.36E+010	0.389	1.13	-0.111	0.2	7.254	0.156	15.067
107	2.5	0.526	4.67E+010	0.468	1.42	-0.102	0.2	7.851	0.181	13.144
108	2.5	0.561	4.11E+010	0.561	1.801	-0.079	0.2	8.568	0.21	11.566
109	2.5	0.596	3.65E+010	0.672	2.182	-0.062	0.2	9.244	0.236	10.257
110	2.5	0.631	3.26E+010	0.805	2.546	-0.049	0.2	9.827	0.259	9.158
111	2.5	0.665	2.93E+010	0.969	2.884	-0.035	0.2	10.293	0.28	8.227
112	2.5	0.7	2.64E+010	1.172	3.186	-0.012	0.2	10.586	0.301	7.43
113	3	0.04	1.17E+013	0.002	0.003	0.002	0.167	4.227	0.001	3276.80
114	3	0.075	3.34E+012	0.006	0.009	0.002	0.167	4.262	0.002	938.643
115	3	0.109	1.56E+012	0.012	0.021	0.002	0.167	4.321	0.005	437.472
116	3	0.144	8.96E+011	0.022	0.036	0.002	0.167	4.404	0.008	252.102
117	3	0.179	5.82E+011	0.034	0.058	0.002	0.167	4.514	0.013	163.727
118	3	0.214	4.08E+011	0.049	0.086	-0.002	0.167	4.655	0.018	114.822
119	3	0.248	3.02E+011	0.067	0.118	0.001	0.167	4.845	0.024	84.956
120	3	0.283	2.32E+011	0.089	0.166	-0.005	0.167	5.041	0.033	65.39
121	3	0.318	1.84E+011	0.114	-0.008	10.303	0.167	0	0.04	51.88
122	3	0.353	1.50E+011	0.144	0.308	-0.035	0.167	5.67	0.054	42.163
123	3	0.387	1.24E+011	0.18	0.456	-0.075	0.167	6.111	0.075	34.94
124	3	0.422	1.05E+011	0.22	0.624	-0.136	0.167	6.543	0.095	29.426
125	3	0.457	8.93E+010	0.268	0.795	-0.149	0.167	7.073	0.112	25.121
126	3	0.492	7.71E+010	0.324	0.895	-0.011	0.167	7.937	0.113	21.696
127	3	0.526	6.73E+010	0.39	1.171	-0.019	0.167	8.556	0.137	18.927
128	3	0.561	5.92E+010	0.467	1.563	-0.114	0.167	9.262	0.169	16.656
129	3	0.596	5.25E+010	0.56	2.019	-0.113	0.167	10.232	0.197	14.77
130	3	0.631	4.69E+010	0.671	2.471	-0.093	0.167	11.152	0.222	13.188
131	3	0.665	4.21E+010	0.807	2.909	-0.072	0.167	11.943	0.244	11.846

132	3	0.7	3.80E+010	0.977	3.315	-0.039	0.167	12.536	0.264	10.7
133	0.75	0.04	7.28E+011	0.007	0.019	0.002	0.667	2.679	0.007	204.800
134	0.75	0.075	2.09E+011	0.023	0.059	-0.081	0.667	2.738	0.022	58.665
135	0.75	0.109	9.72E+010	0.049	0.138	0.152	0.667	3.352	0.041	27.342
136	0.75	0.144	5.60E+010	0.086	0.184	0.11	0.667	3.094	0.059	15.756
137	0.75	0.179	3.64E+010	0.135	0.244	-0.029	0.667	2.796	0.087	10.233
138	0.75	0.214	2.55E+010	0.195	0.437	0.208	0.667	3.522	0.124	7.176
139	0.75	0.248	1.89E+010	0.268	0.501	-0.035	0.667	3.14	0.16	5.31
140	0.75	0.283	1.45E+010	0.355	0.735	-0.146	0.667	3.511	0.209	4.087
141	0.75	0.318	1.15E+010	0.457	0.886	0.023	0.667	3.253	0.272	3.243
142	0.75	0.353	9.37E+009	0.578	0.976	0.164	0.667	3.152	0.31	2.635
143	0.75	0.387	7.76E+009	0.718	1.153	0.323	0.667	3.281	0.351	2.184
144	0.75	0.422	6.54E+009	0.882	1.358	0.377	0.667	3.436	0.395	1.839
145	0.75	0.457	5.58E+009	1.073	1.509	0.322	0.667	3.533	0.427	1.57
146	0.75	0.492	4.82E+009	1.296	1.584	0.222	0.667	3.548	0.446	1.356
147	0.75	0.526	4.21E+009	1.559	1.607	0.135	0.667	3.514	0.457	1.183
148	0.75	0.561	3.70E+009	1.869	1.625	0.11	0.667	3.478	0.467	1.041

Table B-2. Computational results at fruit fly scale: Structural parameters

Cases	α_m	α_e	α_a	φ	Cases	α_m	α_e	α_a	φ
1	87.71	91.13	2.55	90.70	75	89.83	90.37	0.41	98.70
2	82.76	94.09	8.31	92.39	76	89.69	90.65	0.72	98.44
3	69.60	96.45	21.40	93.32	77	89.49	91.01	1.13	90.03
4	72.22	110.59	27.20	100.12	78	89.21	91.45	1.65	90.11
5	89.30	90.36	0.79	90.23	79	88.78	92.00	2.34	90.23
6	87.61	91.29	2.72	90.79	80	88.21	92.77	3.30	90.41
7	85.30	92.79	5.46	91.67	81	88.34	93.93	4.26	90.64
8	82.93	94.85	8.58	92.82	82	88.21	94.63	4.96	90.91
9	79.08	98.09	13.60	94.48	83	87.74	95.40	5.85	91.24
10	73.78	101.84	20.08	96.17	84	87.08	96.22	6.87	91.70
11	70.05	108.67	27.32	99.16	85	85.76	97.45	8.57	92.39
12	65.77	111.50	32.40	100.12	86	83.69	99.22	11.17	92.79
13	89.58	90.31	0.53	90.20	87	81.32	101.07	14.06	93.23
14	88.62	91.01	1.71	90.63	88	78.75	102.73	16.99	93.68
15	87.16	92.06	3.51	91.27	89	75.96	104.07	19.88	94.34
16	85.46	93.44	5.70	92.06	90	72.97	105.03	22.72	95.23
17	83.03	96.00	9.20	93.47	91	69.85	105.58	25.47	96.10
18	79.93	99.89	14.11	95.45	92	66.68	105.61	28.06	96.83
19	73.50	102.01	20.41	96.25	93	89.99	90.04	0.04	97.36
20	71.63	106.61	24.76	98.32	94	89.95	90.13	0.14	97.66
21	72.41	109.55	26.30	99.68	95	89.89	90.29	0.31	97.75
22	65.84	111.83	32.57	100.26	96	89.79	90.51	0.55	97.60
23	89.73	90.29	0.40	90.18	97	89.66	90.79	0.86	90.02
24	89.04	90.97	1.37	90.61	98	89.48	91.14	1.25	90.09

25	87.93	91.93	2.83	91.19	99	89.21	91.58	1.76	90.18
26	86.82	93.23	4.53	91.96	100	88.84	92.20	2.49	90.32
27	85.00	95.03	7.10	92.97	101	89.01	93.13	3.28	90.50
28	82.56	97.23	10.38	94.13	102	88.78	93.62	3.82	90.72
29	78.98	99.60	14.62	95.27	103	88.40	94.23	4.52	90.99
30	76.90	103.09	18.52	96.93	104	88.05	94.88	5.26	91.36
31	76.10	105.96	21.16	98.26	105	87.26	95.80	6.42	91.92
32	72.83	108.03	24.90	99.03	106	85.77	97.29	8.43	92.21
33	67.25	109.75	30.13	95.68	107	84.01	98.87	10.71	92.57
34	89.92	90.11	0.13	100.21	108	81.83	100.47	13.28	92.94
35	89.72	90.37	0.46	100.79	109	79.40	101.89	15.92	93.45
36	89.41	90.81	1.00	101.00	110	76.69	103.00	18.61	94.25
37	88.99	91.39	1.72	99.46	111	73.70	103.72	21.30	95.06
38	88.34	92.20	2.76	90.07	112	70.56	103.92	23.91	95.82
39	87.16	93.08	4.19	90.23	113	89.99	90.03	0.03	96.44
40	86.35	94.46	5.77	90.51	114	89.96	90.11	0.12	96.88
41	84.97	95.72	7.62	90.87	115	89.92	90.24	0.25	97.08
42	84.36	97.86	9.67	91.36	116	89.85	90.42	0.44	97.02
43	84.47	99.54	11.03	91.87	117	89.75	90.66	0.70	90.02
44	83.23	100.93	12.85	92.67	118	89.63	90.95	1.01	90.07
45	80.47	102.82	15.97	93.36	119	89.44	91.30	1.42	90.15
46	76.36	105.37	20.55	94.52	120	89.17	91.81	1.99	90.27
47	72.05	107.89	25.34	95.42	121	89.34	92.58	2.66	90.41
48	68.37	109.81	29.34	96.10	122	89.14	92.98	3.10	90.60
49	65.34	111.22	32.53	96.95	123	88.81	93.53	3.72	90.82
50	62.83	112.11	35.03	97.99	124	88.54	94.09	4.35	91.13
51	60.54	112.17	36.87	98.92	125	87.98	94.86	5.26	91.60

52	57.83	111.89	38.92	99.56	126	86.72	96.33	7.13	91.83
53	89.96	90.07	0.08	99.97	127	85.70	97.42	8.58	92.16
54	89.87	90.24	0.27	100.19	128	84.01	98.77	10.62	92.49
55	89.71	90.51	0.59	100.06	129	81.88	100.20	13.04	92.92
56	89.47	90.89	1.04	99.78	130	79.44	101.41	15.55	93.74
57	89.11	91.39	1.65	90.04	131	76.68	102.28	18.12	94.32
58	88.57	91.97	2.44	90.15	132	73.65	102.66	20.68	95.00
59	87.89	92.71	3.44	90.32	133	89.89	90.15	0.18	96.21
60	86.89	93.78	4.90	90.56	134	89.62	90.52	0.64	96.52
61	87.00	95.44	6.21	90.87	135	89.04	91.20	1.54	96.57
62	87.04	96.41	7.07	91.22	136	88.41	92.11	2.64	90.09
63	86.40	97.26	8.10	91.66	137	87.62	92.99	3.82	90.33
64	85.20	98.40	9.67	92.28	138	85.28	94.55	6.56	90.75
65	83.03	100.14	12.31	93.24	139	84.23	96.76	8.89	91.31
66	80.10	102.36	15.83	93.79	140	82.23	97.38	10.72	91.82
67	76.98	104.38	19.40	94.24	141	82.22	100.25	12.87	92.70
68	73.87	105.97	22.69	94.83	142	81.93	102.20	14.63	93.92
69	70.78	107.16	25.76	95.69	143	79.30	103.76	17.43	94.20
70	67.73	107.97	28.62	96.70	144	74.83	106.14	22.15	95.72
71	64.72	108.33	31.23	97.55	145	69.47	109.18	28.09	96.70
72	61.62	108.15	33.69	98.15	146	64.72	111.89	33.44	97.36
73	89.98	90.05	0.05	98.52	147	61.28	113.83	37.32	98.27
74	89.92	90.17	0.19	98.71	148	59.12	114.73	39.56	99.35

Table B-3: Computational results at Bumblebee scale: Aerodynamic parameters

Cases	k	f/f_1	E	γ	\bar{C}_L	\bar{C}_D	h_a	\bar{C}_P	η	Π_1
1	0.1	0.04	5.84E+010	0.045	0.035	0.035	5	1.553	0.022	4.871
2	0.1	0.075	1.67E+010	0.156	0.073	0.056	5	1.435	0.051	1.395
3	0.1	0.109	7.80E+009	0.338	0.148	0.358	5	1.378	0.107	0.65
4	0.1	0.144	4.50E+009	0.592	0.263	0.063	5	1.447	0.181	0.375
5	0.1	0.179	2.92E+009	0.921	0.34	0.165	5	1.304	0.261	0.243
6	0.1	0.214	2.05E+009	1.333	0.414	-0.068	5	1.268	0.326	0.171
7	0.1	0.248	1.52E+009	1.832	0.417	-0.06	5	1.048	0.398	0.126
8	0.1	0.283	1.17E+009	2.428	0.401	0.067	5	0.904	0.444	0.097
9	0.1	0.318	9.25E+008	3.131	0.476	0.005	5	0.919	0.518	0.077
10	0.1	0.353	7.52E+008	3.956	0.437	-0.111	5	0.81	0.539	0.063
11	0.1	0.387	6.23E+008	4.918	0.533	0.023	5	0.83	0.642	0.052
12	0.1	0.422	5.25E+008	6.039	0.554	0.004	5	0.805	0.688	0.044
13	0.1	0.457	4.48E+008	7.347	0.629	-0.088	5	0.816	0.77	0.037
14	0.1	0.492	3.87E+008	8.876	0.748	-0.021	5	0.813	0.92	0.032
15	0.1	0.526	3.38E+008	10.672	0.79	0.049	5	0.828	0.954	0.028
16	0.2	0.04	2.34E+011	0.022	0.007	0.072	2.5	1.442	0.005	19.483
17	0.2	0.075	6.70E+010	0.078	0.006	0.224	2.5	1.365	0.004	5.581
18	0.2	0.109	3.12E+010	0.169	0.045	-0.217	2.5	1.381	0.033	2.601
19	0.2	0.144	1.80E+010	0.296	0.061	0.525	2.5	1.322	0.046	1.499
20	0.2	0.179	1.17E+010	0.461	0.083	0.294	2.5	1.269	0.065	0.973
21	0.2	0.214	8.19E+009	0.666	0.137	-0.086	2.5	1.268	0.108	0.683
22	0.2	0.248	6.06E+009	0.916	0.327	0.105	2.5	1.613	0.203	0.505
23	0.2	0.283	4.67E+009	1.214	0.314	0.493	2.5	1.441	0.218	0.389
24	0.2	0.318	3.70E+009	1.566	0.392	0.17	2.5	1.452	0.27	0.308
25	0.2	0.353	3.01E+009	1.978	0.514	0.081	2.5	1.438	0.357	0.251
26	0.2	0.387	2.49E+009	2.459	0.628	0.03	2.5	1.548	0.406	0.208

27	0.2	0.422	2.10E+009	3.019	0.439	-0.135	2.5	1.288	0.341	0.175
28	0.2	0.457	1.79E+009	3.673	0.541	-0.095	2.5	1.177	0.46	0.149
29	0.2	0.492	1.55E+009	4.438	0.767	0.096	2.5	1.525	0.503	0.129
30	0.2	0.526	1.35E+009	5.336	0.546	-0.024	2.5	1.222	0.446	0.113
31	0.2	0.561	1.19E+009	6.398	0.986	0.069	2.5	1.461	0.674	0.099
32	0.2	0.596	1.05E+009	7.664	0.774	0.139	2.5	1.23	0.629	0.088
33	0.2	0.631	9.41E+008	9.191	0.672	0.161	2.5	1.079	0.623	0.078
34	0.2	0.665	8.45E+008	11.058	0.649	0.006	2.5	1.053	0.617	0.07
35	0.2	0.7	7.63E+008	13.381	0.781	0.03	2.5	1.024	0.763	0.064
36	0.3	0.04	5.26E+011	0.015	0.02	-0.335	1.666	1.44	0.014	43.836
37	0.3	0.075	1.51E+011	0.052	0.034	0.135	1.666	1.779	0.019	12.557
38	0.3	0.109	7.02E+010	0.113	0.042	-0.137	1.666	2.152	0.019	5.852
39	0.3	0.144	4.05E+010	0.197	0.077	-0.646	1.666	1.477	0.052	3.373
40	0.3	0.179	2.63E+010	0.307	0.128	-0.184	1.666	1.74	0.074	2.19
41	0.3	0.214	1.84E+010	0.444	0.153	-0.175	1.666	1.728	0.089	1.536
42	0.3	0.248	1.36E+010	0.611	0.2	-0.521	1.666	1.628	0.123	1.137
43	0.3	0.283	1.05E+010	0.809	0.208	-0.415	1.666	1.951	0.107	0.875
44	0.3	0.318	8.33E+009	1.044	0.359	-0.049	1.666	1.82	0.197	0.694
45	0.3	0.353	6.77E+009	1.319	0.383	0.18	1.666	1.686	0.227	0.564
46	0.3	0.387	5.61E+009	1.639	0.39	-0.186	1.666	1.5	0.26	0.467
47	0.3	0.422	4.72E+009	2.013	0.471	0.212	1.666	1.649	0.285	0.394
48	0.3	0.457	4.03E+009	2.449	0.597	0.164	1.666	1.785	0.335	0.336
49	0.3	0.492	3.48E+009	2.959	0.648	0.104	1.666	1.642	0.394	0.29
50	0.3	0.526	3.04E+009	3.557	0.636	0.437	1.666	1.668	0.381	0.253
51	0.3	0.561	2.67E+009	4.265	0.538	0.168	1.666	1.526	0.353	0.223
52	0.3	0.596	2.37E+009	5.11	0.787	0.267	1.666	1.677	0.469	0.198
53	0.3	0.631	2.12E+009	6.127	0.944	0.245	1.666	1.803	0.524	0.176
54	0.3	0.665	1.90E+009	7.372	0.662	-0.011	1.666	1.478	0.448	0.158
55	0.3	0.7	1.72E+009	8.921	0.998	0.142	1.666	1.668	0.598	0.143

56	0.4	0.04	9.35E+011	0.011	-0.013	0.317	1.25	2.082	-0.006	77.931
57	0.4	0.075	2.68E+011	0.039	-0.013	-0.417	1.25	1.983	-0.006	22.323
58	0.4	0.109	1.25E+011	0.084	0.054	0.243	1.25	1.802	0.03	10.404
59	0.4	0.144	7.19E+010	0.148	0.06	0.4	1.25	1.932	0.031	5.996
60	0.4	0.179	4.67E+010	0.23	0.075	-0.012	1.25	2	0.038	3.894
61	0.4	0.214	3.28E+010	0.333	0.112	-0.265	1.25	2.014	0.055	2.731
62	0.4	0.248	2.42E+010	0.458	0.166	-0.11	1.25	1.931	0.086	2.02
63	0.4	0.283	1.87E+010	0.607	0.245	0.208	1.25	1.932	0.127	1.555
64	0.4	0.318	1.48E+010	0.783	0.299	0.346	1.25	1.936	0.155	1.234
65	0.4	0.353	1.20E+010	0.989	0.344	0.049	1.25	1.925	0.179	1.003
66	0.4	0.387	9.97E+009	1.229	0.445	-0.064	1.25	2.083	0.214	0.831
67	0.4	0.422	8.40E+009	1.51	0.459	0.515	1.25	2.127	0.216	0.7
68	0.4	0.457	7.17E+009	1.837	0.624	0.182	1.25	1.988	0.314	0.597
69	0.4	0.492	6.19E+009	2.219	0.469	-0.397	1.25	1.783	0.263	0.516
70	0.4	0.526	5.40E+009	2.668	0.592	-0.569	1.25	2.049	0.289	0.45
71	0.4	0.561	4.75E+009	3.199	0.583	-0.353	1.25	1.775	0.328	0.396
72	0.4	0.596	4.22E+009	3.832	0.83	0.284	1.25	2.008	0.413	0.351
73	0.4	0.631	3.76E+009	4.595	0.856	-0.196	1.25	2.028	0.422	0.314
74	0.4	0.665	3.38E+009	5.529	0.936	0.251	1.25	1.978	0.473	0.282
75	0.4	0.7	3.05E+009	6.691	0.953	0.091	1.25	1.986	0.48	0.254
76	0.75	0.04	3.29E+012	0.006	0	-0.024	0.666	3.221	0	273.977
77	0.75	0.075	9.42E+011	0.021	0.008	-0.069	0.666	3.118	0.002	78.481
78	0.75	0.109	4.39E+011	0.045	0.034	-0.09	0.666	3.221	0.01	36.578
79	0.75	0.144	2.53E+011	0.079	0.076	0.559	0.666	2.675	0.029	21.079
80	0.75	0.179	1.64E+011	0.123	0.054	-0.149	0.666	3.296	0.016	13.689
81	0.75	0.214	1.15E+011	0.178	0.084	0.402	0.666	2.373	0.035	9.6
82	0.75	0.248	8.52E+010	0.244	0.162	0.75	0.666	2.635	0.062	7.103
83	0.75	0.283	6.56E+010	0.324	0.182	0.311	0.666	3.108	0.059	5.467
84	0.75	0.318	5.21E+010	0.418	0.233	-0.005	0.666	3.272	0.071	4.338

85	0.75	0.353	4.23E+010	0.527	0.285	-0.178	0.666	2.78	0.102	3.525
86	0.75	0.387	3.51E+010	0.656	0.421	-0.595	0.666	3.253	0.129	2.921
87	0.75	0.422	2.95E+010	0.805	0.483	0.121	0.666	3.151	0.153	2.46
88	0.75	0.457	2.52E+010	0.98	0.49	0.12	0.666	2.925	0.167	2.1
89	0.75	0.492	2.18E+010	1.183	0.487	-0.306	0.666	2.89	0.169	1.814
90	0.75	0.526	1.90E+010	1.423	0.577	0.554	0.666	2.699	0.214	1.582
91	0.75	0.561	1.67E+010	1.706	0.65	0.271	0.666	2.772	0.234	1.393
92	0.75	0.596	1.48E+010	2.044	0.784	0.146	0.666	3.078	0.255	1.235
93	0.75	0.631	1.32E+010	2.451	1.126	0.285	0.666	3.287	0.342	1.103
94	0.75	0.665	1.19E+010	2.949	1.26	-0.09	0.666	3.559	0.354	0.99
95	0.75	0.7	1.07E+010	3.568	1.36	0.475	0.666	3.392	0.401	0.895
96	1	0.04	5.84E+012	0.004	0.027	-0.191	0.5	3.61	0.008	487.070
97	1	0.075	1.67E+012	0.016	0.023	-0.492	0.5	3.359	0.007	139.522
98	1	0.109	7.80E+011	0.034	0.047	-0.131	0.5	3.124	0.015	65.027
99	1	0.144	4.50E+011	0.059	0.037	-0.395	0.5	3.635	0.01	37.473
100	1	0.179	2.92E+011	0.092	0.034	0.479	0.5	3.244	0.01	24.337
101	1	0.214	2.05E+011	0.133	0.051	-0.559	0.5	3.157	0.016	17.067
102	1	0.248	1.52E+011	0.183	0.129	-0.259	0.5	3.647	0.035	12.628
103	1	0.283	1.17E+011	0.243	0.149	-0.768	0.5	3.27	0.046	9.72
104	1	0.318	9.25E+010	0.313	0.169	0.167	0.5	3.556	0.048	7.712
105	1	0.353	7.52E+010	0.396	0.342	-0.405	0.5	3.662	0.093	6.267
106	1	0.387	6.23E+010	0.492	0.226	-0.261	0.5	3.223	0.07	5.194
107	1	0.422	5.25E+010	0.604	0.487	0.128	0.5	4.48	0.109	4.374
108	1	0.457	4.48E+010	0.735	0.377	0.226	0.5	3.792	0.099	3.734
109	1	0.492	3.87E+010	0.888	0.545	-0.496	0.5	3.337	0.163	3.225
110	1	0.526	3.38E+010	1.067	0.746	-0.169	0.5	4.097	0.182	2.813
111	1	0.561	2.97E+010	1.28	0.563	0.07	0.5	3.388	0.166	2.476
112	1	0.596	2.63E+010	1.533	0.921	-0.298	0.5	3.997	0.231	2.195
113	1	0.631	2.35E+010	1.838	1.067	-0.186	0.5	3.879	0.275	1.96

114	1	0.665	2.11E+010	2.212	1.115	0.035	0.5	4.302	0.259	1.761
115	1	0.7	1.91E+010	2.676	1.429	0.193	0.5	4.638	0.308	1.59
116	1.5	0.04	1.32E+013	0.003	0.02	-0.306	0.333	4.085	0.005	1095.90
117	1.5	0.075	3.77E+012	0.01	-0.002	-0.195	0.333	3.477	-0.001	313.924
118	1.5	0.109	1.76E+012	0.023	0.011	-0.226	0.333	3.585	0.003	146.310
119	1.5	0.144	1.01E+012	0.039	0.044	-0.384	0.333	3.664	0.012	84.314
120	1.5	0.179	6.57E+011	0.061	0.034	-0.207	0.333	3.658	0.009	54.757
121	1.5	0.214	4.61E+011	0.089	0.05	0.546	0.333	3.748	0.013	38.402
122	1.5	0.248	3.41E+011	0.122	0.096	-0.444	0.333	3.765	0.025	28.413
123	1.5	0.283	2.62E+011	0.162	0.102	0.076	0.333	4	0.025	21.869
124	1.5	0.318	2.08E+011	0.209	0.156	-0.104	0.333	4.235	0.037	17.351
125	1.5	0.353	1.69E+011	0.264	0.113	-0.471	0.333	4.422	0.026	14.101
126	1.5	0.387	1.40E+011	0.328	0.183	0.029	0.333	4.141	0.044	11.685
127	1.5	0.422	1.18E+011	0.403	0.261	0.235	0.333	4.643	0.056	9.841
128	1.5	0.457	1.01E+011	0.49	0.295	0.123	0.333	4.494	0.066	8.402
129	1.5	0.492	8.71E+010	0.592	0.362	0.353	0.333	5.059	0.072	7.256
130	1.5	0.526	7.60E+010	0.711	0.448	-0.072	0.333	5.213	0.086	6.33
131	1.5	0.561	6.68E+010	0.853	0.514	-0.131	0.333	4.704	0.109	5.57
132	1.5	0.596	5.93E+010	1.022	0.634	0.187	0.333	4.999	0.127	4.94
133	1.5	0.631	5.29E+010	1.225	0.766	-0.082	0.333	4.96	0.154	4.41
134	1.5	0.665	4.75E+010	1.474	0.738	-0.337	0.333	4.602	0.16	3.962
135	1.5	0.7	4.29E+010	1.784	0.955	-0.207	0.333	5.453	0.175	3.578
136	2	0.04	2.34E+013	0.002	0.005	-0.133	0.25	3.891	0.001	1948.280
137	2	0.075	6.70E+012	0.008	0.012	-0.235	0.25	3.955	0.003	558.087
138	2	0.109	3.12E+012	0.017	0.007	-0.43	0.25	3.991	0.002	260.107
139	2	0.144	1.80E+012	0.03	0.026	-0.328	0.25	4.065	0.006	149.892
140	2	0.179	1.17E+012	0.046	0.043	-0.334	0.25	4.09	0.011	97.347
141	2	0.214	8.19E+011	0.067	0.048	-0.286	0.25	4.107	0.012	68.269
142	2	0.248	6.06E+011	0.092	0.075	0.167	0.25	4.164	0.018	50.512

143	2	0.283	4.67E+011	0.121	0.077	0.422	0.25	3.979	0.019	38.879
144	2	0.318	3.70E+011	0.157	0.114	-0.014	0.25	4.199	0.027	30.846
145	2	0.353	3.01E+011	0.198	0.102	-0.538	0.25	4.203	0.024	25.069
146	2	0.387	2.49E+011	0.246	0.172	-0.109	0.25	4.322	0.04	20.774
147	2	0.422	2.10E+011	0.302	0.167	0.263	0.25	4.485	0.037	17.496
148	2	0.457	1.79E+011	0.367	0.214	0.109	0.25	4.285	0.05	14.936
149	2	0.492	1.55E+011	0.444	0.275	0.143	0.25	4.665	0.059	12.9
150	2	0.526	1.35E+011	0.534	0.374	0.042	0.25	4.782	0.078	11.253
151	2	0.561	1.19E+011	0.64	0.384	-0.052	0.25	5.017	0.077	9.903
152	2	0.596	1.05E+011	0.766	0.51	0.079	0.25	5.181	0.098	8.782
153	2	0.631	9.41E+010	0.919	0.513	-0.382	0.25	4.99	0.103	7.841
154	2	0.665	8.45E+010	1.106	0.759	-0.011	0.25	5.147	0.147	7.043
155	2	0.7	7.63E+010	1.338	0.873	-0.338	0.25	5.818	0.15	6.362
156	2.5	0.04	3.65E+013	0.002	0.001	0.067	0.2	3.692	0.0	3044.188
157	2.5	0.075	1.05E+013	0.006	0.004	0.081	0.2	3.709	0.001	872.011
158	2.5	0.109	4.88E+012	0.014	0.011	0.085	0.2	3.731	0.003	406.417
159	2.5	0.144	2.81E+012	0.024	0.024	0.085	0.2	3.841	0.006	234.206
160	2.5	0.179	1.83E+012	0.037	0.029	0.138	0.2	3.895	0.007	152.104
161	2.5	0.214	1.28E+012	0.053	0.038	0.252	0.2	3.885	0.01	106.671
162	2.5	0.248	9.47E+011	0.073	0.056	0.315	0.2	4.067	0.014	78.925
163	2.5	0.283	7.29E+011	0.097	0.063	-0.171	0.2	4.277	0.015	60.748
164	2.5	0.318	5.78E+011	0.125	0.09	0.57	0.2	4.313	0.021	48.198
165	2.5	0.353	4.70E+011	0.158	0.09	0.201	0.2	4.355	0.021	39.17
166	2.5	0.387	3.90E+011	0.197	0.147	0.356	0.2	4.569	0.032	32.46
167	2.5	0.422	3.28E+011	0.242	0.171	0.431	0.2	4.698	0.036	27.337
168	2.5	0.457	2.80E+011	0.294	0.202	0.303	0.2	4.58	0.044	23.338
169	2.5	0.492	2.42E+011	0.355	0.28	-0.049	0.2	4.879	0.057	20.156
170	2.5	0.526	2.11E+011	0.427	0.314	-0.216	0.2	5.024	0.063	17.583
171	2.5	0.561	1.86E+011	0.512	0.336	-0.14	0.2	5.089	0.066	15.473

172	2.5	0.596	1.65E+011	0.613	0.453	0.003	0.2	5.373	0.084	13.722
173	2.5	0.631	1.47E+011	0.735	0.472	0.291	0.2	5.48	0.086	12.251
174	2.5	0.665	1.32E+011	0.885	0.529	0.639	0.2	5.63	0.094	11.005
175	2.5	0.7	1.19E+011	1.07	0.622	0.564	0.2	6.076	0.102	9.94
176	3	0.04	5.26E+013	0.001	0	-0.101	0.166	3.868	0.001	4383.630
177	3	0.075	1.51E+013	0.005	0.005	-0.08	0.166	3.884	0.001	1255.696
178	3	0.109	7.02E+012	0.011	0.008	-0.078	0.166	3.901	0.002	585.241
179	3	0.144	4.05E+012	0.02	0.017	-0.074	0.166	3.919	0.004	337.256
180	3	0.179	2.63E+012	0.031	0.024	0.066	0.166	3.951	0.006	219.03
181	3	0.214	1.84E+012	0.044	0.038	0.024	0.166	4.004	0.01	153.606
182	3	0.248	1.36E+012	0.061	0.039	0.147	0.166	4.172	0.009	113.652
183	3	0.283	1.05E+012	0.081	0.049	0.209	0.166	4.44	0.011	87.478
184	3	0.318	8.33E+011	0.104	0.066	0.104	0.166	4.225	0.016	69.404
185	3	0.353	6.77E+011	0.132	0.089	0.295	0.166	4.933	0.018	56.404
186	3	0.387	5.61E+011	0.164	0.095	-0.193	0.166	4.464	0.021	46.742
187	3	0.422	4.72E+011	0.201	0.147	0.351	0.166	4.709	0.031	39.365
188	3	0.457	4.03E+011	0.245	0.181	0.244	0.166	4.743	0.038	33.606
189	3	0.492	3.48E+011	0.296	0.183	0.08	0.166	4.885	0.038	29.025
190	3	0.526	3.04E+011	0.356	0.278	-0.091	0.166	5.13	0.054	25.32
191	3	0.561	2.67E+011	0.427	0.28	-0.163	0.166	5.298	0.053	22.282
192	3	0.596	2.37E+011	0.511	0.383	0.034	0.166	5.563	0.069	19.759
193	3	0.631	2.12E+011	0.613	0.405	0.455	0.166	5.661	0.072	17.642
194	3	0.665	1.90E+011	0.737	0.445	0.365	0.166	5.678	0.078	15.848
195	3	0.7	1.72E+011	0.892	0.582	0.054	0.166	6.197	0.094	14.314

Table B-4: Computational results at Bumblebee scale: Structural parameters

Cases	α_m	α_e	α_a	φ	Cases	α_m	α_e	α_a	φ
1	89.198	90.201	0.827	90.127	100	89.572	90.699	0.820	90.441
2	86.682	92.019	3.884	91.232	101	89.444	91.091	1.225	90.685
3	84.915	93.388	6.110	92.020	102	89.111	91.333	1.603	90.834
4	82.504	114.8567.857		91.380	103	88.844	91.973	2.287	91.225
5	79.006	97.025	13.047	93.909	104	88.442	92.232	2.722	91.379
6	72.662	100.77420.413		95.600	105	88.076	93.522	4.013	92.147
7	72.629	102.30621.288		96.348	106	87.808	93.521	4.147	92.143
8	69.197	104.17125.171		97.068	107	86.127	94.661	6.060	92.781
9	68.250	116.53334.308		102.324	108	85.899	94.819	6.327	92.867
10	64.976	113.08734.047		100.726	109	85.627	95.371	6.927	93.177
11	53.001	111.52542.804		99.328	110	84.628	98.505	10.059	94.876
12	61.769	115.16837.821		101.356	111	85.311	99.594	10.679	95.468
13	49.649	137.88247.670		100.624	112	84.693	99.062	10.502	95.174
14	51.883	126.14452.529		104.690	113	84.681	101.32912.516		96.345
15	48.592	109.03345.573		98.071	114	83.351	101.96913.692		96.628
16	89.799	90.143	0.246	90.091	115	81.197	103.80216.371		97.455
17	89.484	90.458	0.690	90.290	116	89.990	90.024	0.026	90.015
18	88.482	91.131	1.893	90.705	117	89.966	90.085	0.091	90.054
19	87.881	91.532	2.615	90.948	118	89.933	90.182	0.194	90.116
20	87.038	93.105	4.291	91.887	119	89.883	90.308	0.330	90.195
21	85.939	94.467	6.037	92.666	120	89.830	90.490	0.519	90.310
22	80.622	96.628	11.483	93.745	121	89.691	90.678	0.745	90.428
23	83.200	95.970	9.049	93.456	122	89.522	90.907	1.025	90.571
24	76.298	97.223	15.489	93.926	123	89.400	91.153	1.300	90.724

25	74.713	105.58821.833	98.012	124	89.205	91.570	1.759	90.980	
26	74.366	103.40720.595	96.963	125	89.214	92.169	2.307	91.346	
27	75.292	109.38224.331	99.760	126	88.674	92.344	2.693	91.449	
28	76.925	114.85928.087	102.152	127	87.875	92.554	3.322	91.568	
29	68.328	100.02423.879	95.050	128	87.942	93.536	4.091	92.154	
30	75.973	106.41221.589	98.457	129	87.199	94.082	4.951	92.464	
31	55.469	114.61842.408	100.715	130	87.193	95.510	6.184	93.284	
32	57.872	116.40641.587	101.576	131	87.402	96.882	7.356	94.054	
33	65.343	112.62833.467	100.561	132	87.488	97.016	7.452	94.129	
34	54.134	120.33546.975	102.795	133	86.951	97.235	7.851	94.240	
35	51.359	124.65851.907	104.136	134	85.797	97.625	8.706	94.430	
36	89.943	90.129	0.141	90.082	135	84.521	99.263	10.763	95.275
37	89.756	90.473	0.532	90.299	136	89.991	90.017	0.019	90.011
38	88.840	90.874	1.452	90.547	137	89.977	90.060	0.064	90.038
39	89.012	92.076	2.299	91.289	138	89.953	90.130	0.139	90.083
40	88.167	92.619	3.196	91.610	139	89.918	90.226	0.241	90.144
41	87.768	93.760	4.373	92.283	140	89.884	90.350	0.368	90.222
42	85.798	96.826	8.016	93.993	141	89.809	90.491	0.527	90.311
43	85.088	96.911	8.479	94.024	142	89.719	90.656	0.714	90.414
44	82.403	97.663	10.790	94.360	143	89.662	90.887	0.949	90.559
45	83.538	99.355	11.370	95.295	144	89.542	91.091	1.184	90.686
46	79.853	102.75916.301	96.893	145	89.466	91.405	1.503	90.880	
47	55.649	98.358	14.502	94.587	146	89.199	91.665	1.848	91.039
48	70.979	103.30723.213	96.750	147	88.930	91.916	2.194	91.191	
49	75.242	105.75421.587	98.116	148	88.671	92.399	2.743	91.482	
50	74.196	108.80624.565	99.448	149	88.511	93.108	3.447	91.906	
51	74.711	111.51126.391	100.651	150	88.130	94.329	4.715	92.619	

52	68.787	114.86732.685	101.694	151	88.471	94.864	5.099	92.932	
53	66.715	116.75735.470	102.313	152	87.981	95.701	6.048	93.403	
54	77.753	115.16227.984	102.314	153	87.970	95.222	5.603	93.131	
55	52.843	124.33450.591	104.135	154	87.449	96.302	6.799	93.733	
56	89.943	112.5570.081	90.036	155	87.645	96.467	6.882	93.827	
57	89.756	90.329	0.410	90.209	156	89.994	90.016	0.017	90.010
58	89.628	90.659	0.757	90.416	157	89.984	90.047	0.050	90.030
59	89.169	90.974	1.280	90.611	158	89.968	90.103	0.108	90.066
60	88.654	91.804	2.251	91.121	159	89.946	90.178	0.186	90.113
61	87.953	92.762	3.438	91.694	160	89.913	90.272	0.286	90.173
62	87.882	93.561	4.144	92.168	161	89.877	90.398	0.417	90.252
63	88.310	94.373	4.688	92.647	162	89.831	90.533	0.559	90.337
64	87.438	95.582	6.142	93.329	163	89.798	90.703	0.732	90.444
65	85.005	97.968	9.404	94.598	164	89.692	90.897	0.948	90.565
66	81.908	98.271	11.571	94.671	165	89.643	91.096	1.152	90.689
67	81.238	99.141	12.662	95.108	166	89.484	91.316	1.414	90.825
68	80.672	104.31917.090	97.684	167	89.248	91.558	1.730	90.973	
69	60.558	108.71819.964	99.801	168	89.048	91.840	2.072	91.145	
70	82.780	111.14122.340	100.847	169	88.714	92.378	2.703	91.470	
71	63.116	112.12422.555	101.336	170	88.760	93.211	3.442	91.969	
72	75.650	110.01224.625	100.054	171	88.886	93.733	3.896	92.279	
73	82.654	113.81224.919	101.958	172	88.556	94.378	4.609	92.652	
74	66.789	114.86434.014	101.566	173	88.859	94.187	4.339	92.544	
75	62.776	117.39838.624	102.299	174	88.376	94.636	4.913	92.800	
76	89.966	90.072	0.079	90.046	175	88.282	95.070	5.353	93.048
77	89.888	90.186	0.217	90.118	176	90.000	90.011	0.011	90.007
78	89.715	90.358	0.458	90.227	177	89.994	90.040	0.041	90.026

79	89.567	90.573	0.718	90.362	178	89.983	90.086	0.088	90.055
80	89.377	91.031	1.205	90.648	179	89.966	90.149	0.153	90.095
81	89.239	91.475	1.660	90.922	180	89.944	90.229	0.236	90.146
82	88.775	92.119	2.447	91.313	181	89.913	90.327	0.338	90.207
83	88.249	92.305	2.895	91.422	182	89.884	90.448	0.463	90.284
84	87.559	92.691	3.633	91.647	183	89.838	90.586	0.608	90.370
85	65.875	94.261	4.560	92.583	184	89.791	90.745	0.774	90.470
86	86.206	94.701	6.041	92.806	185	89.712	90.947	0.990	90.596
87	84.779	95.363	7.485	93.154	186	89.701	91.116	1.155	90.701
88	84.237	96.106	8.396	93.558	187	89.533	91.345	1.424	90.843
89	84.491	100.351	11.726	95.840	188	89.338	91.557	1.691	90.973
90	83.901	101.017	12.592	96.164	189	89.099	91.992	2.186	91.238
91	85.221	100.642	11.666	96.009	190	89.153	92.554	2.690	91.579
92	82.225	104.273	16.254	97.720	191	89.271	92.934	3.023	91.807
93	81.647	103.900	16.217	97.520	192	88.987	93.434	3.580	92.103
94	80.203	105.735	18.536	98.336	193	88.966	93.514	3.663	92.150
95	78.076	107.938	21.540	99.255	194	88.943	93.893	4.034	92.373
96	89.976	90.019	0.031	90.012	195	88.930	94.184	4.318	92.542
97	89.938	90.125	0.139	90.079					
98	89.842	90.284	0.324	90.180					
99	89.722	90.470	0.546	90.297					

REFERENCES

- [1] Shyy W, Aono H, Chimakurthi S K, Trizila P, Kang C, Cesnik C E S and Liu H 2010 Recent progress in flapping wing aerodynamics and aeroelasticity *Prog. Aerosp. Sci.* **46** 284–327
- [2] Ma K Y, Chirarattananon P, Fuller S B and Wood R J 2013 Controlled flight of a biologically inspired, insect-scale robot *Science* **340** 603–607
- [3] Ifju P G, Jenkins D A, Ettinger S, Lian Y, Shyy W and Waszak M R 2002 Flexible-wing-based micro air vehicles *AIAA Pap.* **705** 1–11
- [4] Keennon M, Klingebiel K and Won H 2012 Development of the Nano Hummingbird: A Tailless Flapping Wing Micro Air Vehicle (American Institute of Aeronautics and Astronautics)
- [5] De Croon G, De Clercq K M E, Ruijsink R, Remes B and De Wagter C 2009 Design, aerodynamics, and vision-based control of the DelFly *Int. J. Micro Air Veh.* **1** 71–97
- [6] Anon www.avinc.com
- [7] Anon <http://www.delfly.nl/explorer.html>
- [8] Shyy W, Aono H, Kang C and Liu H 2013 *An Introduction to Flapping Wing Aerodynamics* (Cambridge University Press)
- [9] Anon <https://en.wikipedia.org/wiki/File:Archilochus-alexandri-002-edit.jpg>
- [10] Anon https://en.wikipedia.org/wiki/File:AD2009Aug08_Bombus_pratorum.jpg
- [11] Anon https://en.wikipedia.org/wiki/File:Drosophila_melanogaster_-_side_%28aka%29.jpg

- [12] Anon
https://commons.wikimedia.org/wiki/File:Vespula_germanica_Horizontalview_Ricard_Bartz.jpg
- [13] Kang C and Shyy W 2013 Scaling law and enhancement of lift generation of an insect-size hovering flexible wing *J. R. Soc. Interface* **10**
- [14] Kang C. and Shyy W 2014 Analytical model for instantaneous lift and shape deformation of an insect-scale flapping wing in hover *J. R. Soc. Interface* **11**
- [15] Weis-Fogh T 1973 Quick estimates of flight fitness in hovering animals, including novel mechanisms for lift production *J. Exp. Biol.* **59** 169–230
- [16] Ellington C P, van den Berg C, Willmott A P and Thomas A L R 1996 Leading-edge vortices in insect flight *Nature* **384** 626–630
- [17] Dickinson M H, Lehmann F-O and Sane S P 1999 Wing rotation and the aerodynamic basis of insect flight *Science* **284** 1954–1960
- [18] Birch J M and Dickinson M H 2003 The influence of wing-wake interactions on the production of aerodynamic forces in flapping flight *J. Exp. Biol.* **206** 2257–2272
- [19] Sane S P and Dickinson M H 2002 The aerodynamic effects of wing rotation and a revised quasi-steady model of flapping flight *J. Exp. Biol.* **205** 1087–1096
- [20] Curet O M, Swartz S M and Breuer K S 2013 An aeroelastic instability provides a possible basis for the transition from gliding to flapping flight *J. R. Soc. Interface* **10**
- [21] Lehmann F-O, Gorb S, Nasir N and Schützner P 2011 Elastic deformation and energy loss of flapping fly wings *J. Exp. Biol.* **214** 2949–2961
- [22] Fontaine E I, Zabala F, Dickinson M H and Burdick J W 2009 Wing and body motion during flight initiation in *Drosophila* revealed by automated visual tracking *J. Exp. Biol.* **212** 1307–1323
- [23] Ennos A R 1988 The Inertial Cause of Wing Rotation in Diptera *J. Exp. Biol.* **140** 161–169
- [24] Walker S M, Thomas A L R and Taylor G K 2009 Deformable wing kinematics in free-flying hoverflies *J. R. Soc. Interface* **7** 131–142
- [25] Young J, Walker S M, Bomphrey R J, Taylor G K and Thomas A L R 2009 Details of insect wing design and deformation enhance aerodynamic function and flight efficiency *Science* **325** 1549–1552
- [26] Nakata T and Liu H 2012 Aerodynamic performance of a hovering hawkmoth with flexible wings: a computational approach *Proc. Biol. Sci.* **279** 722–731

- [27] Ishihara D, Yamashita Y, Horie T, Yoshida S and Niho T 2009 Passive maintenance of high angle of attack and its lift generation during flapping translation in crane fly wing *J. Exp. Biol.* **212** 3882–3891
- [28] Altshuler D L, Dickson W B, Vance J T, Roberts S P and Dickinson M H 2005 Short-amplitude high-frequency wing strokes determine the aerodynamics of honeybee flight *Proc. Natl. Acad. Sci. U. S. A.* **102** 18213–18218
- [29] Sane S P and Dickinson M H 2001 The Control of flight force by a flapping wing: lift and drag production *J. Exp. Biol.* **204** 2607–2626
- [30] Combes S A and Daniel T L 2003 Flexural stiffness in insect wings I. Scaling and the influence of wing venation *J. Exp. Biol.* **206** 2979–2987
- [31] Mountcastle A M and Combes S A 2013 Wing flexibility enhances load-lifting capacity in bumblebees *Proc. R. Soc. Lond. B Biol. Sci.* **280**
- [32] Ramanarivo S, Godoy-Diana R and Thiria B 2011 Rather than resonance, flapping wing flyers may play on aerodynamics to improve performance *Proc. Natl. Acad. Sci.* **108** 5964–5969
- [33] Eldredge J D, Toomey J and Medina A 2010 On the roles of chord-wise flexibility in a flapping wing with hovering kinematics *J. Fluid Mech.* **659** 94–115
- [34] Yin B and Luo H 2010 Effect of wing inertia on hovering performance of flexible flapping wings *Phys. Fluids 1994-Present* **22**
- [35] Kang C-K, Aono H, Cesnik C E S and Shyy W 2011 Effects of flexibility on the aerodynamic performance of flapping wings *J. Fluid Mech.* **689** 32–74
- [36] Zhao L, Huang Q, Deng X and Sane S P 2009 Aerodynamic effects of flexibility in flapping wings *J. R. Soc. Interface*
- [37] Buchwald R and Dudley R 2010 Limits to vertical force and power production in bumblebees (Hymenoptera: *Bombus impatiens*) *J. Exp. Biol.* **213** 426–432
- [38] Sridhar M K and Kang C 2014 Effects of Flexible Wings in Hover Flight at Fruit Fly Scale *AIAA-2014-2311* (44th AIAA Fluid Dynamics Conference and Exhibit, Atlanta, Georgia, 16 - 20 June 2014)
- [39] Lucas K N, Johnson N, Beaulieu W T, Cathcart E, Tirrell G, Colin S P, Gemmell B J, Dabiri J O and Costello J H 2014 Bending rules for animal propulsion *Nat. Commun.* **5**
- [40] Sridhar M and Kang C Aerodynamic Performance of Flexible Flapping Wings at Bumblebee Scale in Hover Flight *53rd AIAA Aerospace Sciences Meeting* (American Institute of Aeronautics and Astronautics)

- [41] Billah K Y and Scanlan R H 1991 Resonance, Tacoma Narrows Bridge Failure, and Undergraduate Physics Textbooks *Am. J. Phys.* **59** 118–124
- [42] Anon https://commons.wikimedia.org/wiki/File:Buzz_off!.jpg
- [43] Anderson J 2010 *Fundamentals of Aerodynamics* (McGraw-Hill Education)
- [44] Willmott A and Ellington C 1997 Measuring the angle of attack of beating insect wings: robust three-dimensional reconstruction from two-dimensional images *J. Exp. Biol.* **200** 2693–2704
- [45] Sane S P 2003 The aerodynamics of insect flight *J. Exp. Biol.* **206** 4191–4208
- [46] Shyy W, Trizila P, Kang C-K and Aono H 2009 Can Tip Vortices Enhance Lift of a Flapping Wing? *AIAA J.* **47** 289–293
- [47] Fry S N, Sayaman R and Dickinson M H 2005 The aerodynamics of hovering flight in *Drosophila* *J. Exp. Biol.* **208** 2303–2318
- [48] Sun M and Tang J 2002 Unsteady aerodynamic force generation by a model fruit fly wing in flapping motion *J. Exp. Biol.* **205** 55–70
- [49] Liu H, Ellington C P, Kawachi K, Berg C van den and Willmott A P 1998 A computational fluid dynamic study of hawkmoth hovering *J. Exp. Biol.* **201** 461–477
- [50] Wang Z J 2000 Two dimensional mechanism for insect hovering *Phys. Rev. Lett.* **85** 2216
- [51] Ramamurti R and Sandberg W C 2002 A three-dimensional computational study of the aerodynamic mechanisms of insect flight *J. Exp. Biol.* **205** 1507–1518
- [52] Aono H, Liang F and Liu H 2008 Near- and far-field aerodynamics in insect hovering flight: an integrated computational study *J. Exp. Biol.* **211** 239–257
- [53] Liu H and Kawachi K 1998 A Numerical Study of Insect Flight *J. Comput. Phys.* **146** 124–156
- [54] Tu M and Dickinson M 1994 Modulation of Negative Work Output from a Steering Muscle of the Blowfly *Calliphora vicina* *J. Exp. Biol.* **192** 207–224
- [55] Lehmann F O and Götz K G 1996 Activation phase ensures kinematic efficacy in flight-steering muscles of *Drosophila melanogaster* *J. Comp. Physiol. A* **179** 311–322
- [56] Combes S A 2003 Flexural stiffness in insect wings II. Spatial distribution and dynamic wing bending *J. Exp. Biol.* **206** 2989–2997

- [57] Birch J M and Dickinson M H 2001 Spanwise flow and the attachment of the leading-edge vortex on insect wings *Nature* **412** 729–733
- [58] Wang Z J, Birch J M and Dickinson M H 2004 Unsteady forces and flows in low Reynolds number hovering flight: two-dimensional computations vs robotic wing experiments *J. Exp. Biol.* **207** 449–460
- [59] Wang Z J 2005 Dissecting Insect Flight *Annu. Rev. Fluid Mech.* **37** 183–210
- [60] Alben S and Shelley M 2005 Coherent locomotion as an attracting state for a free flapping body *Proc. Natl. Acad. Sci. U. S. A.* **102** 11163–11166
- [61] Trizila P, Kang C, Aono H, Shyy W and Visbal M 2011 Low-Reynolds-Number Aerodynamics of a Flapping Rigid Flat Plate *AIAA J.* **49** 806–823
- [62] Lehmann F-O, Gorb S, Nasir N and Schützner P 2011 Elastic deformation and energy loss of flapping fly wings *J. Exp. Biol.* **214** 2949–2961
- [63] Kang C and Shyy W 2013 Scaling law and enhancement of lift generation of an insect-size hovering flexible wing *J. R. Soc. Interface* **10**
- [64] Kang C, Aono H, Cesnik C E S and Shyy W 2011 Effects of flexibility on the aerodynamic performance of flapping wings *J. Fluid Mech.* **689** 32–74
- [65] Lehmann F O and Dickinson M H 1997 The changes in power requirements and muscle efficiency during elevated force production in the fruit fly *Drosophila melanogaster*. *J. Exp. Biol.* **200** 1133–1143
- [66] Wright J A and Smith R W 2001 An Edge-Based Method for the Incompressible Navier–Stokes Equations on Polygonal Meshes *J. Comput. Phys.* **169** 24–43
- [67] Smith R W and Wright J A 2003 An implicit edge-based ALE method for the incompressible Navier–Stokes equations *Int. J. Numer. Methods Fluids* **43** 253–279
- [68] Luke E A and George T 2005 Loci: a rule-based framework for parallel multi-disciplinary simulation synthesis *J. Funct. Program.* **15** 477–502
- [69] Thomas P D and Lombard C K 1979 Geometric Conservation Law and Its Application to Flow Computations on Moving Grids *AIAA J.* **17** 1030–1037
- [70] Kamakoti R and Shyy W 2004 Evaluation of geometric conservation law using pressure-based fluid solver and moving grid technique *Int. J. Numer. Methods Heat Fluid Flow* **14** 851–865
- [71] De Boer A, van der Schoot M S and Bijl H 2007 Mesh deformation based on radial basis function interpolation *Comput. Struct.* **85** 784–795
- [72] Ol M V, Bernal L, Kang C and Shyy W 2009 Shallow and deep dynamic stall for flapping low Reynolds number airfoils *Exp. Fluids* **46** 883–901

- [73] Kang C, Aono H, Sik Baik Y, Bernal L P and Shyy W 2013 Fluid Dynamics of Pitching and Plunging Flat Plate at Intermediate Reynolds Numbers *AIAA J.* **51** 315–329
- [74] Vandenheede R B R, Bernal L P, Morrison C L, Gogulapati A, Friedmann P P, Kang C-K and Shyy W 2014 Experimental and Computational Study on Flapping Wings with Bio-Inspired Hover Kinematics *AIAA J.* **52** 1047–1058
- [75] Aono H, Kang C, Cesnik C and Shyy W 2010 A Numerical Framework for Isotropic and Anisotropic Flexible Flapping Wing Aerodynamics and Aeroelasticity *28th AIAA Applied Aerodynamics Conference* (Chicago, Illinois: American Institute of Aeronautics and Astronautics)
- [76] Shyy W and Liu H 2007 Flapping Wings and Aerodynamic Lift: The Role of Leading-Edge Vortices *AIAA J.* **45** 2817–2819
- [77] Birch J M, Dickson W B and Dickinson M H 2004 Force production and flow structure of the leading edge vortex on flapping wings at high and low Reynolds numbers *J. Exp. Biol.* **207** 1063–1072
- [78] Kang C-K and Shyy W 2012 Effects of Flexibility on the Aerodynamics of a Hovering Flexible Airfoil at Reynolds Number of 100 to 1000 (American Institute of Aeronautics and Astronautics)
- [79] Yin B and Luo H 2010 Effect of Wing Inertia on Hovering Performance of Flexible Flapping Wings *Phys. Fluids* **22**
- [80] Trizila P, Kang C, Visbal M R and Shyy W Unsteady Fluid Physics and Surrogate Modeling of Low Reynolds Number, Flapping Airfoils *AIAA-2008-3821* (38th Fluid Dynamics Conference and Exhibit, 23 - 26 June 2008, Seattle, Washington)
- [81] Bratt J B 1953 *Flow Patterns in the Wake of an Oscillating Aerofoil*. (London)
- [82] Whitney J P and Wood R J 2010 Aeromechanics of passive rotation in flapping flight *J. Fluid Mech.* **660** 197–220
- [83] Sunada S, Zeng L and Kawachi K 1998 The Relationship Between Dragonfly Wing Structure and Torsional Deformation *J. Theor. Biol.* **193** 39–45
- [84] Chen J-S, Chen J-Y and Chou Y-F 2008 On the natural frequencies and mode shapes of dragonfly wings *J. Sound Vib.* **313** 643–654
- [85] Ellington C P 1984 The Aerodynamics of Hovering Insect Flight. III. Kinematics *Philos. Trans. R. Soc. Lond. B Biol. Sci.* **305** 41–78